Master's thesis

NTNU
Norwegian University of Science and Technology
Faculty of Engineering
Department of Civil and Environmental Engineering

Fredrik Strifeldt

Calibration and validation of fully LiDAR-derived 2D hydraulic models: Integrating SAR imagery and observed water surface elevations

Master's thesis in Civil and Environmental Engineering
Supervisor: Knut Alfredsen
June 2023

NTNU
Norwegian University of
Science and Technology

Fredrik Strifeldt

Calibration and validation of fully LiDAR-derived 2D hydraulic models: Integrating SAR imagery and observed water surface elevations

Master's thesis in Civil and Environmental Engineering
Supervisor: Knut Alfredsen
June 2023

Norwegian University of Science and Technology
Faculty of Engineering
Department of Civil and Environmental Engineering

NTNU
Norwegian University of
Science and Technology

NTNU
NORGES TEKNISK NATURVITENSKAPLIGE UNIVERSITIET
Institutt for bygg- og miljøteknikk

TVM 4905 Masteroppgåve i vassforsynings- og avløpsteknikk

Kandidat: **Fredrik Strifeldt**

Tema: **Modellering av flom med 2D hydrauliske modellar – vurdering av kvalitet av flomsonekart.**

1. Bakgrunn

Bruk av hydrauliske modellar for å finne område som er sett under vatn ved flaum er utbreidd både i Norge og internasjonalt. Data frå slike analyser er i brukt for arealplanlegging, skadeestimering og planlegg av flaumsikring. Større tilgang på både topografiske og batymetriske data frå måling med LiDAR gir eit svært detaljert grunnlag for modellering av flaumsletter. Men i Norge har vi i dag lite data for å vurdere desse simuleringane, og mykje slikt arbeid er basert på ruhet for flaumsletter basert på teoretiske data. Det er difor ønskjeleg å kunne evaluere slike simuleringar og forbetre grunnlaget for hydraulisk modellering av flaumsletter. Ei utfordring er at det er vanskeleg å finne gode data om kva som er vassdekt under flaum, og det som er kalibrert er ofte basert på vasstand målt i profil i elva.

Føremålet med denne oppgåva er å freiste å finne data for å kunne kalibrere ein hydraulisk modell basert på observert vassdekt areal under flom. Ulike kjelder for slike data skal undersøkast, og elver med data tilgjengeleg skal modellerast med HEC-RAS 2D for vassføringa som var når data vart registrert. I utgangspunktet skal elvene som brukast vere ha data frå topografisk og batymetrisk LiDAR. Arbeidet bygger på rapporten «Combined topographic and bathymetric LiDAR in flood inundation models».

2. Arbeidsoppgåver

Oppgåva vil ha følgjande hovuddelar:

1. Skaffe til veie data om vassdekt areal for ei eller fleire elver, enten frå arkivet til NVE om data eksisterer der, eller frå satellittdata. Her er bruken av SAR data spesielt interessant sidan slike data kan fjernmåle vassdekt areal satellitt og når det er overskya. Val av elver og tidspunkt vil vere avhengig av tilgang på data.

2. Finne ei metode for å hente ut vassdekt areal frå SAR satellitt data for å samanlikne med simulert vassdekt areal.

3. Basert på data frå 1) kalibrere HEC-RAS mot vassdekt areal under flaum. Basert på dette gjere ei vurdering av ruhet frå kalibrert modell mot det som typisk er brukt i samband med utarbeiding av flaumsonekart.

4. Gjere ei sensitivitetsanalyse for HEC-RAS i samband med flaumsonekartlegging og vurdere korleis resultata frå denne kan brukast for å gjere prosessen betre.

3. Rettleiing, data og informasjon

Faglærarar vert professor Knut Alfredsen ved institutt for bygg- og miljøteknikk, NTNU. Kandidaten er elles ansvarleg for innsamling, kontroll og bruk av data. Hjelp frå ovannemnde eller andre må refererast i rapporten.

4. Rapport

Struktur og oppsett av rapporten er viktig. Gå utifrå at det målgruppa er teknisk personell på seniornivå. Rapporten skal innehalde eit samandrag som gir lesaren informasjon om bakgrunn, framgangsmåte og hovudresultata. Rapporten skal ha innhaldsliste og referanseliste. Referanselista skal vere formatert etter ein eksisterande standard.

Denne oppgåveteksta skal vere inkludert i rapporten.

Data som er samla inn skal dokumenterast og leverast på digital form.

Formatet på rapporten skal følgje standarden ved NTNU. Alle figurar, kart og bilete som er inkludert i rapporten skal vere av god kvalitet med tydeleg tekst på akse og teiknforklaring.

Kandidaten skal inkludere ei signert fråsegn som seier at arbeidet som er presentert er eins eige, og at alle bidrag frå andre kjelder er identifiserte gjennom referanser eller på andre måtar.

Frist for innlevering er 22. juni 2023.

Insitutt for bygg- og miljøteknikk, NTNU

Knut Alfredsen
Professor

Abstract

Flooding is a widespread and costly phenomenon that affects millions of people. To mitigate the effects of flooding, the development of flood hazard maps has become crucial as they serve as valuable tools in flood management. Traditionally, these maps have been based on flood inundation models primarily utilizing 1D hydraulic models. However, with advancements in remote sensing techniques, 2D hydraulic models have emerged as a promising approach. Therefore, this thesis focuses on investigating the application of 2D hydraulic models that incorporate high-quality LiDAR data for both terrain and bathymetry within the study area.

Hence, the primary objective of this thesis was to obtain real-world observations, preferably SAR data capturing flooding events, to be employed in calibration and validation processes. The aim was to assess the effectiveness of utilizing such data and examine the outcomes it yields in flood inundation modelling. Although numerous studies have delved into this area of research, there is limited literature that specifically utilizes LiDAR data to represent river bathymetry.

The study area, the Surna River, provided numerous real-world observations, including multiple SAR images capturing multiple flood events, flood delineation vector data during the peak of the flooding caused by Storm Gyda, and observed water surface elevations. The integration of this data enabled a comprehensive evaluation of the performance of the model. The 2D hydraulic model was established using HEC-RAS software with a computational mesh of 10 m grid size, simulating the hydraulic behavior with the shallow water equations. Prior to the analysis, pre-processing and thresholding techniques were applied to the SAR images to precisely define flood boundaries, resulting in binary flood delineation maps used to evaluate and assess the performance of the model in accurately representing the flood extent.

Various calibration approaches were employed, including fine-tuning of Manning's n-values and regionalized calibration, with the aim of enhancing the performance of the model and evaluating the impact of Manning's n-values on the results. The calibration processes yielded optimal parameter sets for Manning's n-values in the main channel and floodplains, with the specific values dependent on the calibration approach. Notably, the model exhibited greater sensitivity to the Manning's n-value in the main channel compared to other parameters across all calibration approaches. The incorporation of high-resolution LiDAR data to represent the bathymetry of the river resulted in Manning's n-values in the main channel falling well within the ranges defined in the existing literature. This outcome highlights the potential of utilizing bathymetric LiDAR data in 2D hydraulic models.

The regionalized calibration using observed water surface elevations resulted in a highly accurate model performance, with a MAE of 0.02 m and a RMSE of 0.04 m. Furthermore, when calibrating the model against SAR imagery, it demonstrated a performance with an F^1 value of 0.67 and an F^2 value of 0.46. The regionalized calibration of the Storm Gyda flood event achieved an F^1 value of 0.83 and an F^2 value of 0.71, indicating a high level of accuracy in representing the flood extent.

The study showcased the promising capability of satellite imagery as a valuable tool for calibrating and validating 2D hydraulic models. The utilization of satellite imagery offers great potential in evaluating and assessing model results. However, it is important to acknowledge that the accuracy of these results is influenced by the uncertainties in the techniques employed to delineate the flood extent in SAR imagery.

Sammendrag

Flom er et utbredt og kostbart fenomen som påvirker millioner av mennesker. For å redusere virkningene av flom har utviklingen av flomsonekart blitt avgjørende da de fungerer som verdifulle verktøy i flomhåndtering. Tradisjonelt sett har flomsonekart blitt produsert på bakgrunn av 1D hydrauliske modeller. Imidlertid har 2D hydrauliske modeller blitt et lovende alternativ med den fremgangen som er gjort innen fjernmålingsteknikker de siste tiårene. Denne avhandlingen har derfor som fokus å undersøke bruken av 2D hydrauliske modeller som integrerer høykvalitets LiDAR-data for både terreng og elvebunnen i studieområdet.

Dette danner grunnlag for hovedmålet for denne avhandlingen, som var å innhente virkelige observasjoner, helst SAR-data som fanger opp flomhendelser, for å bruke dem i kalibrering og validering av modellen. Målet var å vurdere effektiviteten for bruk av slik data og undersøke resultatene de gir i modellering av utbredelsen av flom. Selv om mange studier har utforsket dette forskningsområdet, er det mangel på litteratur som spesifikt bruker LiDAR-data til å representere elvebunnen.

Studieområdet, elven Surna, ga mange virkelige observasjoner, inkludert SAR-bilder som fanger opp flere flomhendelser, vektordata for flomavdekning nær flomtoppen under Storm Gyda-flommen og observerte flomvannstander. Integreringen av disse dataene bidro til en omfattende evaluering av modellens ytelse. HEC-RAS-programvaren ble brukt til å etablere en 2D hydraulisk modell ved å bruke et beregningsnett med en rutenettstørrelse på 10 m, der «shallow water» likningene ble brukt for å simulere den hydrauliske atferden. Før analysene startet, ble SAR-bildene forbehandlet og analysert ved hjelp av en terskelteknikk for å nøyaktig definere flomgrensene. Dette innebar å skille mellom vann- og ikke-vannområder innen bildene, noe som resulterte i generering av binære flomkart. Disse kartene ble deretter brukt til å evaluere og vurdere modellens ytelse i å utføre en nøyaktig representasjon av flomomfanget.

Forskjellige kalibreringsmetoder ble brukt, inkludert finjustering av Manning's n-verdier og regionalisert kalibrering, med mål om å forbedre modellens ytelse og vurdere effekten av Manning's n-verdier på resultatene. Kalibreringsprosessene resulterte i optimale parameteroppsett for Manning's n-verdier i hovedkanalen og flomslettene, der de spesifikke verdiene var avhengig av hvilken kalibreringsmetode som ble brukt. Modellen viste spesielt stor følsomhet for Manning's n-verdi i elvebunnen sammenlignet med andre parametere i alle de forskjellige kalibreringsmetodene. Integreringen av høyoppløselige LiDAR-data for å representere elvebunnen resulterte i Manning's n-verdier i hovedkanalen som lå godt innenfor området definert i eksisterende litteratur. Dette resultatet understreker potensialet ved å bruke bathymetriske LiDAR-data i 2D hydrauliske modeller.

Den regionaliserte kalibreringen med bruk av observerte flomvannstander resulterte i en svært nøyaktig modellprestasjon med en MAE på 0,02 m og en RMSE på 0,04 m. Videre, når modellen ble kalibrert mot SAR-bilder, viste den en ytelse med en F^1-verdi på 0,67 og en F^2-verdi på 0,46. Den regionaliserte kalibreringen av Storm Gyda-flomhendelsen oppnådde en F^1-verdi på 0,83 og en F^2-verdi på 0,71, noe som indikerer en svært høy nøyaktighet i representasjonen av flomomfanget.

Resultatet av studien viste den lovende evnen til satellittbilder som verdifulle verktøy for kalibrering og validering av 2D hydrauliske modeller. Bruken av satellittbilder har stort potensiale i evaluering og vurdering av modellresultater. Det er imidlertid viktig å erkjenne at nøyaktigheten av disse resultatene påvirkes av usikkerheter i teknikkene som brukes til å avdekke flomomfanget i SAR-bildene.

Preface

This master's thesis signifies the completion of a two-year master's program in Civil and Environmental Engineering at NTNU in Trondheim. The process of working on this thesis has been highly educational, and during this period, I have acquired a vast amount of knowledge. However, it has been a challenging journey as a significant portion of the work conducted in this thesis has been learned during this semester. Nevertheless, this experience has also ignited a passion for this field of study within me.

I would like to express my gratitude to my supervisor, Professor Knut Alfredsen, from the Department of Civil and Environmental Engineering, for providing me with the opportunity to delve into this subject matter and for his guidance throughout the entire thesis process. I am grateful for the meaningful conversations we had and the valuable insights he shared, which greatly enriched my research and writing experience.

I would also like to extend my appreciation to my family and significant other for their support throughout my study journey. Their consistent presence and encouragement have been invaluable to me, providing the strength and motivation to navigate the ups and downs that come with being a student. I am grateful for their understanding and the support they have shown me during challenging times.

I hereby declare that the submitted work is my own and that all contributions from other sources are identified through references or other means.

Fredrik Strifeldt

Trondheim, June 22, 2023

Table of Contents

List of Figures

List of Tables

List of Abbreviations

1D	One-dimensional
2D	Two-dimensional
3D	Three-dimensional
ASTER	Advanced Spaceborne Thermal Emission and Reflection Radiometer
CEMS	Copernicus Emergency Management Service
dB	Decibel
DEM	Digital Elevation Model
DSM	Digital Surface Model
DTM	Digital Terrain Model
DSB	Directorate for Civil Protection and Emergency Planning
EMSR	Emergency Mapping Service for Rapid Mapping
ESA	European Space Agency
ETRS 1989	European Terrestrial Reference System 1989,
GPS	Global Positioning System
GRD	Ground Range Detected
HEC-RAS	Hydrologic Engineering Center's River Analysis System
LiDAR	Light Detection and Ranging
MAE	Mean Absolute Error
NIBIO	Norwegian Institute of Bioeconomy Research
NN54	Normal Null 1954 (Norwegian Vertical Reference System)
NN2000	Normal Null 2000 (Norwegian Vertical Reference System)
NVE	Norwegian Water Resources and Energy Directorate
RMSE	Root Mean Square Error
S1TBX	Sentinel-1 Toolbox
SAR	Synthetic Aperture Radar
SNAP	Sentinel Application Platform
SWE	Shallow Water Equations
TEK17	Regulations on technical requirements for construction works
USACE	United States Army Corps of Engineers
UTM	Universal Transverse Mercator
Q_N	Mean specific annual runoff
VH	Vertical-Horizontal Polarization
VV	Vertical-Vertical Polarization
WGS 84	World Geodetic System 1984

1 Introduction

1.1 Background

Flooding is a global phenomenon that occurs when the water level in a river or another body of water surpasses its normal capacity, resulting in the overflow onto surrounding land areas. It is a natural event that can have both negative and positive effects. While flooding is often associated with destructive consequences, such as property damage and human casualties, it can also have beneficial impacts, particularly in areas with agricultural regions. Additionally, in regions with hydroelectric power systems like Norway, spring floods can contribute to filling reservoirs that were depleted during the winter, ensuring an adequate supply of water for generating electricity (Tollan, 2023). Consequently, there has been an ongoing effort to comprehend, evaluate, and forecast flood events and their impacts (Mostert & Junier, 2009).

In 2021, there were 206 major flood disasters worldwide, representing over 56% of all major natural disasters that occurred during that year. This makes flooding the largest global natural disaster when compared to other events such as storms, earthquakes, wildfires, droughts, and others. These flood disasters resulted in 4393 deaths and affected tens of millions of people. The economic losses directly attributed to flood disasters in 2021 exceeded 74.6 billion USD. Additionally, the frequency of flood disasters in 2021 exhibited a significant increase of 48% compared to the average frequency observed over the past 30 years (1991-2020) (Ministry of Emergency Management et al., 2022). Furthermore, in Norway, flooding has led to an economic consequence of 30.3 billion NOK over the past decade (Hygen, 2023).

Moreover, according to a recent study by (Blöschl et al., 2020), it was discovered that in most of Europe, there has been a 90-year gap separating the flood-rich periods of the past from the most recent 30 years. This finding provides a potential explanation for the surprise experienced by both the general public and flood managers regarding the severity of recent floods. This highlights the importance of flood-risk assessment tools and flood-risk management strategies to acknowledge and take into account the current extraordinary flood-rich period in Europe. In order to further highlight the significance of this issue, a study conducted by (Hanssen-Bauer et al., 2017) examined the projected climate changes that will impact Norway until the end of the century. The findings of the study indicate that there will be an increase in intense rainfall events, leading to more frequent and intense rain-induced floods. Conversely, snowmelt floods are expected to occur less frequently and be less severe. The primary challenges that will have a significant impact on Norwegian society are urban flooding and flood-related issues caused by changes in precipitation, along with the increasing sea levels.

Given this context, it becomes even more imperative to prioritize the continuous development and updating of existing flood hazard maps in Norway. In fact, measures are already being taken in this regard. According to a report by (Eikenæs et al., 2020), the Norwegian Water Resources and Energy Directorate (NVE) has prioritized the upgrade of 57 out of a total of 145 flood hazard maps that have been produced since the inception of flood hazard mapping in 1998. Additionally, they are conducting evaluations

and improving the hydraulic data foundation to enhance the accuracy and reliability of the maps.

Flood hazard maps are utilized to ensure adherence to safety regulations specified in TEK17 (Regulations on technical requirements for construction works) (§ 7-2. Sikkerhet Mot Flom Og Stormflo - Direktoratet for Byggkvalitet, n.d.). These comprehensive maps are developed by the NVE and primarily focus on areas that are highly susceptible to flooding. Flood hazard maps delineate the regions prone to flooding at different recurrence intervals, based on historical observations and measurements of water flow and/or water levels (*3. Flaum - Direktoratet for Byggkvalitet*, n.d.).

A notable illustration of the practical application of flood hazard maps can be found in a study conducted by (Kalsnes et al., 2021). The study concluded that a substantial investment of approximately 38 billion NOK would be necessary in Norway to ensure adequate protection for existing buildings situated in flood-prone regions, mitigating the risks associated with flooding and erosion. The assessment was made possible by the utilization of flood hazard maps, which serve as essential tools in identifying vulnerable areas and guiding the implementation of effective flood risk management strategies.

Flood inundation modelling is a broad term that encompasses different methodologies aimed at studying the behavior of river and floodplain flow. These methodologies include empirical methods, hydraulic models, and simplified conceptual models (Teng et al., 2017). However, when it comes to developing flood hazard maps, the focus is primarily on employing flood inundation modelling techniques that utilize hydraulic models. These models allow for the simulation and analysis of the intricate dynamics involved in flooding, enabling a better understanding of flood behavior, and facilitating the creation of accurate flood hazard maps.

Traditionally, flood hazard maps in Norway have been developed using one-dimensional (1D) hydraulic models. However, with advancements in remote sensing techniques and research developments, two-dimensional (2D) hydraulic models are increasingly recognized as a more effective tool for flood inundation modeling. These models provide more accurate and detailed simulations by considering the 2D flow dynamics and incorporating the influence of topography and complex geometries. Therefore, the utilization of 2D hydraulic models holds great potential for enhancing the accuracy and reliability of flood hazard mapping (Cook & Merwade, 2009).

As previously mentioned, predicting the magnitude of floods is crucial in order to assess and mitigate potential damages in terms of economic and social impacts. Flood inundation models are a valuable tool for this purpose. However, these models need to be calibrated using historical flood events that have occurred in the specific area of interest. Conventionally, these models are often calibrated with observed water surface elevations, adjusting the roughness values at the cross sections (Pramanik et al., 2010). Moreover, due to the extreme nature of flood, obtaining these measurements can be challenging, which imposes limitations on the calibration and validation processes (Zotou et al., 2020). Despite the challenges involved in acquiring calibration data, achieving high-accuracy data is crucial for reliable flood predictions. In recent decades, remote sensing techniques have emerged as a reliable source of calibration data, coinciding with notable advancements in 2D flood inundation models (P. D. Bates, 2022).

Indeed, satellite imagery has demonstrated its value in accurately capturing and delineating the extent of flood inundation over specific areas during flood events (G.

Schumann et al., 2009). Optical sensors aboard satellites have been proven to provide robust and accurate detection of flooded areas (Faruolo et al., 2009). However, it is important to note that these sensors operate effectively only during daytime and in clear weather conditions when there are no clouds. This limitation poses a challenge in flood situations, particularly during rainfall events when clouds are typically present, making it difficult to obtain imagery using optical sensors. The limitations of optical sensors in capturing flood data during cloudy and nighttime conditions have led to an increased interest in Synthetic Aperture Radar (SAR) data for flood delineation. SAR is a microwave remote sensing technique that operates effectively in all weather conditions, including during heavy rainfall and at night. It utilizes radar signals to measure backscattered energy from the Earth's surface, allowing for the detection and delineation of flooded areas even in challenging weather conditions (Liang & Liu, 2020).

Previous studies have demonstrated the effectiveness of utilizing SAR data in calibrating and validating flood inundation models, with a specific emphasis on determining the optimal roughness parameter values (Ezzine et al., 2020; Hong Quang et al., 2019; Tarpanelli et al., 2013; Wood et al., 2016). Additionally, researchers have employed topographic LiDAR data to depict the terrain as high-resolution data, when employing SAR data in the calibration and validation processes (Di Baldassarre et al., 2009; Gobeyn et al., 2017; Hostache et al., 2009; Matgen et al., 2007; G. J.-P. Schumann et al., 2011). However, the exploration of LiDAR data specifically for representing the bathymetry of the river under study during the calibration and validation against SAR imagery is still limited. This presents an intriguing area for further research, as the incorporation of LiDAR-derived (Light Detection and Ranging) bathymetric information could enhance the accuracy and detail of riverbed topography representation, thereby improving the accuracy and reliability of flood inundation models.

1.2 Objective of the thesis

The objective of this thesis is to identify and gather relevant data for the calibration of a 2D hydraulic model, specifically focusing on real-world observations obtained during flood events. Various sources of calibration data will be investigated, and potential rivers with available calibration data will be modelled using HEC-RAS (Hydrologic Engineering Centers-River Analysis System) to simulate the flow conditions at the time of data collection. The ideal scenario is to find calibration data for rivers that have both topographic and bathymetric LiDAR data available. Specifically, the following tasks will be performed in the thesis:

1. Acquire data from real-world observations for a potential river, either from the archive of the NVE or from satellite data. The use of SAR imagery is particularly valuable as it can remotely detect flood inundation areas, even during nighttime and cloudy conditions.
2. Identify a method for delineating flood inundation areas from SAR imagery, that should be used in calibration and validation purposes of the 2D hydraulic model.
3. Calibrate the model using the available data for the river included in the study and assess the roughness values derived from the calibrated model in comparison to the typical values used in the development of flood inundation models.
4. Perform a sensitivity analysis for HEC-RAS with respect to flood inundation mapping and assess how the findings from this analysis can enhance the overall process.

1.3 Structure

The thesis consists of several chapters that provide a comprehensive exploration of flood inundation modelling. The first chapter introduces the background, objective, and overall structure of the thesis. The second chapter delves into the theoretical aspects of flood inundation modelling and provides a selective literature review, to establish a solid theoretical foundation and examine previous research in the field. The third chapter focuses on the methodologies employed for data processing, conducting 2D hydraulic simulations, and the calibration and validation processes. In the fourth chapter, the results obtained from the calibration and validation of the hydraulic simulations are presented. The fifth chapter offers a detailed discussion and analysis of the obtained results. Finally, the sixth and last chapter presents the conclusions drawn from the study and suggests potential directions for future work.

2 Flood inundation modelling

2.1 Two-dimensional hydraulic model in HEC-RAS

HEC-RAS is a software developed by the U.S. Army Corps of Engineers (USACE) that enables users to perform various hydraulic analyses. It provides capabilities for steady flow calculations in one-dimensional, unsteady flow calculations in one and two-dimensional scenarios, sediment transport and mobile bed computations, as well as water temperature and water quality modelling. HEC-RAS is a freely available software that was initially developed in 1995. The first version, 1.0, only supported 1D hydraulic models. However, with the release of version 5.0 in February 2016, HEC-RAS introduced the capability to create both 1D and 2D hydraulic models. This expanded functionality allows users to perform more comprehensive hydraulic analyses and simulations. The latest version of HEC-RAS, released June 5, 2023, is 6.4. However, for the 2D hydraulic simulations conducted in this study, version 6.3.1 of HEC-RAS was used, which was released on September 30, 2022 (*HEC-RAS Release Notes*, n.d.).

To gain a comprehensive understanding of the hydraulic capabilities of HEC-RAS, it is recommended that the reader consults the HEC-RAS 5.0 Reference Manual (G. W. Brunner, 2016). This manual provides detailed information about the full range of capabilities offered by HEC-RAS. Subsequently, the following sections will provide a simplified presentation of the relevant theories from this manual pertaining to unsteady 2D hydraulic modelling in HEC-RAS, which were utilized in the study.

HEC-RAS utilizes the shallow water equations (SWE) for channel and flood modelling, which are simplified equations derived from the more complex Navier-Stokes equations that describe fluid motion in three dimensions. By making certain assumptions and simplifications, such as incompressible flow, uniform density, and hydrostatic pressure, the shallow water equations provide a practical framework for simulating water behaviour in rivers and floodplains.

The shallow water equations, commonly referred to as the Saint-Venant equations, incorporate the principles of conservation of mass and momentum, allowing for the calculation of velocity and flow in both the x- and y-directions. Within HEC-RAS, these principles are mathematically represented as partial differential equations, forming the basis of the 2D hydraulic models used for simulating water behaviour in various hydraulic systems.

The unsteady partial differential form of the mass conservation (continuity) equation can be written as:

$$\frac{\partial H}{\partial t} + \frac{\partial (hu)}{\partial x} + \frac{\partial (hv)}{\partial y} - q = 0 \qquad (1)$$

where H is the water surface elevation, t is time, h is the depth of water, u and v are the vertically averaged velocities in x- and y-direction, x and y are the distance in the flow and lateral direction, and q is the lateral inflow term.

The partial differential from of the momentum equations for two-dimensional flow in both the x- and y-directions can be expressed as follows:

$$\frac{\partial u}{\partial t} + u\frac{\partial u}{\partial x} + v\frac{\partial u}{\partial y} = -g\frac{\partial H}{\partial x} + v_t\left(\frac{\partial^2 u}{\partial x^2} + \frac{\partial^2 u}{\partial y^2}\right) - c_f u + fv \quad (2)$$

$$\frac{\partial v}{\partial t} + u\frac{\partial v}{\partial x} + v\frac{\partial v}{\partial y} = -g\frac{\partial H}{\partial y} + v_t\left(\frac{\partial^2 v}{\partial x^2} + \frac{\partial^2 v}{\partial y^2}\right) - c_f v - fu \quad (3)$$

where H is the water surface elevation, t is time, u and v are the vertically averaged velocities in x- and y-direction, x and y are the distance in lateral direction, v_t is the horizontal eddy viscosity coefficient, c_f is the bottom friction coefficient, and f is the Coriolis parameter.

Diffusion wave, commonly used in 2D hydraulic models, is obtained by simplifying the 2D momentum equations. This involves removing the acceleration terms related to changes in velocity over time and space. The resulting equation considers only gravity, friction, and hydrostatic pressure forces. The diffusion form of the momentum equation can be expressed as follows:

$$c_f u = -g\frac{\partial H}{\partial x} \quad (4)$$

$$c_f v = -g\frac{\partial H}{\partial x} \quad (5)$$

where H is the water surface elevation, u and v are the vertically averaged velocities in x- and y-direction, and c_f is the bottom friction coefficient.

The diffusion wave equations are derived by combining the diffusion form of the momentum equations with the continuity equation, with the aim of solving the water surface elevation. As a result, the diffusion wave equations offer improved stability, ease of solution, and reduced computational requirements for a variety of scenarios. However, it is important to acknowledge that the diffusion wave equations sacrifice accuracy compared to the full shallow water equations due to the omission of acceleration terms. Consequently, their applicability is limited to a subset of problems within the full range (G. Brunner et al., 2020).

Manning's formula is used to determine the bottom friction coefficient c_f, and it can be expressed as follows:

$$c_f = \frac{n^2 g|V|}{R^{\frac{4}{3}}} \quad (6)$$

where n is Manning's n, g is the acceleration term due to gravity, $|V|$ is the magnitude of the velocity-vector, and R is the hydraulic radius.

HEC-RAS employs the sub-grid bathymetry approach (Casulli, 2009) to address the challenge of incorporating fine topographic details from high-resolution airborne remote sensing data into a 2D computational grid. To account for the fine topographic features, the computational grid cells include additional information such as hydraulic radius, volume, and cross-sectional area, which can be pre-computed from the fine bathymetry data. Although the high-resolution details are lost, this approach ensures that the numerical method considers the fine bathymetry through mass conservation.

Furthermore, to take advantage of orthogonality in grids, HEC-RAS utilize a hybrid discretization scheme combining finite difference approximations and finite volume approximations. Moreover, a Newton-like solution technique is employed to compute the discrete solution for the hydraulic equations.

In HEC-RAS, the computational domain is divided into non-overlapping polygons to create a grid, which can be structured or unstructured. The grid allows for various cell shapes, such as triangles, squares, rectangles, and polygons with up to eight sides, providing flexibility for complex geometries. The software assumes that the cells in the grid are orthogonal to each other, simplifying computations and improving computational speed (G. W. Brunner, 2023). To account for the second-order derivative terms and the differential nature of the variable relationship, HEC-RAS incorporates a dual grid alongside the regular grid. This dual grid spans the computational domain and establishes a correspondence between dual nodes and regular grid cells, as well as between dual cells and regular grid nodes. The inclusion of the dual grid is essential for numerically modeling the differential equations in the software (G. W. Brunner, 2016).

2.2 Data and modelling requirements

Flood inundation models require four classes of information data: information about the topography and bathymetry, boundary conditions, values of the friction coefficient, and observations of a real flood to calibrate the model and validate its performance (P. D. Bates, 2022).

2.2.1 Topographic and bathymetric data

The topography of floodplains and river channels plays a crucial role in flood hydraulics and the extent of simulated floods, making it the most critical factor in hydraulic modelling for accurate flood predictions (Horritt & Bates, 2001; Nicholas & Walling, 1997). Given the generally flat nature of river floodplains, deficiencies in topographic data can lead to significant discrepancies in hydraulic results, affecting the delineation of the flood area (P. D. Bates & De Roo, 2000). As a result, optimizing the quality of topographic data is of utmost importance, given the potential errors it can introduce in risk assessment, flood management, and flood hazard classification (Casas et al., 2006).

Over the past three decades, there has been significant progress in improving the quality of topographic data, largely driven by advancements in remote sensing technology. Particularly, LiDAR data has become increasingly available on a national scale in many developing countries, with a horizontal resolution of 1-2 meters and a vertical accuracy of approximately 10 centimetres (P. D. Bates, 2022). In Norway, about 80% of the country is already covered by topographic data obtained through LiDAR scanning, and full coverage is expected by 2023 (Breili et al., 2020).

LiDAR-derived topographic data is highly suitable for flood inundation modelling due to its ability to effectively separate vegetation and buildings from open ground (P. D. Bates,

2022). However, it is important to note that topographic LiDAR technology is unable to penetrate water (Leatherman, 2003), which can result in a misrepresentation of river bathymetry. Studies have highlighted that this limitation can lead to erroneous flood inundation predictions (Awadallah et al., 2022). Therefore, while LiDAR offers numerous advantages for topographic data collection, the accurate representation of river bathymetry requires additional techniques and considerations.

Obtaining bathymetric data poses significant challenges, even in well-resourced countries. Conventional methods like ground surveys employing GPS and total station equipment are resource-intensive and face limitations when dealing with large rivers. Field surveys also utilize alternative technologies such as side-scan sonar and multibeam echo to accurately map channel geometry in extensive river systems (P. D. Bates, 2022).

Bathymetric LiDAR, a relatively new technology explicitly designed for measuring water depth, overcomes some of these challenges. By utilizing aerial vehicles, bathymetric LiDAR enables the scanning of much larger areas compared to traditional methods, providing enhanced accuracy and spatial resolution.

LiDAR, a technology developed in the 1960s, is an active remote sensing system widely used for terrain modelling. One of the significant advantages of LiDAR is its capability to capture highly accurate and high-resolution 3D terrain models, commonly represented as point clouds (Dowman, 2004). Remote sensing, on the other hand, refers to the scientific discipline focused on gathering information about the Earth's surface features from a distance, accomplished typically by utilizing sensors installed on aircraft or satellites (Navalgund et al., 2007).

Topographic LiDAR, commonly referred to as red LiDAR, is an airborne LiDAR system that utilizes a light source with a wavelength ranging from 1000 to 1600 nm. This light is directed towards the Earth's surface and emitted back to the aerial vehicle upon interaction with various objects such as roads, buildings, vegetation, and the ground surface (Dong & Chen, 2017). When the laser pulses are directed towards vegetated areas, the first interaction occurs with the canopy, followed by the ground. The reflected light from the canopy is known as the first return, while the light reflected from the ground is called the last return. In cases where a single pulse produces multiple returns, certain LiDAR systems have the capability to capture the complete waveform, providing more detailed information about the surface. Additionally, the laser pulse interacts differently with different surfaces, resulting in variations in intensity, which can be leveraged to derive valuable information about the surface and objects (Smith et al., 2006).

The laser scanner includes a receiver unit with a discriminator and a time interval meter. This unit logs the returning signal and calculates the elapsed time between when the signal was sent and when it returns. By using the velocity of light and half the round-trip time, this information is then used to calculate the distance between the laser and the terrain feature using this formula:

$$D = c\,(\frac{\Delta T}{2}) \qquad (7)$$

where, D is the distance of the object, c is the speed of light, and ΔT is the time required by the light to travel (Mehendale & Neoge, 2020).

The information is stored and visualized as a three-dimensional point cloud in a digital surface model (DSM), which captures elevation measurements for each reflected point. Additionally, it is possible to remove points that are above the ground level in order to generate a digital terrain model (DTM). The terminology of different elevation models can be confusing, as the term digital elevation model (DEM) is commonly used in research papers. DEM is often a broad term that can refer to various types of elevation models, including DTM, DSM, and others (Dong & Chen, 2017; Smith et al., 2006).

On the other hand, bathymetric LiDAR, also known as green LiDAR, is specifically designed for obtaining information about water depth in rivers and coastal areas. Unlike topographic LiDAR, which uses an infrared laser, bathymetric LiDAR employs two lasers with different wavelengths to separate the water bottom from the water surface during depth measurements. A green laser with a wavelength of 532 nm is utilized to detect the water bottom, while an infrared laser with a wavelength of 1064 nm is employed to identify the water surface (LaRocque & West, 1999). The wavelength of the green laser is optimized for penetrating the water surface and accurately measuring the water depth. In contrast, the red laser used in topographic LiDAR cannot penetrate water and hence returns the signal from the water surface. The time difference between the two return signals is used to calculate the water depth (Lin, 1995).

However, bathymetric LiDAR faces certain limitations in measuring water depth due to factors such as absorption, scattering, and refraction of the green laser in water, which can affect laser energy and limit the measurable depth. Other elements that influence the maximum water depth measurable by bathymetric LiDAR include water turbidity, interaction with bottom radiance, as well as incident sun angle and intensity (Irish & White, 1998). Under optimal conditions, bathymetric LiDAR has been able to measure water depths up to 60 meters (Wozencraft & Lillycrop, 2003).

2.2.2 Boundary conditions

Boundary conditions are crucial parameters in flood inundation modelling as they provide vital information about the behaviour at the edges of a system. They can be categorized into three types: external boundary conditions, internal boundary conditions, and global boundary conditions. External boundary conditions are directly associated with the boundary of the 2D flow area and include flow hydrograph, stage hydrograph, normal depth, and rating curve. Internal boundary conditions are applied within the 2D flow area and encompass flow hydrograph and precipitation. Global boundary conditions, on the other hand, apply to the entire model and consist of precipitation, evapotranspiration, and wind (G. W. Brunner, 2023).

The flow hydrograph is the most commonly used upstream boundary condition in flood inundation models. It represents the water flow (discharge) over a specific time period. Input parameters, including flow values at different time intervals and an energy gradient, are required for the flow hydrograph. The energy gradient helps calculate the normal depth at the upstream boundary condition, which is then used to distribute water to the cells at the boundary. By providing information on the varying flow rates, the flow hydrograph enables the model to simulate the dynamic behaviour of the river system over time (G. W. Brunner, 2016).

Normal depth is commonly employed as the downstream boundary condition in flood inundation modelling due to the lack of available field data for most design flows. In such

cases, Manning's equation can be utilized to compute an approximate value for the normal depth boundary condition (Robinson et al., 2019).

When selecting the location of boundary conditions in a flood inundation model, it is important to place them sufficiently far from the area of interest. This ensures that the location of the boundary conditions does not unduly influence the results. By positioning the boundary conditions at a suitable distance, the model can provide more reliable and accurate outcomes for the specific area of focus. This consideration helps to minimize any potential biases or distortions caused by the proximity of the boundary conditions to the region under study (G. Brunner et al., 2020).

Boundary data in flood inundation models can be obtained from various equipment sources, such as rain gauges, coastal water level stations, and river gauging stations, which measure water level and discharge. Measured data can be used to develop numerical and statistical models, allowing for extrapolation when faced with new situations. Flood inundation models aim to capture extreme behaviours, which can introduce additional complexities. During extreme conditions, measurement equipment is more susceptible to failure, leading to increased observation errors. Furthermore, numerical and statistical models that are calibrated for specific conditions may need to extrapolate beyond the calibrated flow range (P. D. Bates, 2022).

One example of potential errors in flood modelling arises from rating curves, which convert stage values to discharge. These curves are typically developed using measurements from non-flood flow states. As a result, during large floods and out-of-bank flows, the momentum transfer between the main channel and flood can cause flow error estimates of up to ±25 % if this mechanism is not considered during rating curve development (Ervine et al., 1982).

Another example is a study done by (McMillan et al., 2012), where they found typical errors in river discharge measurements at ground gauging stations range from ±10-20 % for medium or high in-bank flows to up to ±40 % for out-of-bank flows. These errors exist even before any statistical or numerical extrapolation is performed to estimate values for more extreme and unobserved events.

According to (P. D. Bates, 2022), the accuracy of discharge measurements has not seen significant improvement over many decades, and there are no apparent emerging technologies that would lead to a drastic increase in accuracy in the future. As a result, gauged discharges are expected to become the primary source of error in flood inundation modelling studies, particularly as the quality of fine spatial resolution topography and validation data improves.

2.2.3 Roughness assignments

Roughness, along with topographic data, is a critical input parameter in flood inundation models (Marks & Bates, 2000). The calibration process in hydraulic models often involves tuning roughness parameters to match model predictions with real-world observations. However, this method can be questionable as it may lead to the use of non-physically representative roughness values to compensate for deficiencies in the model scheme, computation method, or model inputs (Aronica et al., 1998). Therefore, in order to limit the range of input parameters during the calibration process of flood inundation models, it is essential to prioritize accurate estimates of roughness parameters. This is particularly crucial as these models are commonly utilized for designing embankments with discharge values that exceed the range of available observed data. Thus, using realistic parameters becomes even more important to ensure reliable and meaningful results (Straatsma & Baptist, 2008).

Manning's n-value is widely used as a roughness coefficient in hydraulic modelling, particularly in open channel flow calculations using Manning's equation. The value of Manning's n represents the resistance to flow offered by the channel surface and is derived from empirical data obtained from rivers and streams worldwide. It serves as a crucial parameter in estimating the flow velocity and water surface elevation in open channels. On the other hand, Manning's formula is derived using theoretical principles based on the phenomenological theory of turbulence (Gioia & Bombardelli, 2001).

Aerial or satellite imagery (Chaulagain, 2018; Straatsma & Baptist, 2008), textbooks (Chow et al., 1988; Te Chow, 1959), guidelines found in research papers (González-Sanchis et al., 2012), and site inspections (surveying) are all valuable resources when it comes to the assignments of roughness values and determining the values of Manning's n coefficient.

2.2.4 Calibration and validation data

The utilization of actual flood event observations is paramount in the calibration and validation process of a flood inundation model. Consequently, the availability of these observations holds significant importance in the development of such models. The observations can encompass various types of data, including measured water surface elevations, velocity, discharge, as well as flood extent derived through satellite imagery or aerial photography. However, it is important to acknowledge that these observations are prone to significant errors (P. D. Bates, 2022).

Numerous studies have investigated the uncertainties associated with the primary data sources used in the calibration and validation of flood inundation models. For instance, (McMillan et al., 2012) reported an error range of ±10-20 % for medium or high-in-bank flows and up to ±40 % for out-of-bank flows when measuring discharge. When it comes to water level measurements at gauging stations, an error of approximately ±0.01-0.02 m has been reported (P. D. Bates, 2022). Post-event high water wrack or water stains, used to estimate water level, introduce an average error of around ±0.3-0.5 m, with the possibility of more extreme outliers (Fewtrell et al., 2011). Measurements of water velocity with a current meter indicate an error of approximately 2% in laboratory tests, while under field conditions, an error range of 5-10% is possible (Carter & Anderson, 1963). Evaluating flood extents using SAR imagery, such as COSMO-SkyMed and Sentinel-1b, in comparison with aerial photos, (Horritt et al., 2001) found that radar data could capture around 75% of the true flooded area in a flood event in the United Kingdom.

Satellite data is particularly valuable for calibration and validation purposes in flood inundation modelling due to its ability to provide measurements over large spatial scales. Given that flooding is a large-scale phenomenon, satellite data offers an appealing method for obtaining information about flood areas across various temporal scales. Over the last two decades, there has been a substantial increase in satellite missions equipped with instruments capable of mapping floods. This growth has led to a consensus among space agencies and scientists that satellites can effectively support flood monitoring efforts (G. J. Schumann et al., 2018).

The two most commonly used sensors for flood mapping worldwide are optical and radar (microwave) sensors. Optical sensors have been in use since the mid-1970s but have limitations related to cloud cover and the density of vegetation cover and built-up areas. Mapping flood inundation areas using optical images is relatively straightforward and these images now hold significant historical value. SAR, on the other hand, has been providing more available satellite images of floods since the mid-1990s, with the launch of high-resolution SAR satellites in the last decade further improving the situation. During

high-impact flood events, weather conditions can be extremely adverse, and this is often when accurate high-resolution flood data is needed the most. SAR technology can penetrate cloud cover and operate in all-weather conditions, offering day and night capabilities, which gives it a distinct advantage for flood mapping purposes (G. J.-P. Schumann & Moller, 2015).

The increased accessibility of satellite data and its ability to operate in all weather conditions have significantly improved flood mapping reliability and have contributed to significant advancements in flood inundation modelling. Satellite data has become increasingly valuable in the calibration and validation of flood inundation models (P. Bates et al., 1997).

In a study by (P. D. Bates et al., 2006) a hybrid 1D-2D flood model was assessed using SAR imagery and high-quality data. The researchers used floodplain terrain data from airborne LiDAR, upscaled to an 18 m resolution for modelling. Bathymetric data from ground surveys were incorporated as a rectangular channel, matching actual cross sections. Boundary conditions came from ground gauging stations, and the model was minimally calibrated with friction parameters within plausible ranges. This study stood out due to its utilization of SAR images from multiple occurrences of a significant flood in November 2000. These images precisely delineated the flood shoreline within an accuracy range of approximately 1-2 meters, making it one of the most reliable sources of information on flood extent ever collected. The research outcomes demonstrated that by utilizing an airborne radar image obtained close to peak flow, the model achieved an accurately predicted 89 % of the observed inundated area with minimal under- or overprediction.

2.3 The Sentinel-1 mission

The Sentinel-1 mission consists of a constellation of satellites in polar orbits that conduct continuous C-band SAR imaging day and night. With this advanced imaging capability, the satellites are able to acquire imagery regardless of weather conditions. Sentinel-1 serves as the first mission among the five missions being developed by the European Space Agency (ESA) for the Copernicus initiative (*Sentinel-1 - Missions - Sentinel Online - Sentinel Online*, n.d.).

The original configuration of the Sentinel-1 mission included two satellites, Sentinel-1A and Sentinel-1B, which shared the same orbital plane. Sentinel-1A was launched on April 3, 2014, while Sentinel-1B was launched on April 25, 2016. Two new satellites, Sentinel-1C and Sentinel-1D are planned to replace the first two satellites, Sentinel-1A and Sentinel-1B, at the end of their operational lifespan (*Sentinel-1 - Mission Summary - Sentinel Online - Sentinel Online*, n.d.). However, Sentinel-1B has been retired due to malfunctioning on December 23, 2021, leaving only Sentinel-1A as the active satellite within the constellation. The retirement of Sentinel-1B has accelerated the process of launching Sentinel-1C (*ESA - Mission Ends for Copernicus Sentinel-1B Satellite*, n.d.), which was originally planned to launch by the end of 2023 (*Sentinel-1C - ITC Satellites and Sensors Database*, n.d.).

The Sentinel-1 satellites are positioned in a sun-synchronous, near-polar orbit and feature a C-band SAR instrument operating at 5405 GHz. With a revisit period of 12 days for each individual satellite, their 180° orbital separation allows for a reduced revisit period of 6 days at the equator and even more frequent revisits at higher latitudes. The primary acquisition mode of the radar is Interferometric Wide swath (IW), offering a

swath width of 250 km and a spatial resolution of 5 m x 20 m (*Sentinel-1 - Mission Summary - Sentinel Online - Sentinel Online*, n.d.), illustrated in Figure 1.

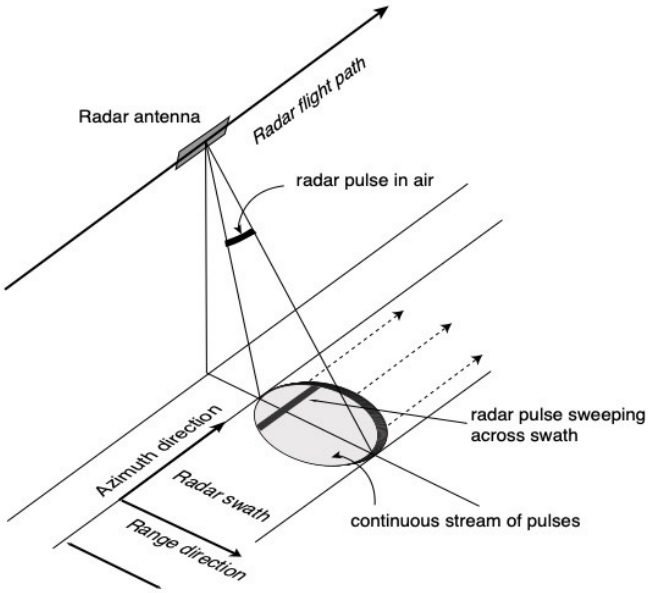

Figure 1: Radar in motion to enable SAR imaging (*Overview | Get to Know SAR – NASA-ISRO SAR Mission (NISAR)*, n.d.).

The SAR imagery obtained from the Interferometric Wide swath mode is provided as Level-1 Ground Range Detected (GRD) products, often acquired in dual polarization, VV (Vertical-Vertical) and VH (Vertical-Horizontal). These products undergo detection, multi-looking, and projection to ground range using an Earth ellipsoid model. The resulting GRD products have square spatial resolution pixels and square pixel spacing, which helps in reducing speckle but at the expense of slightly lower spatial resolution (*Sentinel-1 - Data Products - Sentinel Online - Sentinel Online*, n.d.).

The Sentinel-1 products are made available systematically and free of charge to all data users including the public, scientific and commercial users. This have resulted in that many researchers have been using Sentinel-1 SAR imagery in studies when assessing hydraulic models with the use of SAR data from the Sentinel-1 mission (Elkhrachy et al., 2021; Ezzine et al., 2020; Melkamu et al., 2022; Zotou et al., 2020).

2.4 Calibration and validation

Calibration and validation are critical steps in the development of flood inundation models. During the calibration process, model parameters are adjusted to achieve the best possible agreement between the model outputs and historical data. This ensures that the model accurately represents the observed behaviour of floods and their impacts. Subsequently, the calibrated model is validated using independent datasets to assess its ability to reproduce flood behaviour and historical flood events that were not used during the calibration. Calibration and validation of flood inundation models are essential to ensure reliable results and achieve confidence in the accuracy of the model (Dhillon et al., 2014).

The calibration process of the model enhances understanding of the sensitivity to data, friction forces, and other empirical coefficients. In contrast, an uncalibrated flood inundation model is merely a numerical experiment, lacking an understanding of its ability to replicate realistic flows and water surface elevations within the system. The use

of an uncalibrated model is only justified in emergency scenarios, where time or data limitations prevent calibration, as some information from an uncalibrated model is better than having no information at all (G. Brunner et al., 2020).

In the calibration process of a hydraulic model, the focus is primarily on calibrating the surface friction parameter, which is the key parameter in most cases. In contrast, other environmental prediction codes often involve tens or even hundreds of parameters that require calibration (P. D. Bates, 2022). However, measuring surface friction directly in the field remains a challenge, leading to difficulties in parameterizing and calibrating friction accurately. Hydraulic resistance encompasses several components that are theoretically unmeasurable, although advancements have been made in evaluating vegetation-induced resistance using remotely sensed plant biophysical data (Mason et al., 2003).

As a results, despite indirect measurements (Arcement & Schneider, 1989), modellers experience, and land use data to establish a plausible range of friction values, the spatial distribution of friction parameters remains uncertain. Consequently, adjustments to these parameters are often necessary to optimize the agreement between the model and observed data. However, it is important to note that the optimization process has a limitation: while it brings the parameters closer to their true values, it can also unintentionally compensate for errors in the input and validation data, as well as discrepancies between the modelled hydraulic processes and real-world conditions (P. D. Bates, 2022).

2.5 Uncertainty

Uncertainty arises when we have limited confidence in a particular matter, spanning a range from complete uncertainty about an outcome to nearly complete certainty. Uncertainty analysis involves considering uncertainties associated with various factors such as model structure, parameters, boundary conditions, and calibration/validation data to evaluate the uncertainty present in model outputs (Prinos, 2009). Uncertainty analysis has gained significant attention in the flood inundation modelling community and is considered crucial for accurate predictions in non-idealized environmental systems. Addressing uncertainty can be achieved through a systematic approach involving three key steps (Teng et al., 2017):

1. Identify and determine the sources of uncertainty.
2. Quantify or qualitatively rank the uncertainty from different sources and prioritize them.
3. Properly communicate the uncertainty.

Flood inundation modelling involves various sources of uncertainty, with two fundamental types that are important to distinguish: natural and epistemic uncertainty. Natural uncertainty arises from unpredictable outcomes inherent in stochastic processes and cannot be reduced. Epistemic uncertainty, on the other hand, stems from incomplete knowledge about the studied process and can be reduced by acquiring more information (Merz & Thieken, 2005). Considering model processes can also serve as a practical approach to identifying uncertainties (Beven et al., 2015). According to (Teng et al., 2017), the most relevant and extensively studied sources of uncertainty in flood inundation modelling, which are inherent to the model processes, include:

- Choice of model structures (Apel et al., 2009)
- Model parameters (e.g., friction parameters, conveyance parameters etc.) (P. D. Bates et al., 2004; Pappenberger et al., 2005; Romanowicz & Beven, 2003)

- Model inputs (floodplain and channel geometry, initial and boundary conditions such as inflow hydrographs and lateral inflow) (Abily et al., 2016; Pappenberger et al., 2008; Savage et al., 2016)
- Validation data (Stephens et al., 2012; Werner et al., 2005)
- Change in floodplain landscape over time (e.g., land use change) (Beven, 2011)
- Change in climate conditions (Neal et al., 2013; Vaze et al., 2011)

Sensitivity analysis are techniques that efficiently quantify the influence of uncertain drivers in a model, identifying those with the most significant impact and assigning them a rank or weight based on their influence (Hall et al., 2005). Sensitivity analysis can be categorized into two types: local sensitivity analysis and global sensitivity analysis. In local sensitivity analysis, parameters are altered individually around a specific point to evaluate their influence on the model output of interest (Tsubaki & Kawahara, 2013). Global sensitivity analysis evaluates the variation of all parameters together across their complete parameter space, thereby capturing the collective influence of each parameter averaged over all possible values of other input parameters. This approach enables the assessment of parameter interactions and their significance in relation to model predictions (Fieberg & Jenkins, 2005). In published sensitivity studies, uncertainties are often addressed through model calibration, with particular emphasis on friction parameters. Friction parameters are typically prioritized in sensitivity analyses due to their significant influence on the overall behaviour and outcomes of the system being studied. (Hall et al., 2005; Pappenberger et al., 2005). On the other hand, (Pappenberger et al., 2008) conducted a study on different global sensitivity analysis methods and found that it is impossible to define sensitivity in a unique way. Furthermore, these different methods can lead to variations in the ranking of the importance of model factors.

In flood inundation mapping, it is essential to embrace an inclusive approach to comprehending and addressing uncertainty. This entails examining uncertainty from multiple angles, including different methods, assumptions, and utilizing multiple models. It is important to acknowledge that the communication of uncertainty itself introduces uncertainty. A important aspect of uncertainty communication in flood inundation modelling is effectively conveying the meaning and significance of the outputs obtained from uncertainty analysis (Beven et al., 2015).

3 Methodologies

The methodology in this study is presented in Figure 2, outlining the sequential steps undertaken. Firstly, a study area is selected based on predefined criteria. Secondly, the terrain data, boundary conditions, and roughness values used in setting up the 2D HEC-RAS hydraulic model are defined, as well as the collection of calibration and validation data. Thirdly, the data processing methodologies are described, with a particular focus on flood delineation of SAR images. Fourthly, the setup of the 2D HEC-RAS hydraulic model is explained. Fifthly, the establishment of important parameters for executing the simulations is detailed. Lastly, the calibration and validation processes are explained, along with how the sensitivity analysis is performed and how the model performance of the models are evaluated.

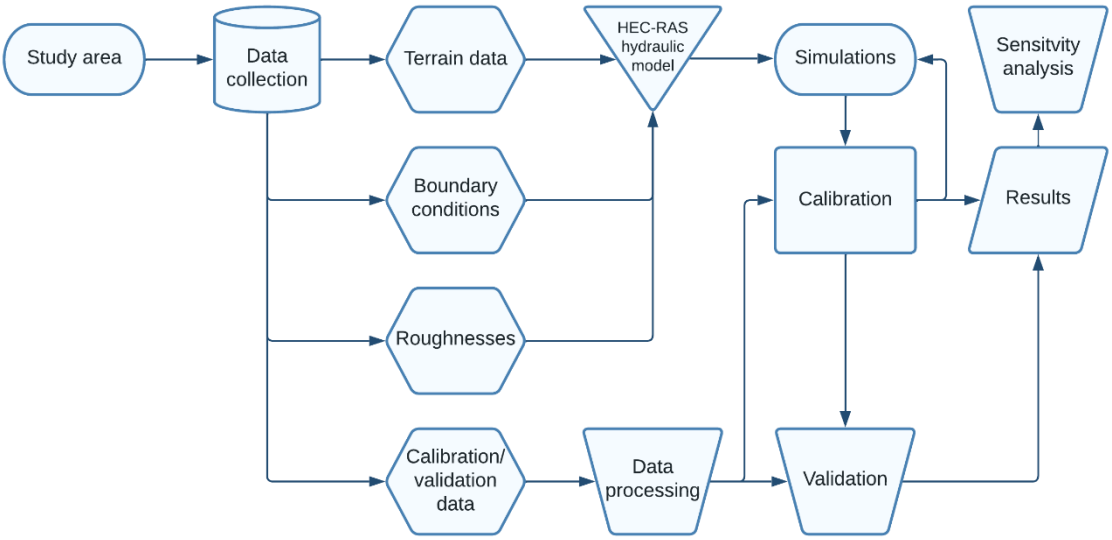

Figure 2 - Flowchart of methodology for hydraulic modelling.

3.1 Study area

In the thesis, one of the tasks was to locate real-world observation data for a suitable river that had both topographic LiDAR and bathymetric LiDAR data available. Potential sources of such data was identified in a report by (Alfredsen, 2022). This report highlighted rivers where bathymetric LiDAR data had been combined with topographic LiDAR data to create a comprehensive DEM of the entire river valley.

After identifying rivers with merged LiDAR data, the next step in the thesis involved investigating potential flood events in these rivers. To determine the flood events that had occurred since the launch of the Sentinel-1 mission on April 3, 2014, the Sildre [https://sildre.nve.no/] service provided by NVE was utilized.

To confirm if satellite images were available for the identified flood events, the Varsom Xgeo [https://xgeo.no/] tool was employed. Varsom Xgeo is a specialized tool designed for preparedness, monitoring and warning of flood, landslides, and avalanches. By using

Varsom Xgeo, changes in satellite images were observed and is displayed as flooded areas in the map. This information was essential for selecting suitable study areas for the thesis, as it ensured that there were SAR images available for downloading, that could be used in the calibration and validation processes.

Following the identification of the river with a significant number of available SAR images capturing various flood events, the Surna River was selected as the primary focus of the study.

The Surna River originates in Rindal municipality, located in Trøndelag county, Norway. The river flows through several municipalities, including Surnadal municipality in Møre and Romsdal county, situated in western Norway. Eventually, the river empties into the Surnadalsfjorden near the towns of Surnadalsøra and Skei. The Surna River begins at the confluence of the Lomunda and Tiåa rivers and has a gentle slope, extending for approximately 45 kilometers.

Moreover, the Surna River has its source in the mountainous regions of Trollheimen in the northeastern part of Møre and Romsdal county. It is fed by four smaller rivers, namely Rinna, Bulu, Folla, and Vindøla, all originating from Trollheimen. The majority of the river system is located within Surnadal and Rindal municipalities. It shares borders with the Søya and Todalselva rivers to the west, the Driva river to the south, the Orkla river to the east, and the Svorka and Bøvra rivers to the north. The drainage area of the river at its outlet is approximately 1200 km^2, and the mean annual specific runoff for the area is estimated to be 48 $l/s \cdot km^2$. The river system exhibits significant variations in elevation, ranging from sea level up to an elevation of 1668 meters above sea level. The highest point in the area is Snota, situated in the Trollheimen mountain range. The average elevation of the region is approximately 610 meters above sea level (Leine, 2018).

Currently, the catchment area is heavily regulated, with approximately 60% of the total precipitation affecting the Surna River system. The power plant system was established in 1968. As a result of this regulation, the Trollheimen power plant generates approximately 809 GWh of electricity annually, while the Gråsjø power plant produces around 73 GWh per year. One notable impact of the regulation is the significant reduction in the intensity of the annual spring floods in the regulated parts of the river system. (Ugedal et al., 2021).

On the other hand, the Surna River system experiences its largest floods during autumn, primarily due to heavy rainfall and often in combination with snow melting. The limited storage capacity of the reservoirs also plays a role in intensifying these floods, especially in the lower parts of the catchment area. The regulations in place have increased the prominence of autumn floods in the Surna River system compared to previous conditions. These autumn floods can be rapid and intense due to limited self-regulation in the unregulated parts of the catchment area. The presence of the two artificial reservoirs, Follsjø and Gråsjø, typically mitigates the floodwater from the eastern part of the catchment area. However, if the reservoirs are already full during the autumn period, their ability to dampen the floodwater is limited (Leine, 2018).

The study area in the Surna River starts from 112.27 Skjermo measuring station and goes down to Øye bru in Skei center, as illustrated in Figure 3.

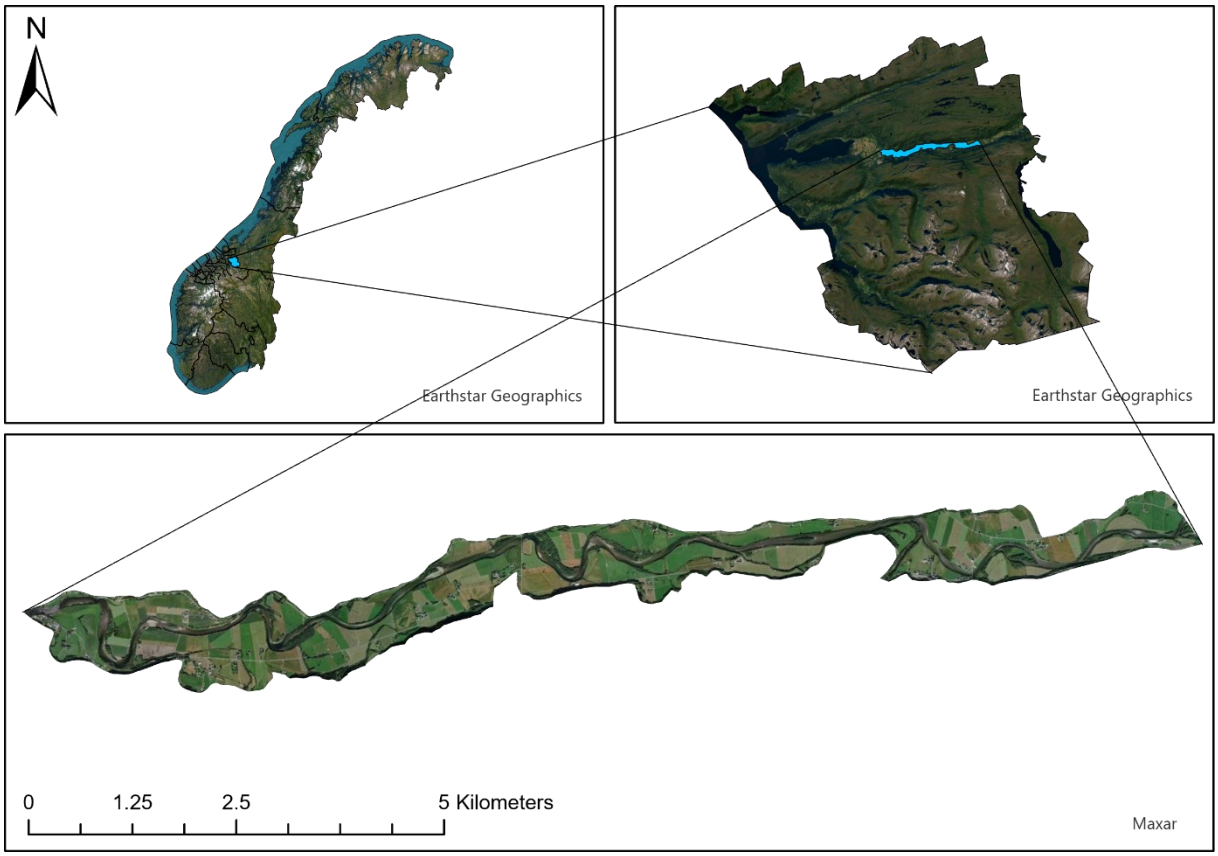

Figure 3: The study area located in Surnadal municipality, western Norway.

3.2 Terrain data

The terrain data used in the hydraulic model is a DEM generated in a study by (Awadallah et al., 2022) where they integrated bathymetric LiDAR data with topographic LiDAR data, respectively acquired through green and red LiDAR, as shown in Figure 4.

The bathymetric data retrieved from the green LiDAR has a resolution of 0.5 m, a point density of > 1.0 points/m^2, and was scanned with the laser RIEGL VQ-880-G. The scanning was done by AirborneHydroMapping GmbH (AHM) between 20 August 2016 and 26 August 2016, on a mission for the hydropower operator Statkraft (Sundt et al., 2021).

The topographic data retrieved from the red LiDAR has a resolution of 0.5 m, a point density of 2.0 points/m^2, and was scanned with the laser Leica ALS80. The scanning was done by TerraTec AS between 21 July 2016 and 8 October 2016 (Gulbrandsen, 2017).

Figure 4: DEM of study area with green LiDAR data merged with red LiDAR data.

3.3 Boundary conditions

Boundary conditions in HEC-RAS are being used to reflect physical constraints of the system being studied, in order to accurately model real-world scenarios. Hence, boundary conditions are the set of constraints that define the behaviour of the flow at the edges of the computational 2D domain in HEC-RAS. The flow behaviour at the boundaries of the system can have significant impact on the hydraulic dynamics throughout the entire system. Therefore, it is crucial to understand and carefully select the appropriate boundary conditions to ensure accurate modelling results.

Boundary conditions in HEC-RAS can be classified into three categories: external, internal, and global. External boundary conditions can be placed outside the 2D flow area, while internal boundary conditions can be placed anywhere inside the 2D flow area. Global boundary conditions provide meteorological data to the entire model, if being used. Different types of boundary conditions can be applied, such as flow hydrograph, stage hydrograph, normal depth, and rating curve.

Flow hydrograph used as external boundary condition can send flow in and out of the 2D flow area by applying positive or negative flow values. Stage hydrograph is an external boundary conditions that sends flow in and out of the 2D flow area based on the elevation of the ground. If the ground or water surface is lower than the stage, water will flow in; if the water surface is higher than the stage, water will flow out of the 2D flow area. Normal depth and rating curve are external boundary conditions that can only be used where flow leaves the 2D flow area, often being utilized as the downstream boundary condition. Internal boundary conditions can only be applied using the flow hydrograph as the boundary condition type (G. W. Brunner, 2023).

3.3.1 Upstream boundary condition

The upstream boundary condition for the 2D flow area is based on flow values from the gauging station 112.27 Skjermo. 112.27 Skjermo was established in 1986 as a replacement for the 112.7 Honstad gauging station, to measure the total discharge in the Surna River downstream of the Trollheimen power plant. The catchment area for 112.27 Skjermo is approximately 925 km^2 and includes most of the regulation system in the Surna River.

Although the station is located in a well-suited river profile, the quality of the stage-discharge curve has been assessed by a field hydrologist to be slightly below average. While the curve has been well measured, with two flood measurements taken during a large flood in 2016, there is some variation in the measurement basis for the curve (Leine, 2018).

The stage-discharge curve was updated in 2017 because of the flood measurements in 2016. This updated curve now provides significantly more water than the previous version due to new measurement technology ADCP (Acoustic Doppler Current Profiler), that provides more accurate results than traditional methods like using a current meter. However, the field hydrologist believes that the current curve may still underestimate the amount of water during large floods, and further improvements may be necessary to achieve better accuracy (Leine, 2018).

The placement of the upstream boundary condition was determined based on two different scenarios. In the first scenario the boundary condition was placed where the 112.27 Skjermo gauging station is located, to limit the uncertainty between water inflow between the boundary condition and gauging station. In the other scenario the 2D model

domain was extended approximately 370 m upstream of 112.27 Skjermo gauging station as shown in Figure 5. This was done in order to use an observed water surface elevation at 112.27 Skjermo from the August 14, 2003, flood event for calibration and analysis purposes.

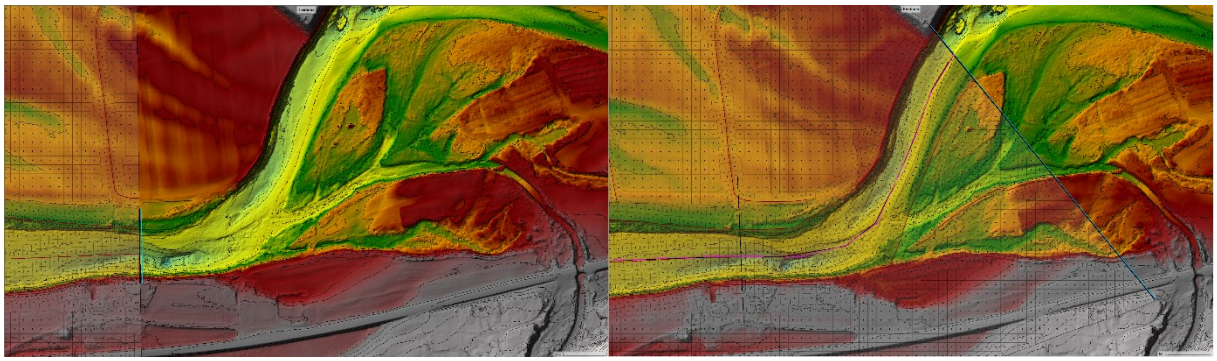

Figure 5: Upstream BC in 2D flow area (left: first scenario, right: second scenario).

The upstream boundary condition was defined with an external boundary condition using a flow hydrograph (discharge versus time) to bring flow into the 2D flow area, which is a required data for this boundary condition. The other required data is the energy slope for computing normal depth along the boundary condition line for each computational time step, using the given flow rate and underlying terrain data in the cross section. Once the normal depth of water is determined using the energy slope, a flow distribution is computed based on the normal depth water surface and the underlying terrain of the boundary condition line. This flow distribution is then utilized to assign the water flow to the cells along the boundary condition line that are wet. At every time step of the simulation, it is possible that only a section of the boundary condition line is wet, meaning that only those cells whose water surface elevation exceeds the elevation of their outer boundary terrain will receive water. A conveyance weighting approach is employed to send water to the cells, if all the cells along the boundary condition line is lower than the computed normal depth water surface (G. W. Brunner, 2023). Therefore, the width of the boundary condition line is also of relevance to simulate realistic flow situations along the boundary condition.

In accordance with (Robinson et al., 2019), it is considered good practice to position upstream boundary conditions at locations characterized by narrow floodplains and minimal hydraulic complexity. These locations exhibit hydraulic conditions that are closer to 1D flow, which better represents typical flow distribution. Moreover, this approach simplifies the estimation of inflow hydraulics. However, due to constraints in the vicinity of the 112.27 Skjermo measuring station, this ideal placement was not attainable.

To address this limitation, a sensitivity analysis was conducted, incorporating different energy slopes based on the bed slope in the proximity of the boundary condition. Unrealistic values with very steep slopes were also included to assess the tolerance of the model for such parameters. The energy slope values ranged from 0.0001 to 0.01, and Figure 6 illustrates the corresponding water surface elevation for each slope. The sensitivity analysis utilized the full shallow water equation, a Manning's n value of 0.06 across the entire 2D domain, and a flat hydrograph with a flow rate of 465.0 m^3/s.

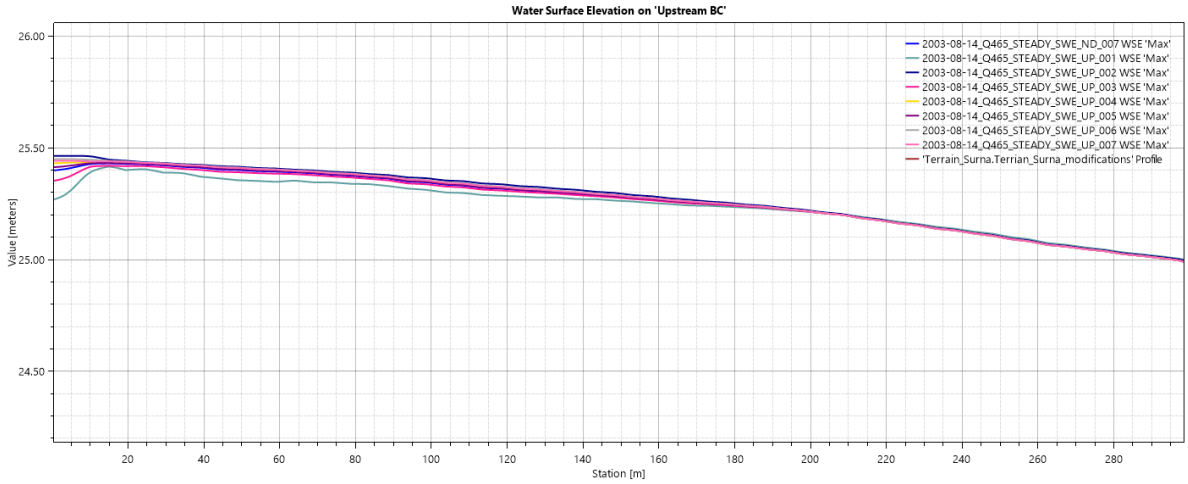

Figure 6: Water surface elevations from upstream boundary condition to 200 m downstream.

The results of the sensitivity analysis indicate that moving the area of interest approximately 220 m downstream from the upstream boundary condition will limit the uncertainty from the calculated energy slope in the flow hydrograph option. Thus, the water surface elevation will be normalized before reaching the 112.27 Skjermo gauging station and the analysis can be performed from this point. It also shows that both scenarios can be used. However, the first scenario must move the area of interest even further down the river reach before the analysis can be carried out. The energy slope used in the upstream boundary condition for further simulations was 0.0007, as it had the most natural slope on the water surface elevation from the sensitivity analysis results. Nevertheless, this value is not of significantly importance if the area of interest is moved far enough away from the boundary condition line but should be used within realistic values.

3.3.2 Downstream boundary condition

The Surna River has a relatively flat slope, implying that the downstream boundary condition can significantly impact the accuracy of model results. Therefore, to reduce uncertainties from the downstream boundary, the model should be extended further downstream from the study area (Robinson et al., 2019). In this case, the bathymetric LiDAR data in the DEM serves as the constraining component, so the downstream boundary condition was placed just upstream of the Øya bridge, where the LiDAR data ends as shown in Figure 7.

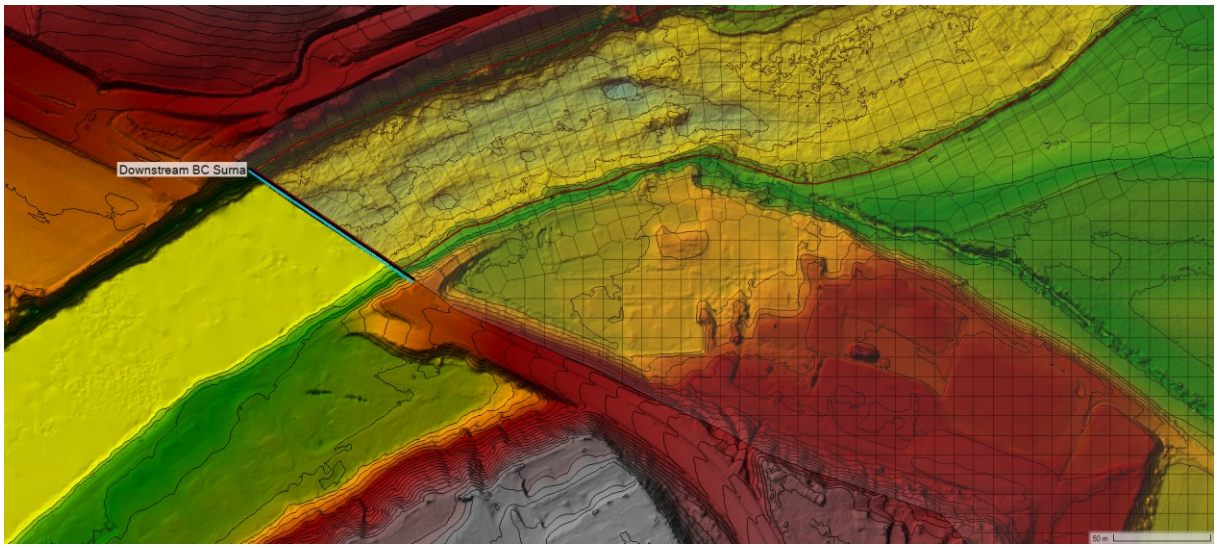

Figure 7: Downstream boundary condition using normal depth option.

If LiDAR data were available all the way to the fjord, the model area could have been extended, and a stage hydrograph could have been used to define the downstream boundary condition, potentially limiting uncertainty in the results by utilizing ocean tides.

There are no stream gauges in the region of the downstream boundary condition with known water surface elevations, so any stages for a given flow is not known. Therefore, the normal depth boundary condition was used. To compute water surface elevations for each given flow in the normal depth option, the friction slope (slope of the energy grade line) is used withing the Manning's equation to calculate the water surface elevation based on the cross section underneath the 2D boundary condition line (G. W. Brunner, 2023).

Normal depth assumes uniform flow conditions, but since it do not normally occur in naturals stream normal depth boundary condition should be placed far enough downstream from the study area to not have interference with the results (G. W. Brunner, 2016). Therefore, a sensitivity analysis was performed to see the effect of different friction slopes in water surface elevations upstream of the boundary condition as shown in Figure 8. The friction slopes used in the sensitivity analysis ranged from 0.0009 to 0.0450 and was based on water surface elevation downstream of the boundary condition derived from LiDAR data, average bed slope of the river reach, and bed slope in the river in the vicinity of the boundary condition line as suggested by (G. W. Brunner et al., 2023). The sensitivity analysis was run using the full shallow water equation, Manning's n value of 0.06 for the whole 2D domain, and a flat hydrograph with the flow of 465.0 m^3/s.

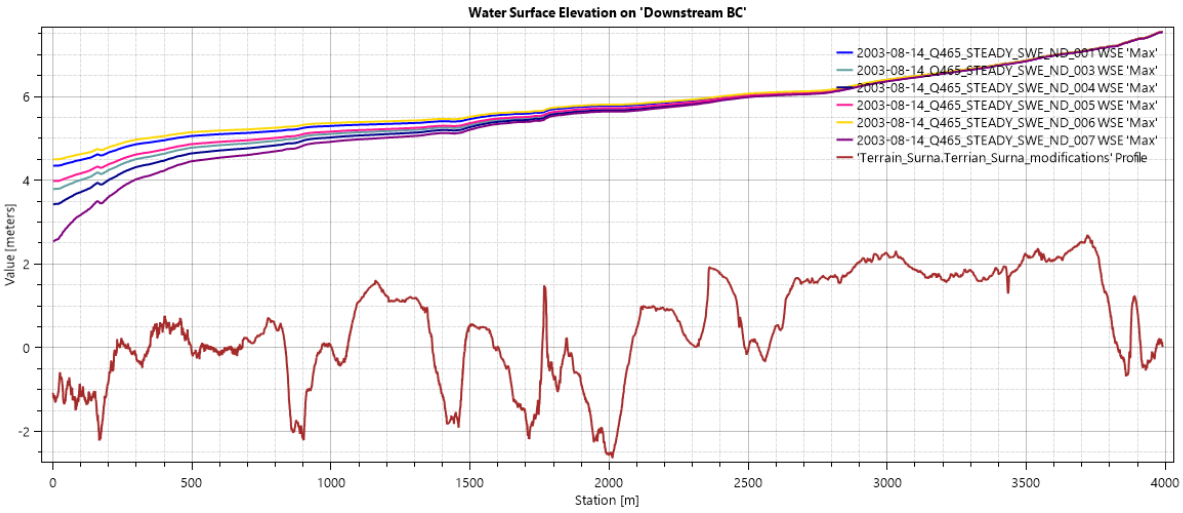

Figure 8: Water surface elevations from downstream boundary condition to 4000 m upstream.

The results of the sensitivity analysis indicate that moving the area of interest approximately 3000 m upstream from the downstream boundary condition will limit the uncertainty from the calculated friction slope in the normal depth option. This will also reduce the possibility for interference from ocean tides, as this can significantly impact water surface elevations. The friction slope of 0.0013, calculated from the average bed slope for the whole river reach was used in the normal depth boundary condition as suggested by (Goodell, 2010).

3.3.3 Lateral boundary conditions

The lateral boundary conditions in the model consist of all the tributaries that contribute to the total flow in the Surna River, and they are used as both external and internal boundary conditions. The largest and most influential tributary, the Vindøla River, is employed as the external boundary condition, while the smaller tributaries are used as internal boundary conditions.

In the development of the model a preliminary sensitivity analysis was performed to see the difference in the results between using external and internal boundary conditions for the small tributaries as shown in Figure 9. When using external boundary conditions, it is recommended to define the tributaries with refinement regions and breaklines with a smaller cell size than the 2D flow area to get a detailed description of the terrain from the edge of the model domain to the main river (G. W. Brunner, 2023). This to direct the water through the 2D domain without water spilling into other cells, which can lead to unrealistic flooded areas. On the other hand, when using internal boundary conditions, the flow into the perimeter can be placed anywhere, "dropping" water into the model at the cells where the internal boundary condition line crosses. The internal boundary condition lines were placed where the tributaries enter the main channel, and the tributaries was defined with a breakline with the same cell size as the 2D flow area.

No significant difference was observed in the flooded area when comparing the two methods in the model. As a result, internal boundary conditions were used, leading to shorter computational times due to reduced computational cell counts and possibility to use larger timesteps.

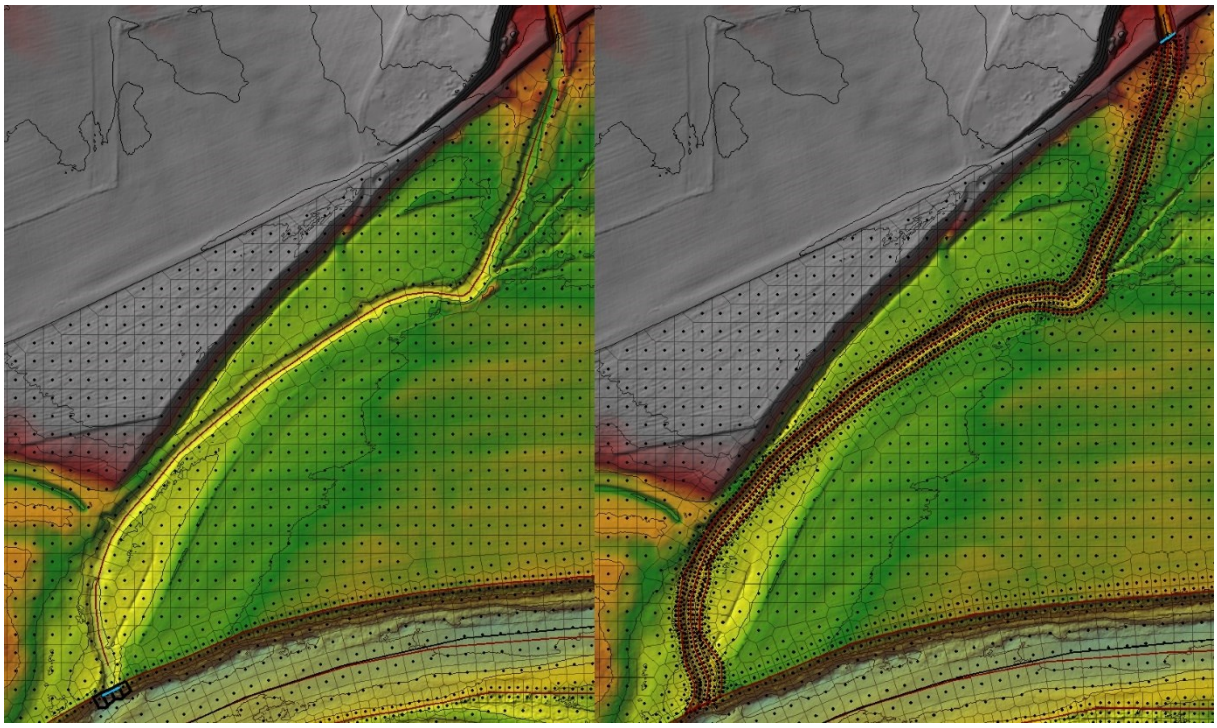

Figure 9: Left: Tributary with internal boundary condition. Right: Tributary with external boundary condition.

The Vindøla River was used as an external boundary condition as earlier mentioned, because of the size of the river compared to the other tributaries. It was placed downstream the Vindøla bridge, approximately 700 meters upstream of the confluence to the Surna River as shown in Figure 10. The purpose of this is to accurately simulate the flow dynamics when the Vindøla tributary merges with the main channel.

The energy slope for the external boundary condition was calculated based on the average bed slope from the boundary condition line and 400 meters downstream, which gave a value of 0.0049. The uncertainty in this value does not significantly affect the outcome of the calculation results, as the boundary condition is located high enough upstream in the river that the flow behaves normally before it reaches the Surna River.

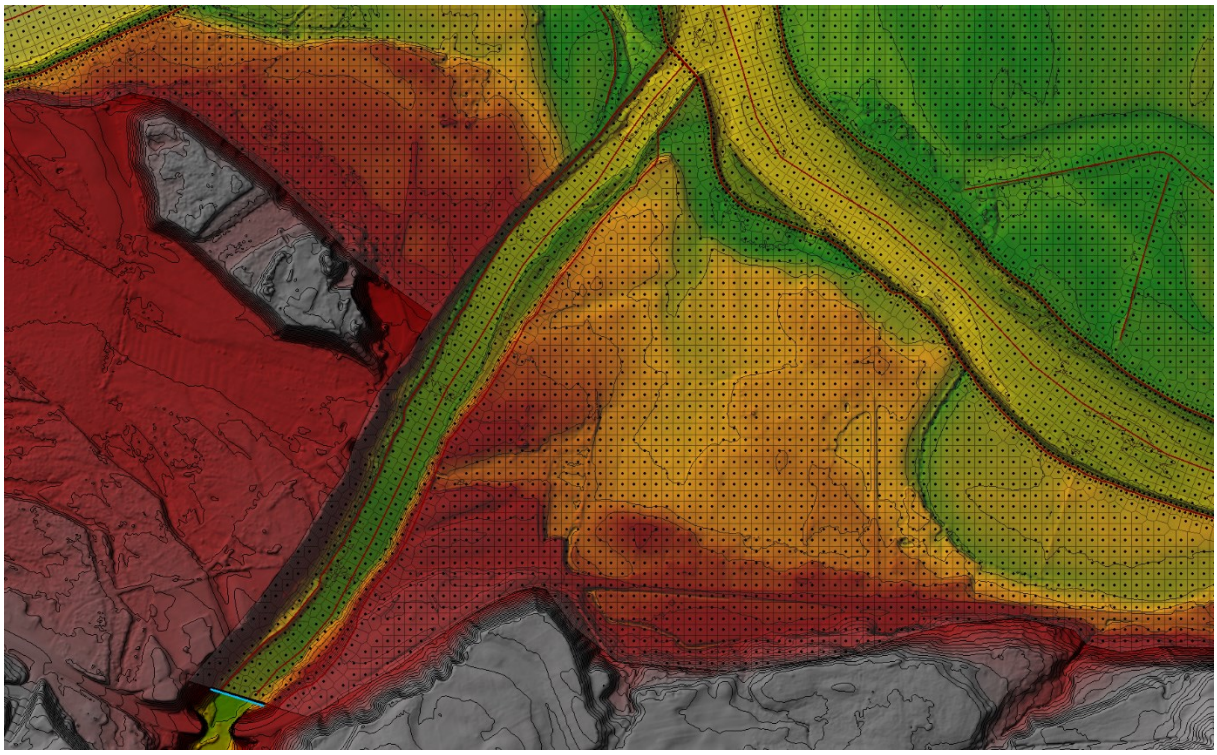

Figure 10: Vindøla tributary that enters the main channel with external boundary condition.

To calculate the contribution from the tributaries, scaling is a traditional method used in the practical fields in Norway and other countries (Faulkner et al., 2012; Fleig & Wilson, 2013). The scaling method is using a scaling factor to scale whole time series of flow from gauged to ungauged catchments, respectively the donor catchment and target catchment. The formulas used to scale flow time series is:

$$Q_T = scale\ factor * Q_D \quad (8)$$

$$scale\ factor = \frac{A_T * F_T}{A_D * F_D} \quad (9)$$

where Q_T is the discharge at the target location, Q_D is the discharge at the donor location, A_T is the area of the target catchment, A_D is the area of the donor catchment, F_T is the mean specific annual runoff of target catchment, and F_D is the mean specific annual runoff of donor catchment.

(Lobintceva, 2014) performed a study in seven catchments in central Norway where they compared the scaling method and regional modelling, where the scaling method got better results than the regional modelling in all catchments that where tested. However, there will always be uncertainties in predicting flow for ungauged basins.

The tributaries listed in Table 1 were scaled from the gauged catchment Rinna (Table 2), located in Rindal municipality in Trøndelag county. The gauging station 112.8 Rinna is the only measuring station in the Surna catchment that is not affected by regulations (Leine, 2018). Rinna was selected because it is the closest unregulated catchment with similar characteristics to the study area, meeting one of two assumptions required for the

scaling method. The other assumption is that the catchments must be located near each other and receive similar amounts of rainfall at the same time (Abdalla, 2019).

Table 1: Ungauged tributaries with the calculated scale factor and associated boundary condition number in the model.

Nr.	Name target	Q_N (l/s * km^2)	Area (km^2)	Scale factor
2	Bergemsbekken	35.3	0.4	0.004
	Bergåa	38.2	3.5	0.036
3	Hommelstadbekken	39.5	3.2	0.034
4	Storbekken	37.3	2.6	0.026
5	Lekkaren	46.1	1.6	0.020
	Brøskjåa	42.9	7.7	0.090
6	Sollibekken	31.9	0.5	0.004
7	Lomtjønna	34.7	0.8	0.008
8	Tjuvevja	34.1	1.1	0.010
9	Sverkestykket	36.0	2.4	0.024
10	Talgøya	44.4	6.3	0.076
11	Røstigbekken	37.4	0.6	0.006
	Ranesbekken	50.0	6.8	0.093
12	Honnestadfossen	50.6	10.0	0.138
13	Sprenbekken	34.5	1.3	0.012
14	Sagbekken	44.8	5.2	0.064
15	Storøra	31.4	1.0	0.009
16	Vindøla	68.3	95.0[1]	1.770
	Fergemannshølen	33.0	0.3	0.003
	Småøyan	33.4	0.8	0.007

Table 2: Unregulated gauged catchment used for scaling.

Name donor	Q_N (l/s * km^2)	Area (km^2)	Scale factor
Rinna	41.2	89.0	-

The tributaries were, in general, very small, except for the Vindøla River. Consequently, certain tributaries were combined. Figure 11 illustrates all the boundary conditions in the model, with the merging of several tributaries, such as the combination of Bergemsbekken and Bergåa (2), Lekkaren and Brøskjåa (5), Røstigbekken and Ranesbekken (11), and Fergemannshølen and Småøyan with the Vindøla River (15). Additionally, the boundary condition (0) corresponds to the downstream boundary condition, while (1) represents the upstream boundary condition.

[1] The Vindøla River catchment area is a total of 169.0 km^2, but due to 74.0 km^2 of the upper part is transferred into 112.27 Skjermo catchment area, the area used for scaling is 95.0 km^2 (Leine, 2018).

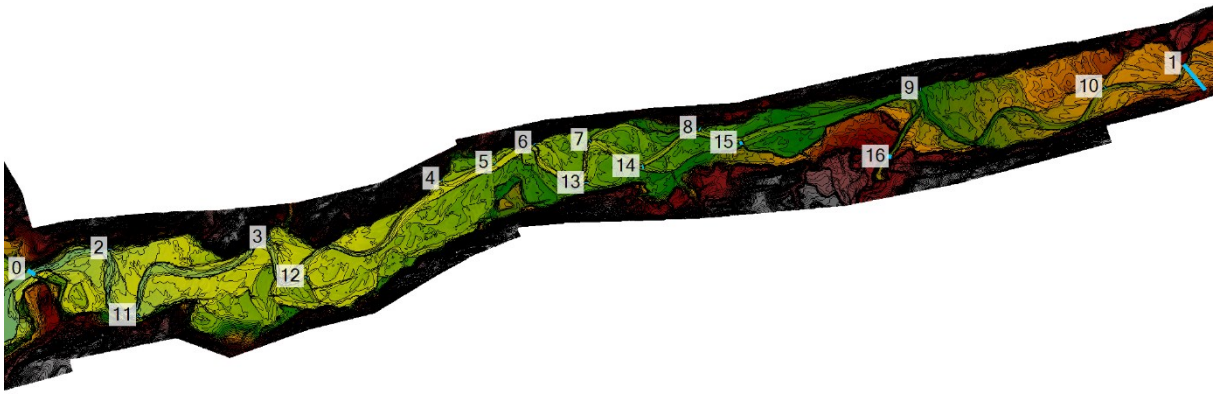

Figure 11: Overview over all the boundary conditions in the model.

The transmission capacity from the upper part of the Vindøla River catchment area to Gråsjø that is in the 112.27 Skjermo catchment area is a total of 27.5 m^3/s (Multiconsult, 2010), and under high flood conditions the uncertainty of this transmission can be very large. Therefore, an alternative to the scaling method for calculating the discharge from the Vindøla River was made.

As said before, the Vindøla River is the largest tributary of the Surna River, making it the lateral boundary condition with the most significant influence on the results. In a flood estimation study by (Leine, 2018), peak flow discharges were calculated for floods with different recurrence intervals at 13 different locations, including upstream and downstream of the confluence of the Vindøla River, and gauging station 112.27 Skjermo. Based on these values, a linear regression analysis was performed with respect to 112.27 Skjermo and downstream the inflow from the Vindøla River, which includes the inflow of water between these points. The tributaries Fergemannsholen and Småøyan are already accounted for in the boundary condition for the Vindøla River, but since Talgøya is an internal boundary condition, its calculated discharge must be subtracted from the calculated discharge of the Vindøla River.

Two linear regression formulas were created, one for discharge values under 513 m^3/s:

$$Q_{Vindøla} = 0.3279 * Q_{112.27\ Skjermo} - 17.206 \quad (10)$$

and one for discharges values over 513 m^3/s:

$$Q_{Vindøla} = 0.1441 * Q_{112.27\ Skjermo} + 116.74 \quad (11)$$

where $Q_{Vindøla}$ is the discharge at the Vindøla River external boundary condition, and $Q_{112.27\ Skjermo}$ is the discharge at 112.27 Skjermo gauging station.

The explanation for using two different regression formulas is that between mean annual flow and a return period of 20 years the transmission from the upper part of Vindøla catchment is accounted for, making Vindøla a regulated catchment. From a return period of 50 years until 1000 years, its estimated as an unregulated catchment area (Leine, 2018).

3.3.4 Area of interest based on sensitivity analyses

The sensitivity analyses conducted on the upstream and downstream boundary conditions revealed the extent of their influence in the model. To reduce uncertainty stemming from these boundary conditions, a specific area of interest within the 2D model domain was identified. This defined area of interest, depicted in Figure 12, was used for all subsequent analyses and results in the study, ensuring a focused and consistent evaluation within a controlled region.

Figure 12: Area of interest inside the 2D flow area from the hydraulic model in HEC-RAS, with the border of the land photo defining the extent of the 2D flow area.

3.4 Roughnesses (Manning's n-values)

In hydraulic models, the roughness of surfaces is one of the most significant factors that impact the flow of water. Thus, understanding the roughness of the land cover and its effect on the flow of water is essential for accurate flood inundation modelling. The roughness coefficient, represented by Manning's n-value, is used to quantify the surface roughness of different land covers. Accurately representing the surface roughness of different land covers is therefore essential in predicting the and mitigating the impacts of floods.

The land cover map used to provide Manning's n-values for the different land cover types as defined by NIBIO (Norwegian Institute of Bioeconomy Research), was downloaded from Geonorge.no [https://www.geonorge.no/] (accessed on March 10, 2023) as shown in Figure 13.

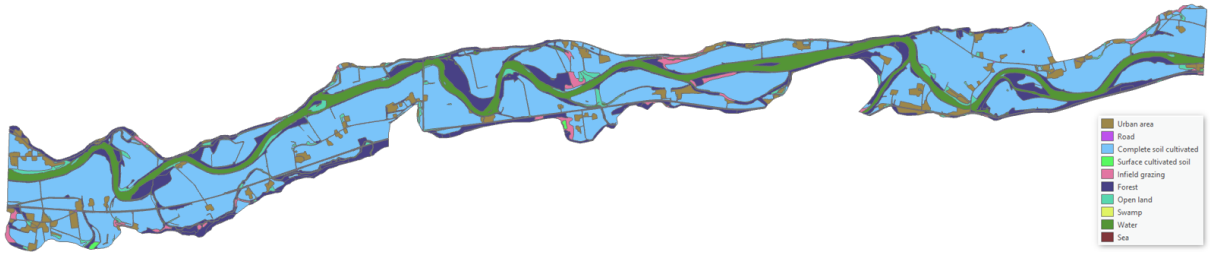

Figure 13: Land cover map of area of interest.

The land cover map developed by NIBIO is called AR5 and is a classification system that divides the land surface into different types of land cover based on criteria such as vegetation and land use (Ahlstrøm et al., 2019). To give specific Manning's-n values to the model either a land cover layer or user defined polygons can be used to define various roughness values in the 2D flow area. Therefore, the AR5 land cover map was used to create a spatially land cover layer in RAS Mapper with a cell size of 5 meters. Once created, a table of land cover versus Manning's n-values was made and associated with the geometry file(s).

Complete soil cultivated, surface cultivated soil, and infield grazing (pasture) are land cover types that refer to different forms of land use. Complete soil cultivation refers to an

area where the soil has been fully tilled and used for agricultural purposes. Surface cultivated soil, on the other hand, refers to an area where the soil has been partially tilled and used for agricultural purposes, and the remaining vegetation provides some roughness. Infield grazing refers to an area where livestock are allowed to graze, resulting in a mixture of vegetation and soil cover. Overall, these land cover types have different hydraulic properties and affect flow resistance in different ways, but it can be useful to combine them into a single roughness group to simplify the calibration process. (Te Chow, 1959) states that the Manning's n-value range from 0.025 and 0.050 in pasture areas, and from 0.020 to 0.050 in cultivated areas. Studies have used Manning's n-values as high as 0.1 for floodplains (Horritt & Bates, 2002).

Forest as a Manning's n-value can vary depending on factors such as tree density, canopy cover, and the type of vegetation under the trees. The forests surrounding the Surna River mainly consists of deciduous forest as shown in Figure 14. According to (Te Chow, 1959) trees with straight dense willows at the summer has Manning's n-values ranging from 0.110 to 0.200. (G. W. Brunner, 2023) describes deciduous forest as areas with trees mostly greater than 5 meters tall, and a total vegetation cover greater than 20 %. Seasonal change is a significant factor in the Norwegian climate and according to the description, more than 75% of tree species must shed foliage simultaneously in response to seasonal changes. Hence, the Manning's n-value range from 0.100 to 0.200 in his description will most likely represent the forest surrounding the Surna River.

Figure 14: Picture of the Surna River in upper Surnadal (Melby, 2019).

Open land is areas that do not fit into other defined categories, such as urban or agricultural land. This land cover type can be classified as developed, open space areas with a mostly vegetation in the form of lawn grasses, and a mixture of some constructed materials, where less than 20 % of the total cover is impervious surfaces. The Manning's

n-value is according to (G. W. Brunner, 2023) ranging between 0.03 to 0.05 in developed, open space.

Water is a land cover type in AR5 that includes lakes, rivers, and streams. In the study area there are no lakes, and only a few insignificant small streams in relation of contribution to the total water area. The land cover type mainly consists of the Surna River, which is a natural river with a width ranging from approximately 40 m to 150 m in the study area. The riverbed between the Trollheimen powerplant and the fjord is mainly composed of gravel, which covers 53 % of the total area, and rocks, covering 25 %. Sand is also present in significant amounts (14 %) between the gravel and rocks. Additionally, boulders are commonly found along the riverbanks, with a coverage of 4 % (Gabrielsen et al., 2017). According to (Fergus et al., 2010) natural rivers that are over 30 meters wide can have Manning's n-value between 0.025 and 0.1. (Barnes, 1967) did an evaluation of roughness characteristics of natural channels and found Manning's n-values between 0.024 and 0.075. (Te Chow, 1959) defines mountain streams with no vegetation in channel, banks usually steep, trees and brush along banks submerged at high stages. He separates the bottom conditions with different Manning's n-values, were a bottom with gravel, cobbles and few boulders have n-values between 0.030 and 0.050. Cobbles with large boulders have Manning's n-values between 0.040 and 0.070.

Urban area is a land cover type that can be classified as developed with low intensity in the study area, since most of the area in the floodplains include single-family housing units. That implies that 20 % to 49 % of the total cover is impervious surfaces and is a mixture of constructed materials and vegetation. Manning's n-value for this land cover type range between 0.06 and 0.12 according to (G. W. Brunner, 2023).

Roads in the study area are both asphalt and gravel roads, but do not represent a significant part of the total area. Therefore, the roads are defined as asphalt surface, where the Manning's n-value can range from 0.013 to 0.016 according to (Te Chow, 1959).

Although swamp and sea are land cover types included in AR5, they are not present in the study area and therefore will not be discussed further.

The range of Manning's n-values for different land cover types based on the presented sources used in the model calibration is listed in Table 3.

Table 3: Manning's n-values min and max values based on land cover types.

Class	Land cover type	Area (km^2)	Area (%)	Manning's-n min	Manning's-n max
21	Complete soil cultivated	5.19	60.4	0.020	0.100
22	Surface cultivated soil	0.01	0.1	0.020	0.100
23	Infield grazing (pasture)	0.13	1.5	0.020	0.100
30	Forest	1.32	15.4	0.100	0.200
50	Open land	0.28	3.3	0.030	0.050
81	Water (Main channel)	1.05	12.2	0.020	0.100
11	Urban area	0.42	4.9	0.060	0.120
12	Road	0.19	2.2	0.013	0.016

3.5 Calibration & validation data

3.5.1 Copernicus Data Space Ecosystem

Copernicus Data Space Ecosystem is a new service launched in January 2023, that gives free user access to large amounts of data from the Copernicus Sentinel satellites from Earth observations. Researchers, businesses, and institutions can use this as a powerful tool to analyse, stream, download, visualize, and discover data with the next level of data processing and distribution infrastructure. (*Ecosystem | Copernicus Data Space Ecosystem*, n.d.)

This service can be used to see if there were any Sentinel-1 satellites above the area of interest at the time of the flood event. The area of interest must be marked, and the time range of the event needs to be specified. The data source that is going to be used for flood delineation is a Sentinel-1 C-SAR Level-1 GRD image. All the available products will be listed with sensing time, product information and possibility to download the product for further analysis.

Table 4 presents an overview of the satellite passes over the study area during the flood events that aligned with the active period of the Sentinel-1 program. The acquired SAR images from November 26, 2016, January 21, 2020, and November 24, 2021, demonstrated significant potential in terms of capturing flooded areas. These SAR images were subsequently employed in the delineation of flood extents, forming an integral part of the calibration and validation process for the 2D hydraulic model.

Table 4: Sentinel-1 satellites with time of SAR imagery capture and the discharge at 112.27 Skjermo when the image was taken.

Satellite	Time of peak	Peak discharge (m^3/s)	Time of SAR imagery capture	Image discharge (m^3/s)
Sentinel-1A	2016-11-25 23:00	451	2016-11-26 05:47	215
Sentinel-1B	2016-12-05 05:00	388	2016-12-04 16:46	–
Sentinel-1B	2016-12-09 11:00	358	2016-12-09 16:54	-
Sentinel-1B	2020-01-21 03:00	356	2020-01-21 05:54	289
Sentinel-1A	2021-11-24 03:00	583	2021-11-24 05:47	420

3.5.2 Copernicus Emergency Management Service

The Copernicus Emergency Management Service (CEMS) is a service that supports decision-making during natural and man-made disasters. The service uses geospatial data and images from satellites from the Copernicus Programme to provide timely information and analysis for effective emergency management. CEMS constantly monitors Europe and the world for signs of potential disasters and provides critical insights to help responders and authorises take prompt action. (*What Is Copernicus | COPERNICUS EMERGENCY MANAGEMENT SERVICE*, n.d.)

One of the services CEMS deliver is Rapid Mapping products, which provides geospatial information and data within a short timeframe in the immediate aftermath of a disaster, usually within hours or days of a service request. The Rapid Mapping product can be requested by a diverse range of users at different levels, including regional, national, European, and international entities and organizations involved in emergency management. Although the service only can be requested by a certain type of

stakeholders, the Rapid Mapping products generated from these requests are freely available and accessible for download. The Rapid Mapping products typically include maps and imagery that provide a visual representation of the affected areas, highlighting key features such as damage assessment, infrastructure status, and potential risks. (*The Emergency Management Service - Mapping | COPERNICUS EMERGENCY MANAGEMENT SERVICE*, n.d.)

One of the key components of the Rapid Mapping product is the delineation feature, which offers an evaluation of the extent and impact of the event. In the context of flood mapping services provided by CEMS, this feature utilizes satellite imagery to swiftly capture and assess the flooded areas following an emergency event.

On January 12, 2022, the western and central parts of Norway were bracing for the impact of Storm Gyda, a severe weather event characterized by warm temperatures, strong winds, and heavy rainfall. In anticipation of potential flooding caused by the combination of snow melt and rainfall, the Directorate for Civil Protection and Emergency Planning (DSB) activated the Rapid Mapping service. As a result, delineation products were generated for several rivers in the potentially affected areas, including the Surna River in Surnadal. The Emergency Management Service Rapid Mapping (EMSR) product for the Surna River can be found in Appendix 1.

The EMSR product includes vector data depicting the delineation of the flood extent caused by Storm Gyda. This information was obtained through satellite imagery captured by a COSMO-SkyMed mission satellite, which is part of the Copernicus Programme. To generate the flood delineation vector data, SAR imagery from the COSMO-SkyMed mission, as indicated in Table 5, was specifically utilized.

Table 5: Copernicus Programme satellite with time of SAR imagery capture and the discharge at 112.27 Skjermo when the image was taken.

Satellite mission	Time of peak	Peak discharge (m^3/s)	Time of SAR imagery capture	Image discharge (m^3/s)
COSMO-SkyMed	2022-01-13 16:00	692	2022-01-13 17:21	657

This SAR image played a crucial role in accurately outlining the extent of the flood-affected areas, illustrated in Figure 15. The flood delineation map was subsequently employed in the calibration and validation process of the 2D hydraulic model.

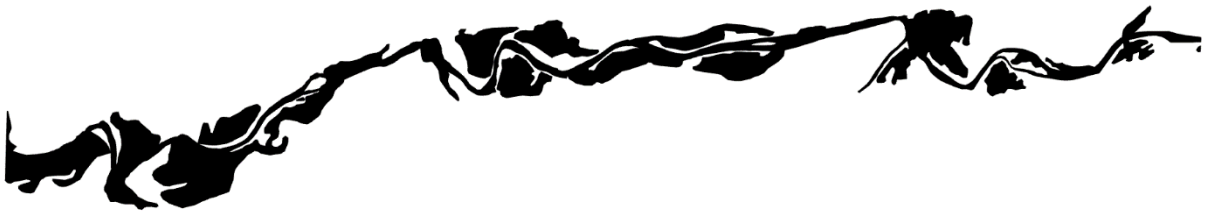

Figure 15: Vector data depicting the delineation of the flood extent caused by Storm Gyda.

3.5.3 SR16 forest resource map

The SR16 forest resource map is a comprehensive dataset that offers an overview of the distribution of the forest resources in Norway. It provides detailed information regarding

the extent of forest cover, as well as various characteristics such as tree species composition, forest volume, and other relevant parameters.

The SR16 dataset is created using advanced automated processes that integrate various data sources, including 3D remote sensing data (such as photogrammetry and LiDAR), terrain models, satellite data, existing map data (AR5), and information from the National Forest Inventory. Laser data from the Norwegian Detailed Elevation Model and Sentinel-2 imagery are fundamental datasets utilized in the development of SR16.

SR16 is divided into two parts: SR16R, a raster map, and SR16V, a vector map. SR16R consists of pixels with a resolution of 16 x 16 meters, while SR16V comprises polygons that represent homogeneous forest areas, derived from the pixel data. The attributes in SR16V are primarily calculated as averages of the corresponding pixel values in SR16R (*Skogressurskart (SR16) - Nibio*, n.d.).

The SR16V map, illustrated in Figure 16, was downloaded from Geonorge.no [https://www.geonorge.no/] (accessed on May 9, 2023), and was used to represent the flooded areas that were not identified in the flood delineation of the SAR images.

Figure 16: SR16V vector map clipped inside the area of interest.

The SR16V forest resource map was spatially clipped to include only the areas within the predicted flood inundation area generated by the model. This clipped SR16 map was then merged with the binary maps derived from the flood delineation of the Sentinel-1 SAR images and the delineated vector data obtained from COSMO-SkyMed SAR imagery. It played a crucial role in the calibration and validation processes by providing a reference to compare against the simulated flood extent generated by the model. This comparison helped assess the accuracy and performance of the model in accurately reproducing the observed flood extent.

Figure 17 provides a visual representation of the methodology employed in this process. In (a), the simulated flood inundation area is depicted in black, with the vector data obtained from the Storm Gyda flood event on January 13, 2022, overlaid in blue. Moving to (b), the same information from (a) is presented, with the addition of the clipped SR16 map displayed in pink. Upon observing the black areas in (a) that indicate the flooded areas, it is highly plausible that these areas are indeed flooded, especially when compared to the forest areas clipped in (b).

This observation aligns with previous research, which highlight the challenges of using SAR imagery to detect and map flooded areas in vegetated environments. Vegetation can attenuate and scatter the SAR signal, making it difficult to differentiate between flooded areas and dense vegetation. As a result, accurate identification and delineation of flooded areas in such regions require careful analysis and integration of different data sources and techniques (Horritt et al., 2003).

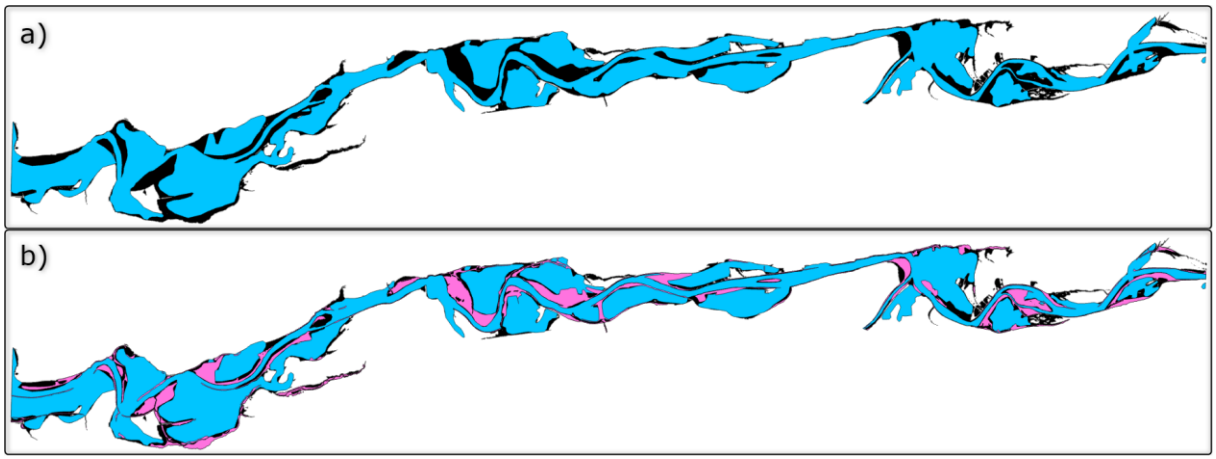

Figure 17: Storm Gyda flood event January 13, 2020. In (a), black represents the simulated flood inundation area, blue is the vector data from the flood delineation of the flood event, and in (b) pink is the SR16 clipped inside the simulated flood inundation area.

3.5.4 Observed flood water levels

In collaboration with Surnadal municipality, NVE conducted a post-flood survey to measure the water levels following a flood event on August 14, 2003. The survey was carried out immediately after the flood and is considered to be of high quality. The recorded values, listed in Table 6 (Bævre & Øydvin, 2007), were originally based on the NN54 reference system but have been adjusted to the more recent NN2000 reference system for consistency and compatibility with the data of the study and analysis. The survey mark data used to transform the water levels to NN2000 was collected from norgeskart.no [https://www.norgeskart.no/] (accessed on March 29, 2023). Figure 18 illustrates the profile lines from Table 6, with their profile line number.

Table 6: Flood water levels from the flood event August 14, 2003 (Bævre & Øydvin, 2007).

Profile line	Flood water levels at 465 m^3/s discharge (Skjermo) [masl NN54]	Survey mark ID	Difference NN54 to NN2000	Flood water levels at 465 m^3/s discharge (Skjermo) [masl NN2000]
1	5.96	E26N0079	+ 0.055	6.02
2	7.95	E26N0047	+ 0.056	8.01
3	7.93	E26N0047	+ 0.056	7.99
4	10.27	E26N0048	+ 0.057	10.33
5	11.93	E26N0049	+ 0.058	11.99
6	15.30	E26N0051	+ 0.061	15.36
7	17.20	E26N0051	+ 0.061	17.26
8	19.08	E26N0052	+ 0.062	19.14
9	21.05	E26T0238	+ 0.063	21.11
10	23.78	E26N0053	+ 0.063	23.84

Figure 18: Profile Lines 1 - 10 with observed water levels inside the area of interest.

3.6 Flood delineation from Sentinel-1 SAR imagery

Flood delineation from Sentinel-1 SAR imagery involves the process of identifying the extent and boundaries of flood-affected areas using image processing techniques. This process includes pre-processing of the SAR imagery, followed by the application of a thresholding technique, used to take advantage of the contrasting backscatter properties between water and non-water surfaces presented in the SAR imagery. The sequence of the different steps of the process is shown in Figure 19.

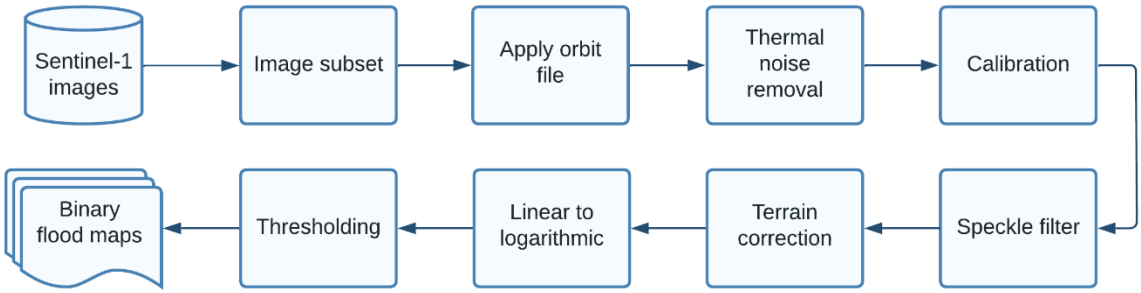

Figure 19: Flowchart of methodology for flood delineation from Sentinel-1 SAR imagery.

The tool to perform these processes is the Sentinel-1 Toolbox 9.0.3 (S1TBX) that is a plugin for the SNAP 9.0.0 (released 2022-06-29) (SeNtinel Applications Platform) which are a free and open-source software developed by the European Space Agency (ESA). S1TBX provides a wide range of functionalities for SAR data analysis. These includes pre-processing tools, polarimetric and interferometric analysis capabilities, data product readers and writes, visualization and analysis tools, and support for third-party SAR data (*Toolboxes*, n.d.).

The Sentinel-1 mission had several passes over the study area during some of the major floods that occurred between 2014 and 2022 (as previously listed in Table 4). Table 7 provides a list over which of these SAR images that were used for processing and flood mapping, with additional specifications.

Table 7: Specifications of Sentinel-1 SAR images used for flood mapping.

Satellite	Acquisition time	Acquisition mode	Product type	Polarization	Pixel spacing
Sentinel-1A	2016-11-26 05:47	IW	GRD	VH + VV	10x10 m
Sentinel-1B	2020-01-21 05:54	IW	GRD	VH + VV	10x10 m
Sentinel-1A	2021-11-24 05:47	IW	GRD	VH + VV	10x10 m

The first thing that was done after loading the SAR image into S1TBX was using the function image subset. Image subset is used for extracting a smaller portion of an SAR image to only focus on the specific area of interest within the image illustrated in Figure 20. This was done to reduce the size of the SAR images, since files are over 1.5 GB in a full-sized SAR image. Other advantages of cropping the images are faster computations times, and more pixels that are flooded, making it easier to find threshold values between flooded and non-flooded areas.

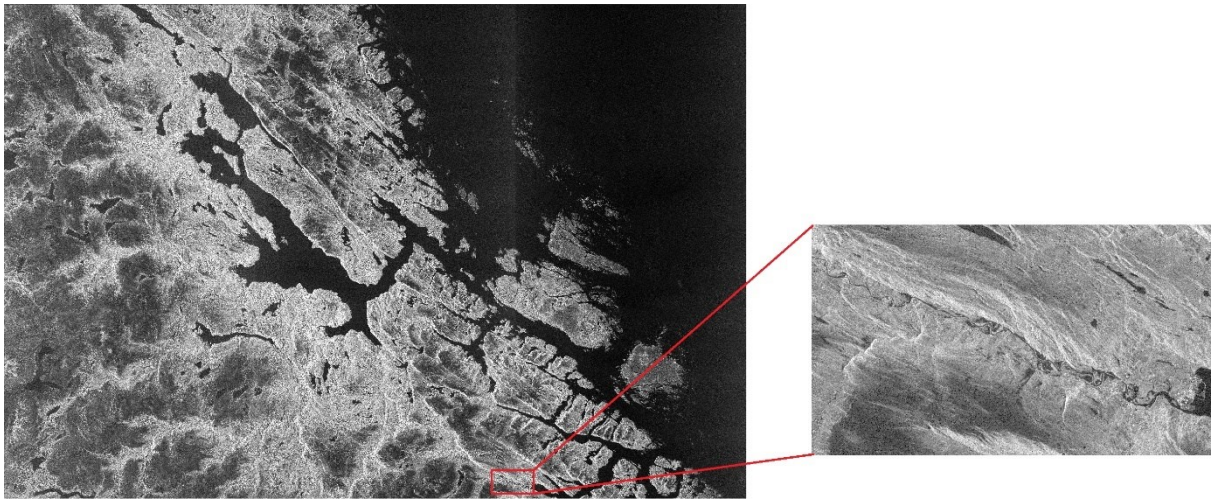

Figure 20: Sentinel-1 SAR full image with subset image representing area of interest.

The orbit state vectors in the metadata information of the SAR products are not always accurate when the product is generated. To compensate for this, precise orbits of the satellites are determined after a few days and made available a few days to weeks after the generation of the product. So, the function apply orbit file was used to receive these precise orbit files to provide more accurate information about the position and movement of the satellite at the time of image acquisition (Filipponi, 2019).

Image intensity in Sentinel-1 SAR images is caused by random fluctuations in the electronics due to temperature change, particularly in the cross-polarization (Park et al., 2017). This can introduce a radiometric bias in the backscatter, that can disproportionately affect pixels with low backscatter values, such as water bodies or flooded areas. Therefore, the thermal noise removal function was used to reduce the noise effect and normalize the backscatter signal in the Sentinel-1 SAR images.

Calibration is a radiometric correction process that was used to convert SAR integer digital numbers (DN) to backscatter coefficients, which represents the radar backscatter intensity in each pixel of the surface (sigma nought). The calibration process is necessary because Sentinel-1 SAR images often contains significant radiometric bias that can affect the accuracy of quantitative analysis (Mangidi et al., 2023). The Sentinel-1 GRD product includes a calibration vector with image intensity values that allows for the conversion into backscatter coefficient using a calibration equation (Filipponi, 2019).

Speckle in SAR images is caused by the interference of electromagnetic waves that are scattered by the surface being imaged (Park et al., 2017). Speckles can be described as random, granular pattern of bright and dark pixels that are not necessarily indicative of the true scattering properties of the surface. Speckle can produce a wide range of pixel values that appear as noise in the image, that can lead to misclassification, making it difficult to interpret. S1TBX provides several speckle filters that are designed to reduce

the impact of speckle in SAR images. These filters work by applying mathematical operations to the image data to smooth out the noise caused by speckle while preserving the important information about the underlying scattering properties of the surface. The filters available in S1TBX range from simple linear filters like Lee and Frost filters to more complex non-linear filters like Gamma Map, each with their own strength and weaknesses for different types of imagery. (Rana & Suryanarayana, 2019) did a study where they evaluated de-noising methods for SAR images. The results indicated that the Lee filter 3 x 3 kernel size provided a good balance between preserving image features and reducing speckle noise compared to other filters. Therefore, it was selected as the preferred speckle filter when pre-processing the Sentinel-1 SAR images as shown in Figure 21.

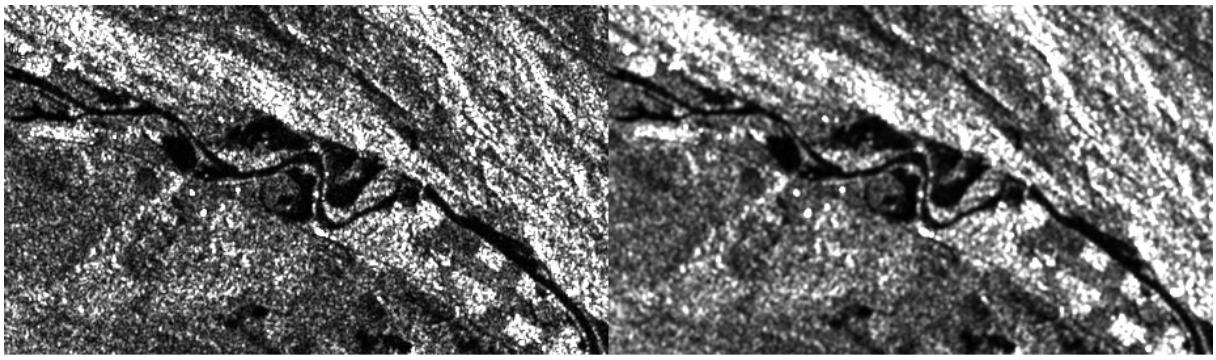

Figure 21: Sentinel-1 SAR image with VV polarization of flood event from November 24, 2021. Left: Before applying speckle filter. Right: After applying Lee 3 x 3 speckle filter.

The satellite reference system is defined with respect to the orbit of the satellite at a specific point of time. Hence, applying terrain correction is to set a geographic reference system to the pixels from the satellite reference system. Terrain correction also corrects the geometric distortion that are caused by topography in SAR images. This correction compensates for distortions such as foreshortening and shadows, caused by the varying viewing angle of SAR data acquisition (Selmi, 2021). Range Doppler Terrain Correction utilizes orbit state vector information, radar timing annotations, and slant to ground range conversation parameters along with a reference digital elevation model to accurately project the image pixels onto a georeferenced system (Filipponi, 2019), and was used to ensure precise geolocation data using the Range Doppler orthorectification approach (Small & Schubert, 2008). The digital elevation model used in the Range Doppler Terrain Correction was the ASTER 1sec GDEM downloaded from ASTER Global Digital Elevation Model [https://gdemdl.aster.jspacesystems.or.jp/] (accessed on February 6, 2023), and map projection were set to UTM / WGS 84 for having x- and y-coordinates in a 2D coordinate system as shown in Figure 22.

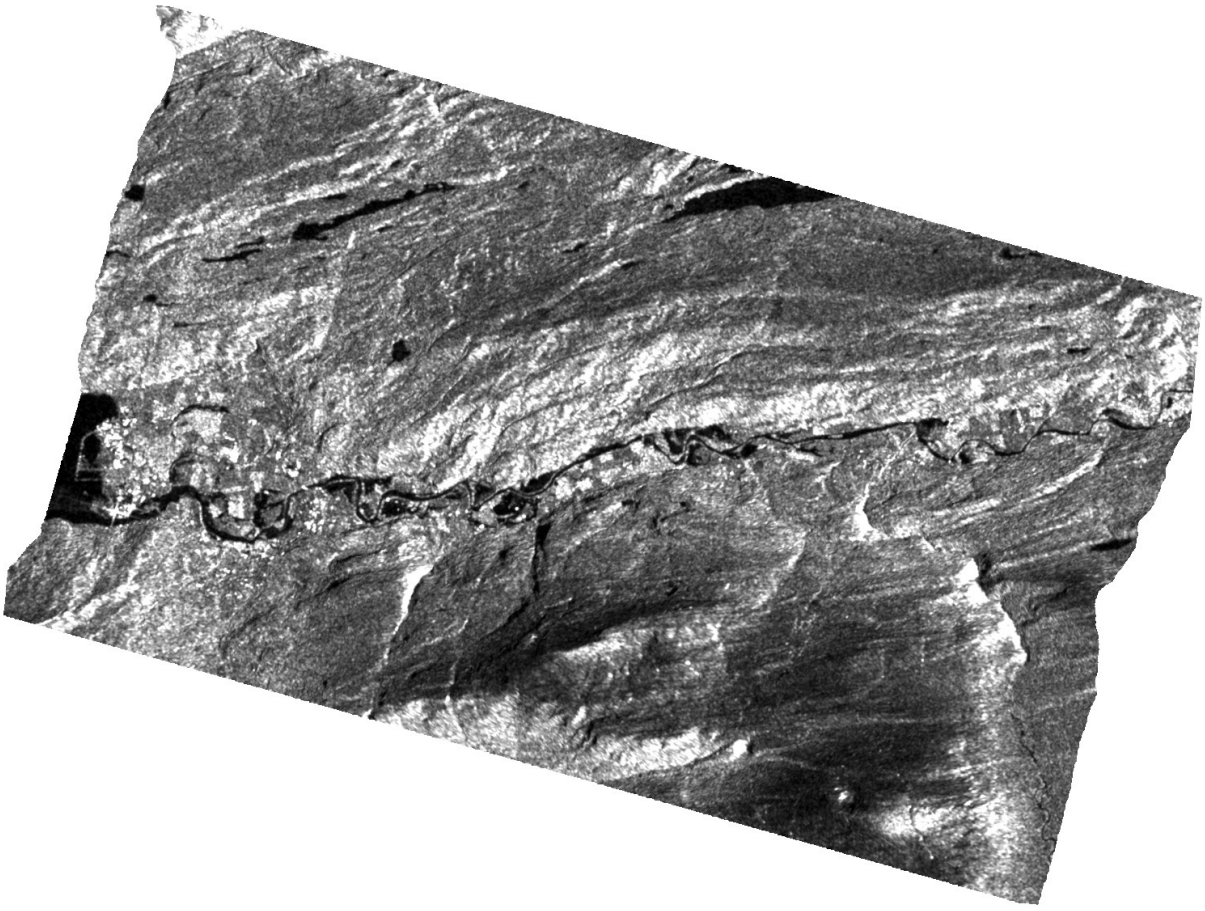

Figure 22: Sentinel-1 SAR image with VV polarization of flood event from November 24, 2021, after applying Range Doppler Terrain Correction.

Linear to logarithmic (dB) was then used as a conversion of backscatter coefficients to dB values using a logarithmic transformation. This will make it easier to see, understand, and manipulate the distribution of the pixel values, as most of the pixels have a very small backscatter value and a few have large values before the transformation. This created a new band that was saved by using the convert band function.

Thresholding is one of several approaches used to detect non-permanent water surfaces (Carreño Conde & De Mata Muñoz, 2019). Different algorithms have also been employed for the same task, including supervised classification (Chapman et al., 2015), automatic non-supervised classification (Borah et al., 2018), and RGB combination (Tavus et al., 2018), among others. Thresholding is a popular technique because it is relatively simple and efficient, making it a useful way to identify water surfaces in remote sensing images. Therefore, thresholding was used to specify water bodies inside the Sentinel-1 SAR images and create binary flood maps.

The objective of thresholding is to distinguish between the flooded areas and not flooded areas assuming a pixel threshold value that separates the wet pixels from the dry pixels in the SAR image. This is done by creating a histogram based on a statistical distribution of pixels and their backscatter intensity in dB. Bimodal distribution of the histogram is considered an ideal situation for determining a threshold value to identify flooded and non-flooded areas. In this situation, the histogram displays two distinct peaks separated by a valley. The first peak represents the pixels in flooded areas, which typically have low backscatter values due to the specular reflection on the water surface (Selmi, 2021). The

second peak represents the pixels in non-flooded areas, which generally have higher backscatter values. By selecting an appropriate threshold value at the valley between the two peaks, it is possible to effectively distinguish between flooded and non-flooded areas in the image. But in most cases, it is often rare to find an image where a large portion of the area is flooded, resulting in a clear bimodal distribution in the histogram. Instead, the histogram may show a single peak with a long tail representing the flooded area and another peak or plateau representing the non-flooded areas shown in Figure 23.

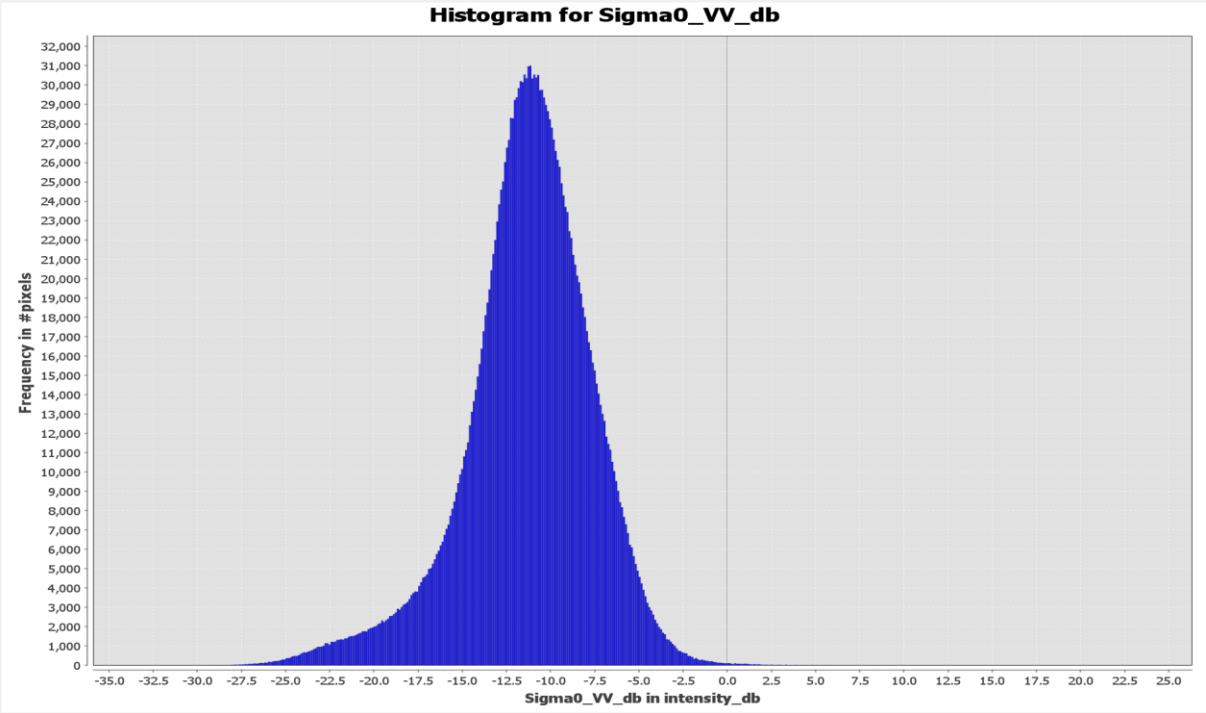

Figure 23: Histogram derived from Sentinel-1 SAR image with VV polarization, showing a single peak in the backscatter values of pixels during the flood on November 24, 2021.

A seen in the histogram of the pixel distribution, it does not show a clear definition in what pixel intensities that are flooded or not. To address this issue a method of focusing the attention to the flooded areas, creating polygons to select the region of interests. When selecting regions with approximately the same amount of flooded and non-flooded areas as shown in Figure 24, a more evenly distribution of flooded and non-flooded pixels is achieved.

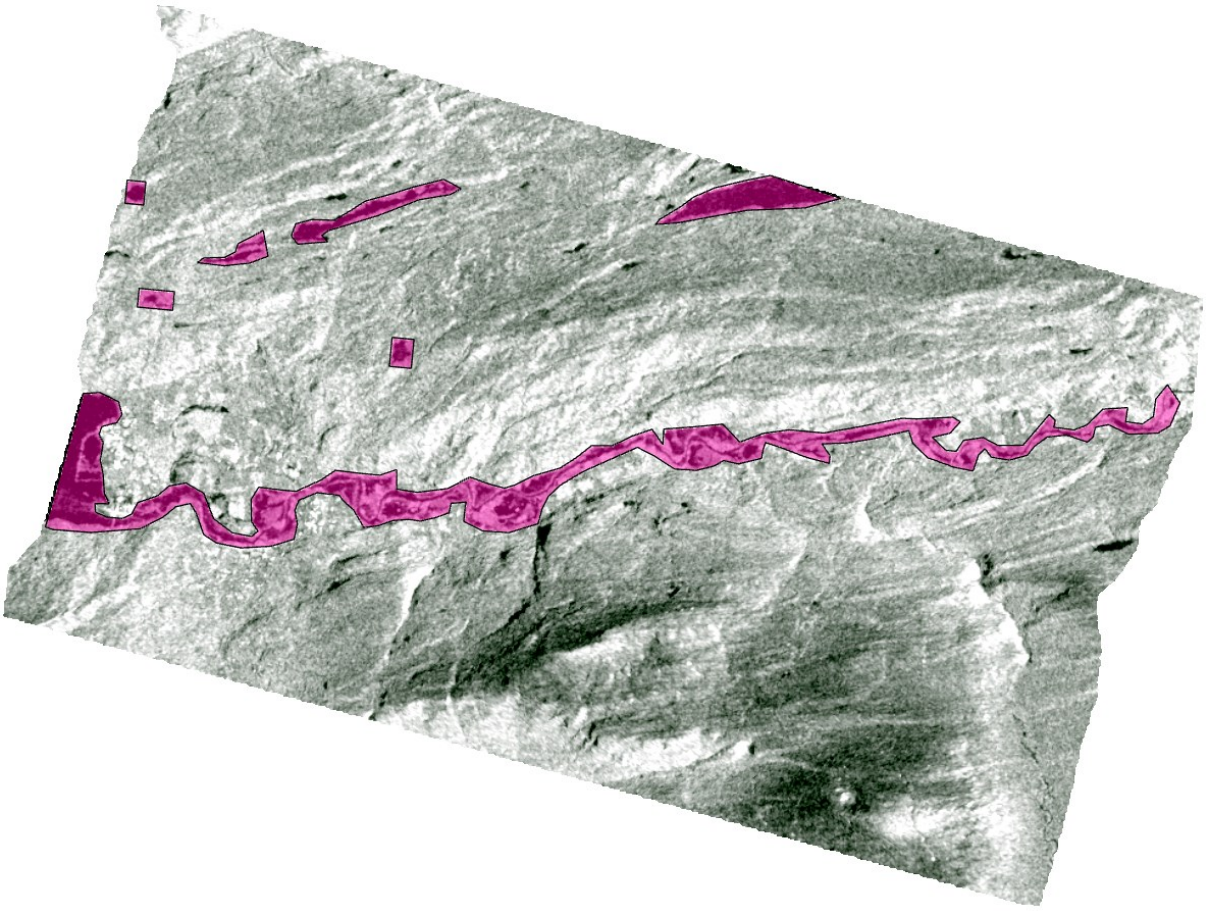

Figure 24: Polygons around flooded areas to better separate flooded pixels and non-flooded pixels.

This method generates vector data, which was then used to provide a bimodal distribution of pixel values, as shown in Figure 25. The valley of the bimodal distribution is around -16.0 dB meaning all values below this value will be identified as flooded pixels, while all the values above -16.0 dB will be identified as non-flooded pixels. However, it is important to note that using the threshold technique can result in misclassification and uncertainty in identifying flooded pixels. Some pixels with backscatter values within the range of flooded pixels may not actually be flooded, while some pixels with backscatter values outside this range may be flooded, leading to both false positives and false negatives.

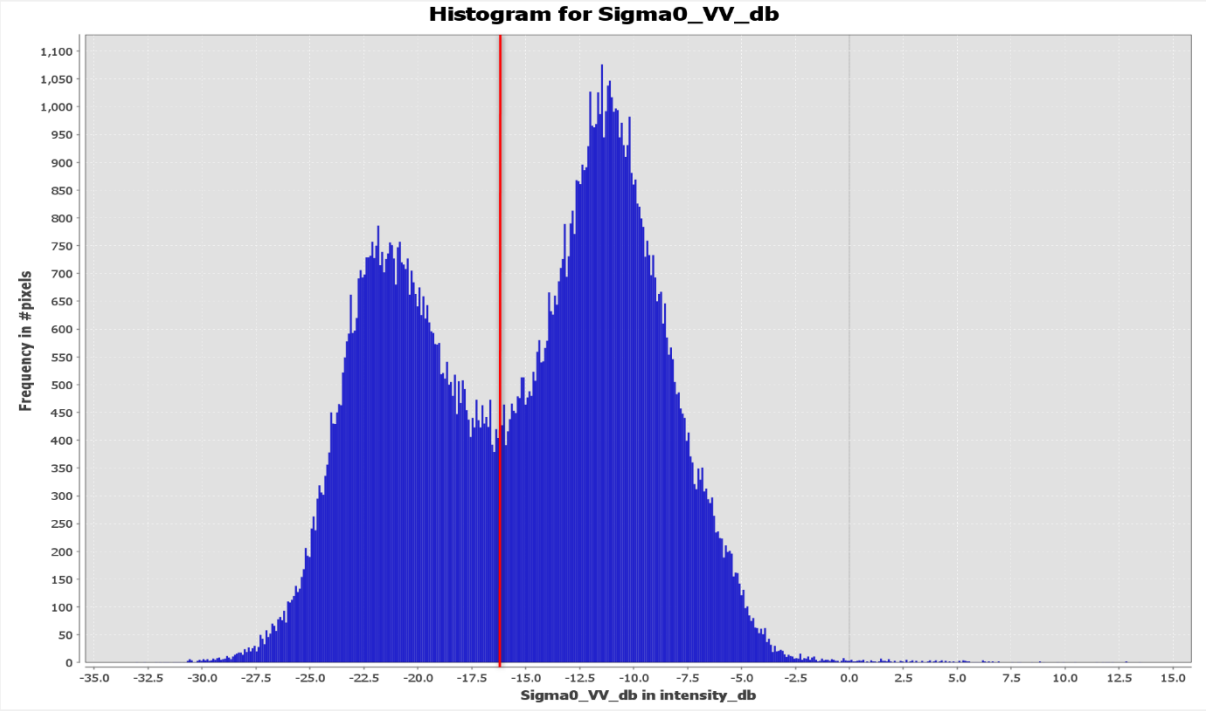

Figure 25: Histogram with bimodal distribution of pixels derived from vector data in Sentinel-1 SAR image with VV polarization during the flood on November 24, 2021.

To further refine the threshold value for distinguishing between flooded and non-flooded areas, polygons were used to capture the boundaries of several randomly flooded areas within the Sentinel-1 SAR image. This allowed for the creation of a histogram showing the distribution of pixel intensity only within the flooded areas. The Sentinel-1 SAR image with VV polarization during the flood on November 24, 2021, has pixel intensity distribution ranging from -27.5 dB to -12.5 dB in the flooded areas as shown in Figure 26.

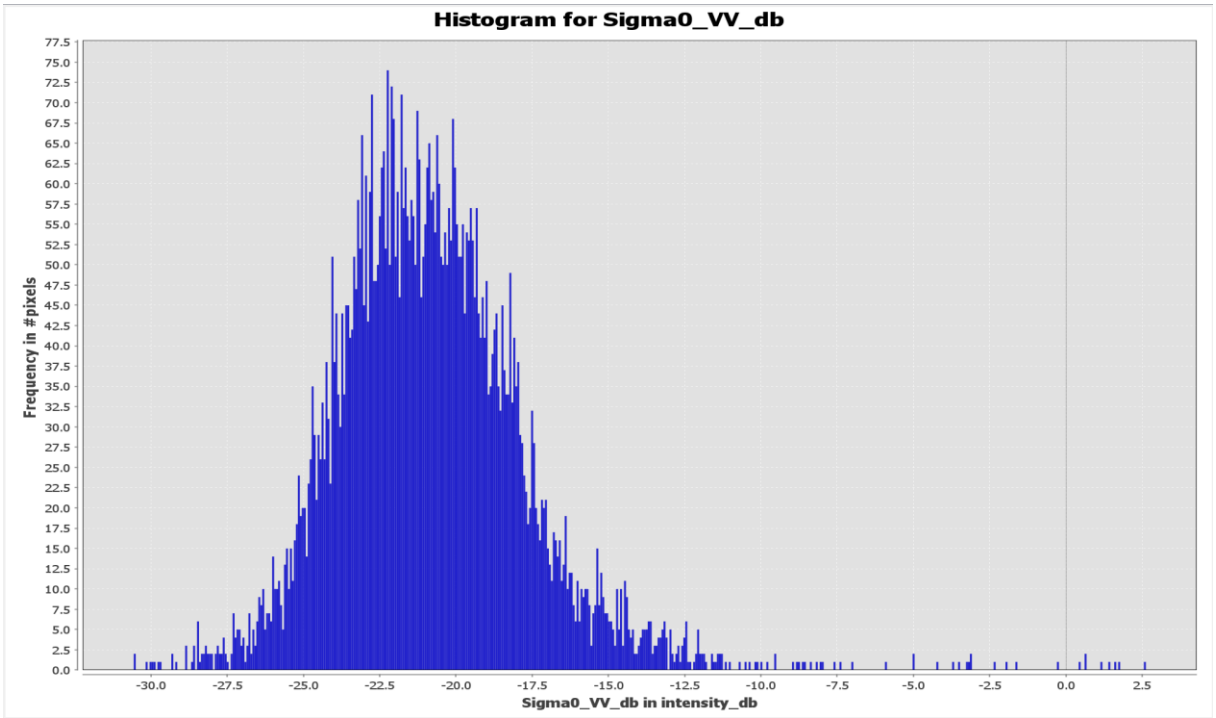

Figure 26: Histogram with distribution of pixels intensity from flooded areas, derived from Sentinel-1 SAR image with VV polarization during the flood on November 24, 2021.

This confirms that the pixel intensities from the bimodal is correct, and a threshold value can be applied to the band maths feature in S1TBX. Band maths can be used to perform mathematical operations on data acquired from Sentinel-1 SAR data images. It allows for the creation of new bands by combining and processing existing bands, resulting in a binary image for the flooded areas as shown in Figure 27. The expression used to capture the binary image was Sigma0_VV_db <- 15.0. However, the binary image shows more wet area than only the river and floodplains. This is because remote sensing imagery provides a comprehensive overview of all flood-related processes, including bank overtopping, excess rainfall, backwater effects, complex 2D and 3D flows in the floodplain (Di Baldassarre et al., 2009), and even lakes in mountainous regions. As a result, the binary images produced by applying the threshold on the band maths feature, capture not only the flooded areas in the river and floodplains, but also the additional wet areas that are a result of these various flood-related processes.

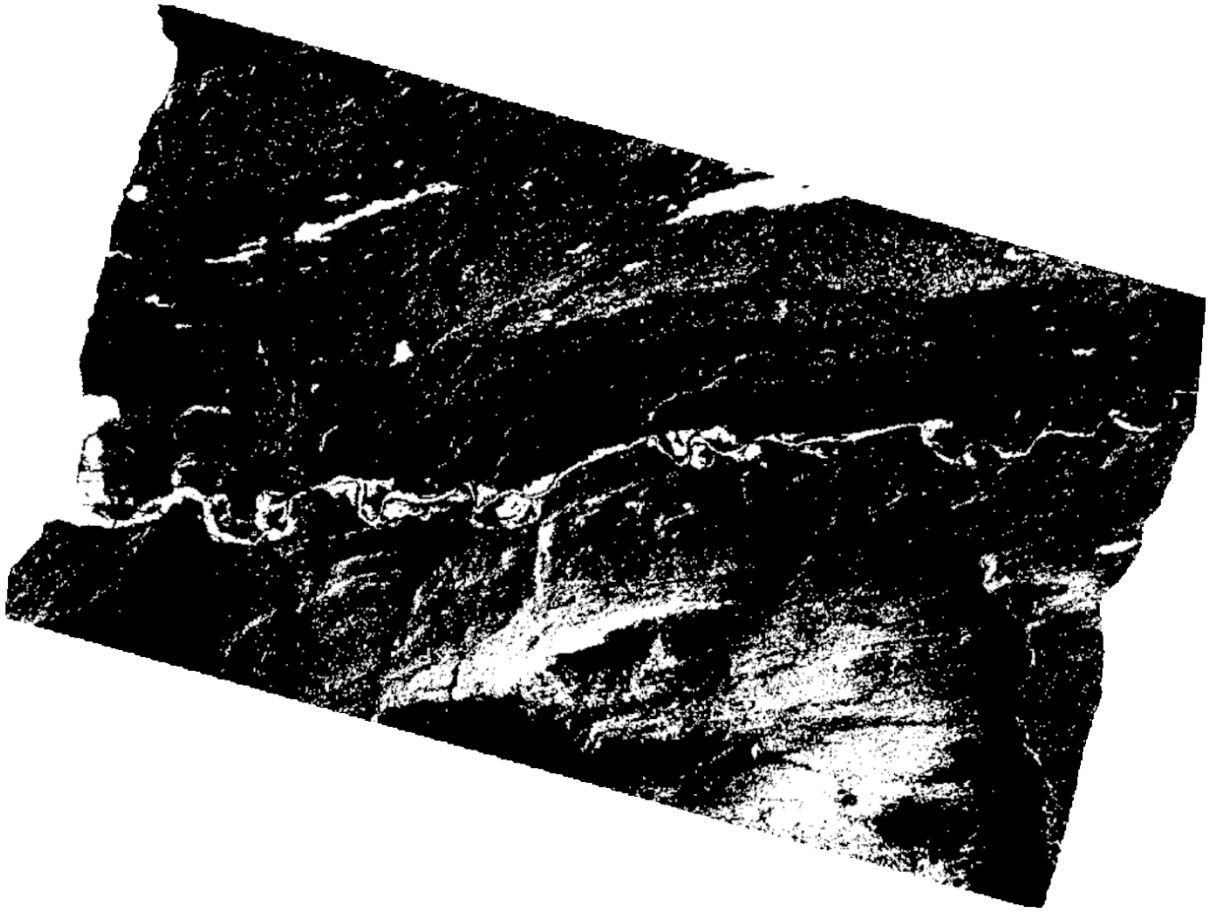

Figure 27: Binary flood map derived from Sentinel-1 SAR image with VV polarization during the flood on November 24, 2021.

The Sentinel-1 SAR images that were captured during the flooding events contains both VV and VH polarizations. (Pham-Duc et al., 2017) compared the VV and VH polarization when deriving surface water, where they found a 72 % spatial linear correlation with the reference water mask when using VH polarization. VV polarization showed a spatial linear correlation of 62 %. They also used both the polarizations for the classification, where they found a correlation of 76 %, and concluded that using both polarizations will increase the retrieval accuracy, since the two polarizations carry different information.

Therefore, the produced math bands feature was used to merge both VV and VH polarizations with the expression IF Sigma0_VV_db < -15.0 OR Sigma0_VH_db < -20.0 THEN 1 ELSE 0. The expression was changed for the other Sentinel-1 SAR images with their respective intensity threshold values as shown in Table 8.

Table 8: Pixel intensity values for Sentinel-1 SAR images for both VV and VH polarization.

Satellite & Acquisition time	Polarization	dB range for wet pixels	dB used in band maths
Sentinel-1A 2016-11-26 05:47	VV	-24.0 to -10.0	-14.0
	VH	-32.5 to -17.5	-18.0
Sentinel-1B 2020-01-21 05:54	VV	-20.0 to -10.0	-15.0
	VH	-40.0 to -22.5	-22.5
Sentinel-1A 2021-11-24 05:47	VV	-27.5 to -12.5	-12.5
	VH	-47.5 to -20.0	-20.0

The binary maps created for each flooding event, merged with VV and VH polarization was then imported as a raster to ArcGIS Pro, where they were converted to vector data and clipped according to the area of interest inside the study area. The flood delineated binary maps that were used for further analysis is shown in Figure 28.

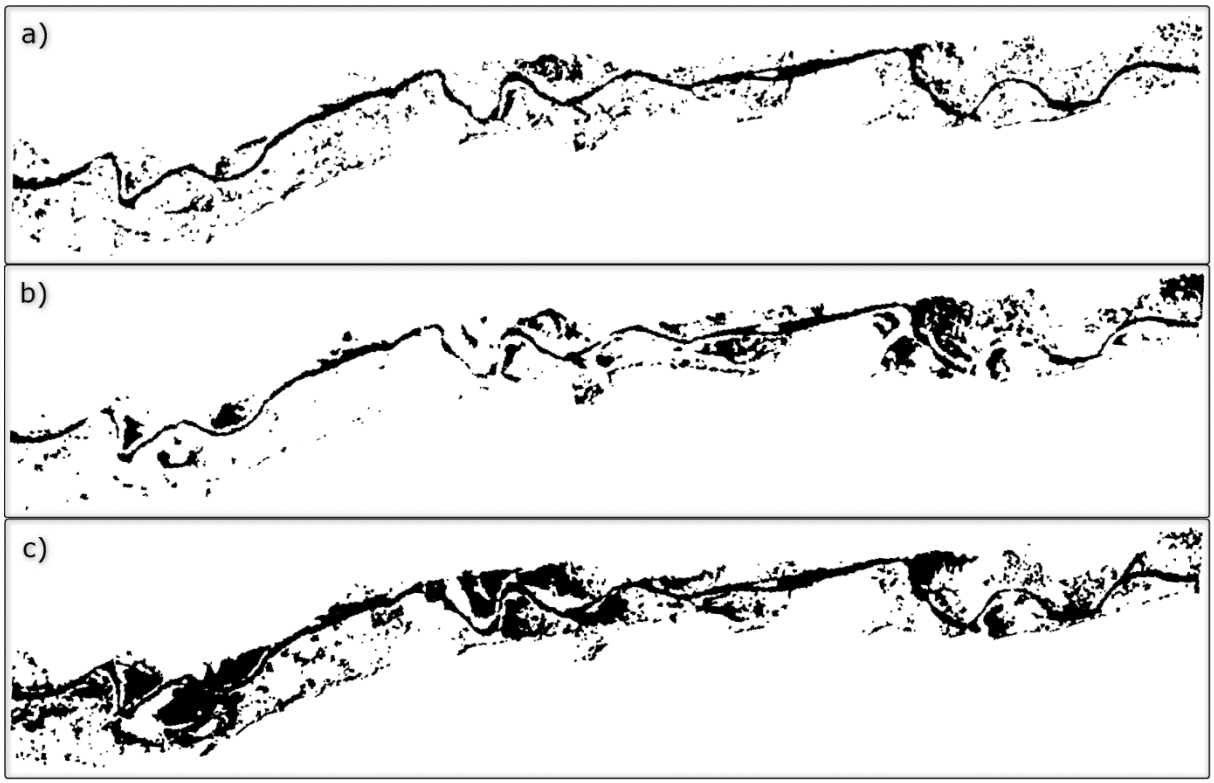

Figure 28: Flood delineated binary maps for det flood events: (a) November 26, 2016, (b) January 21, 2020, and (c) November 24, 2021.

3.7 HEC-RAS 2D hydraulic model

The HEC-RAS hydraulic model was set up in RAS Mapper in HEC-RAS. This section includes the methodology for the process of developing the HEC-RAS 2D unsteady hydraulic model to be ready for simulations. The flow data used in the boundary conditions is elaborated for in this section, but the placement and procedure for setting up the boundary conditions was previously covered in an earlier chapter.

In the HEC-RAS hydraulic model development, a projection file was utilized to accurately represent the spatial locations in the coordinate system. This projection file was obtained from spatialreference.org [https://spatialreference.org/] (accessed on February 22, 2023) and specifically chosen to transform the curved Earth surface onto a flat surface. The selected projected coordinate system was ETRS89/UTM zone 32N, which uses the metric system SI units. To ensure consistency, these SI units were also set as the project units within HEC-RAS. This process guarantees that the model accurately reflects the real-world geographic locations and allows for precise analysis of the hydraulic behaviour.

Furthermore, a terrain dataset was loaded to create a terrain model in RAS Mapper. The terrain data used in this case was the DEM generated in a study conducted by (Awadallah et al., 2022), which compromises both bathymetric and topographic LiDAR data with a resolution of 0.5 meters. The DEM is georeferenced in the ETRS1989 UTM zone 32N coordinate system, and by using the high-resolution and accurately georeferenced terrain model precise geometries could be created in the RAS Mapper.

Once the necessary foundations for creating the HEC-RAS hydraulic model was established, the initial geometry was developed. By default, HEC-RAS assigns a Manning's-n value of 0.06 to the entire 2D flow area if no other land cover layers are incorporated. This default value was used in the construction of a "Quick and Dirty" model, which involves setting up flow area polygons, defining cell sizes, incorporating breaklines, refinement regions, and establishing boundary conditions. This approach, combined with the diffusion wave, allows for quick computations and facilitates the testing of different settings to achieve a robust model. By utilizing the "Quick and Dirty" model, it was possible to extensively test the model with various configurations and settings before introducing the land cover layer and applying the shallow water equation in the calibration and validation phases. This testing phase allowed for the identification of any necessary adjustments and optimizations, ensuring more accurate and reliable solutions during subsequent simulations.

3.7.1 Mesh generation

The generation of the 2D computational mesh began by drawing a polygon boundary for the 2D flow area within the study area. The polygon representing the 2D flow area was carefully delineated at higher elevations to encompass areas that are unlikely to be inundated during flood events. This precaution was taken to ensure that the water does not reach those elevated regions. Additionally, the 2D mesh was extended to include the upstream and downstream boundary conditions, allowing for the incorporation of external boundary conditions into the model.

After establishing the 2D mesh with a grid resolution of 5 meters, a simulation was conducted using a 1000-year flood event. The simulation utilized a default Manning's n-value of 0.06 for all cells and a flow value of 1512 m^3/s (Leine, 2018). The purpose of this simulation was to generate a water extent that far exceeded what would typically be observed during calibration and validation processes. Once the simulation was completed, the 2D flow area was adjusted to be a few meters away from the water extent borders, as depicted in Figure 29. This adjustment aimed to potentially reduce computational times by reducing the number of computational cells in the mesh while ensuring that no water would reach the polygon boundary.

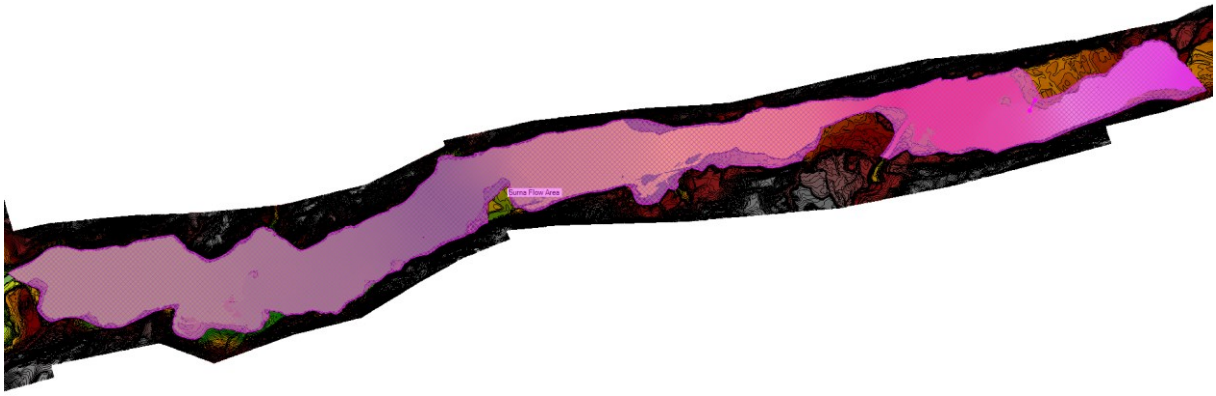

Figure 29: 2D flow area with a 1000-year flood water extent.

Once the polygon boundary of the 2D computational area was defined, the next step was to determine an appropriate mesh cell size. The cell size is crucial as it defines the resolution of the underlying terrain, with finer resolutions representing the terrain more accurately. However, using smaller cell sizes within the 2D flow area results in a larger number of cells and longer simulation times.

In order to achieve a balance between model accuracy and simulation times, it was important to carefully select the cell size within the 2D flow area. While using the same cell size as the terrain model would provide the most accurate results, it was not practical due to the significant increase in simulation times, especially considering the large number of simulations runs required during the evaluation of Manning's n-values in the calibration and validation processes.

In HEC-RAS, a detailed volume/area relationship is employed to accurately represent the underlying terrain. This is achieved by representing each cell face as a detailed cross-section of the terrain, which is then processed to establish relationships between detailed elevation volume/area, wetted perimeter, and roughness (G. W. Brunner, 2023). As a result, HEC-RAS allows for the use of larger cell sizes while still effectively capturing the characteristics of the terrain. This approach enables the selection of larger cell sizes without significantly compromising the accuracy of the hydraulic model.

However, it is important to note that the water surface elevation is computed at the center of each cell. Therefore, if the cell size is too large, the averaged water surface will be calculated over a longer distance. In cases where the water surface slope and velocity change rapidly, such as in small, steep rivers, choosing a smaller cell size is necessary to accurately capture these changes. On the other hand, in large, flat floodplains where water surface and velocity changes are more gradual, a larger cell size can be chosen without significant loss of accuracy.

Taking these factors into consideration, a cell size of 10 meters was selected for the development of the hydraulic model in this study. This choice balanced the need for accuracy with reasonable computational times, with simulations typically taking around 1-2 hours to complete. While no sensitivity analysis was conducted to evaluate the accuracy of the model with different cell sizes, it was assumed that this cell size would yield satisfactory results given the functionality of detailed volume/area relationship within HEC-RAS.

In summary, selecting an appropriate mesh cell size involves a trade-off between accuracy and computational efficiency. By choosing a cell size that strikes a balance between these factors, the model can provide accurate answers while keeping the simulation times within acceptable limits.

3.7.2 Breaklines and refinements regions

Once the 2D computational mesh with 10 m cells was created for the 2D flow area, additional enhancements were made through the use of breaklines and refinement regions. Breaklines and refinement regions was introduced to better represent the high grounds and other barriers to the flow with aligning the computational cell faces along these features.

Through an iterative process, breaklines were strategically placed at locations where water was leaking through structures that were higher than the water surface elevations. These breaklines served to rectify any inaccuracies in the model by effectively aligning the cell faces and preventing water from flowing through undesired paths. Additionally, breaklines were also introduced at high ground features such as levees, roads, and other elements that could impact the accuracy of the model. To avoid significant increases in simulation times, the breaklines were introduced with the same resolution as the 2D computational mesh, ensuring a balance between model accuracy and computational efficiency.

To accurately represent the main channel aligned with the flow, a refinement region with integrated breaklines was introduced. This approach improves the accuracy of the hydraulic model by reducing numerical diffusion and enhancing computational accuracy. The refinement region was specifically placed along the channel banks in the main channel, which also can lead to improved modelling results (Sanchez, 2021). By aligning the cell faces with the channel banks, the issue of leakage through higher channel banks than the actual flow in the main channel is effectively addressed. This alignment ensures that the cells accurately represent the channel geometry and flow characteristics. Additionally, to further refine the alignment of cells within the refinement region, breaklines were drawn along the centre of the region, following the path of the flow. The number of near repeats for the breaklines was determined based on the width of the river at the specific location of the breakline. This approach ensures that the cells aligned precisely with the refinement region, as depicted in Figure 30.

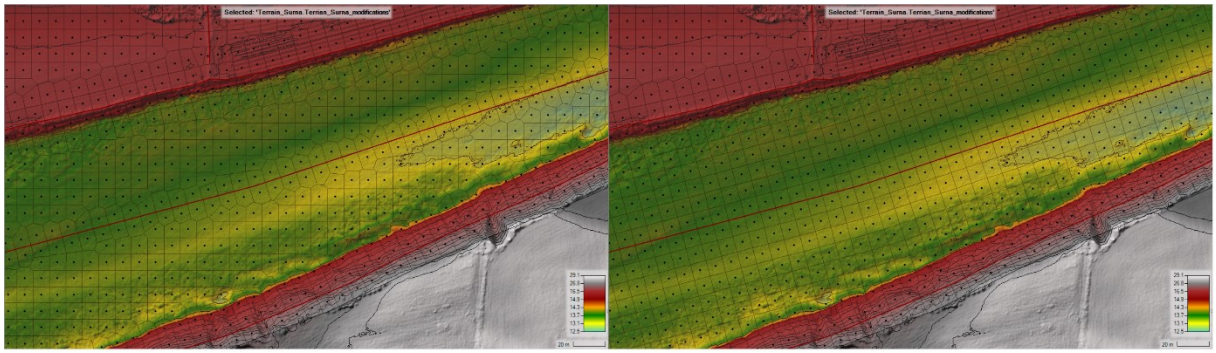

Figure 30: Main channel before and after enforcing a refinement region and breaklines.

3.7.3 Hydraulic structures

Hydraulic structures, such as bridge decks, piers, culverts, weirs, and gates in 2D hydraulic modelling can either serve as the focus of the analysis or as features that can significantly impact the hydraulic behaviour of the system (Robinson et al., 2019).

There are two bridges in the study area that crosses the Surna River, but according to (Bævre & Øydvin, 2007), they have sufficient clearance in relation to flood and ice accumulation. Hence, they will not be included as hydraulic structures in this analysis.

The bridge in the Vindøla River is not included as a hydraulic structure since the external boundary condition is placed downstream the bridge, therefore the flow of water will not be impacted by the presence of this structure.

Regarding culverts and bridges in the smaller tributaries within the study area, they can often be represented as a terrain elevation in the DEM generated from LiDAR data as shown in Figure 31.

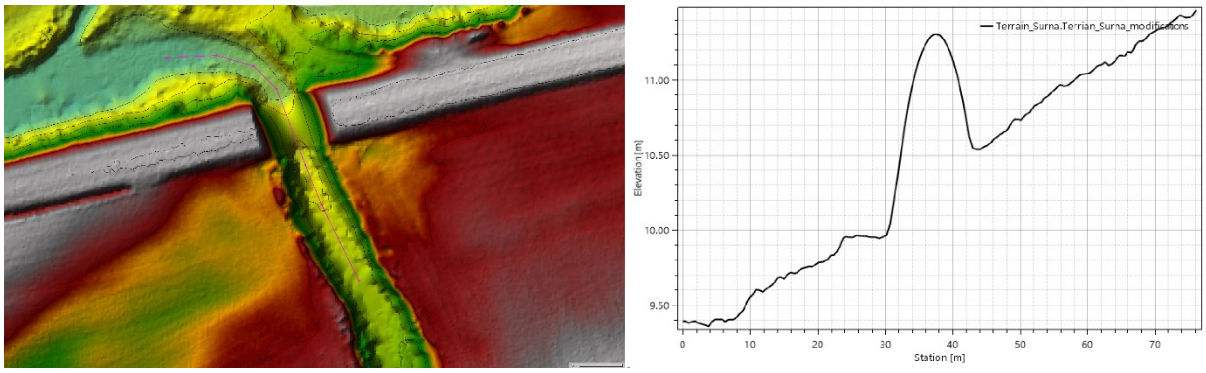

Figure 31: Terrain elevation in DEM generated from LiDAR data.

Since internal boundary conditions is being used for the tributaries at the confluence to the Surna River, the potential backwater effects in flooding events caused by limiting capacity in the culverts and low bridge decks in the tributaries is not taken into consideration in the hydraulic model. However, to achieve a more accurate simulation, the terrain has been flattened out as terrain modifications in RAS Mapper in HEC-RAS as shown in Figure 32. This flattening of elevations leads to a more realistic rise of water in the tributaries as the water surface elevation in the Surna River increases.

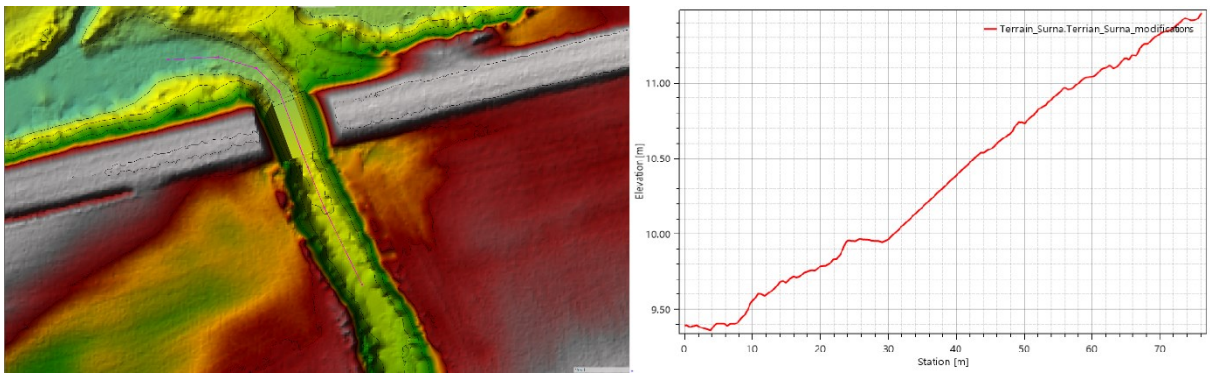

Figure 32: Terrain in tributary after terrain flattening done in RAS Mapper.

3.7.4 Flow data

Flow data used for the upstream and lateral boundary conditions during the various flooding events simulated was obtained from Sildre. Sildre is a publicly accessible web service provided by the NVE that offers a comprehensive database of historical and near real-time hydrological data. The platform features a map displaying all registered measuring stations in Norway. The prioritized measurements available for display and download as time series, in both table format and graphs, include water-stage, discharge, and water temperature.

The flow for the upstream boundary condition in the model was derived directly from 112.27 Skjermo measuring station for the different events. However, for the flood event that occurred on August 13, 2003, the observed flow from the acquisition of the water surface elevations was utilized (Bævre & Øydvin, 2007). On the other hand, the lateral boundary conditions, represented by the Vindøla River and the smaller tributaries, the developed regression formulas, and scaling from Rinna, respectively, was used as flow input in the model.

i. Flood August 14, 2003

Flow data for this flooding event that reached a peak discharge of 602 m^3/s were based on what the discharge in 112.27 Skjermo was when the observed water surface elevations was acquired, as previously mentioned. The flow data in every boundary condition is used as a flat hydrograph since there is no timesteps for the collected water surfaces. The duration of the flow data that is 12 hours, and the flows for all the different boundary conditions is shown in Figure 33.

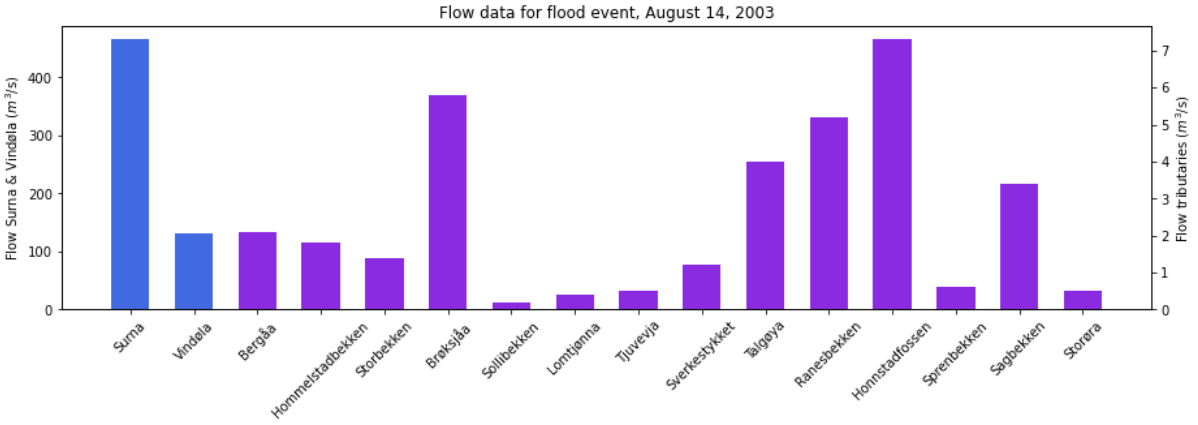

Figure 33: Flow data for flood event, August 14, 2003 (Blue bars is the Surna River and Vindøla River. Pink bars is the smaller tributaries.)

ii. Flood November 26, 2016

Flow data for the flood event that reached a peak discharge at 451 m^3/s, covers a duration of 24 hours, starting on November 25, 2016, at 10:00 and ending on November 26, 2016, at 10:00 as shown in Figure 34.

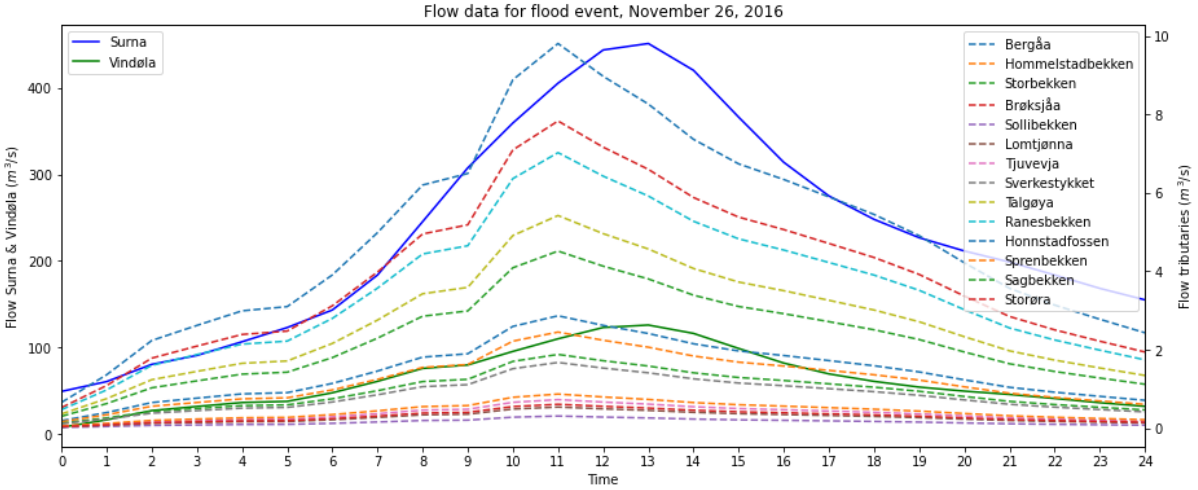

Figure 34: Flow data for flood event, November 26, 2016.

iii. Flood January 21, 2020

Flow data for the flood event that reached a peak discharge at 356 m^3/s, covers a duration of 24 hours, starting on January 20, 2020, at 12:00 and ending on January 20, 2020, at 12:00 as shown in Figure 35.

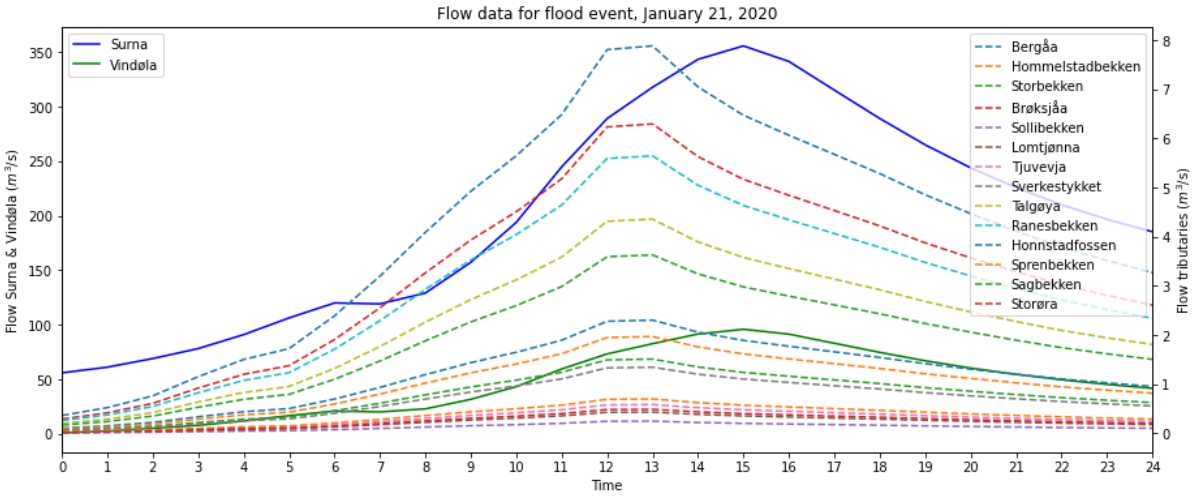

Figure 35: Flow data for flood event, January 21, 2020.

iv. Flood November 24, 2021

The flow data for the flood event that reached a peak at 583 m^3/h, covers a duration of 33 hours, starting on November 23, 2021, at 08:00 and ending on November 24, 2021, at 17:00 as shown in Figure 36.

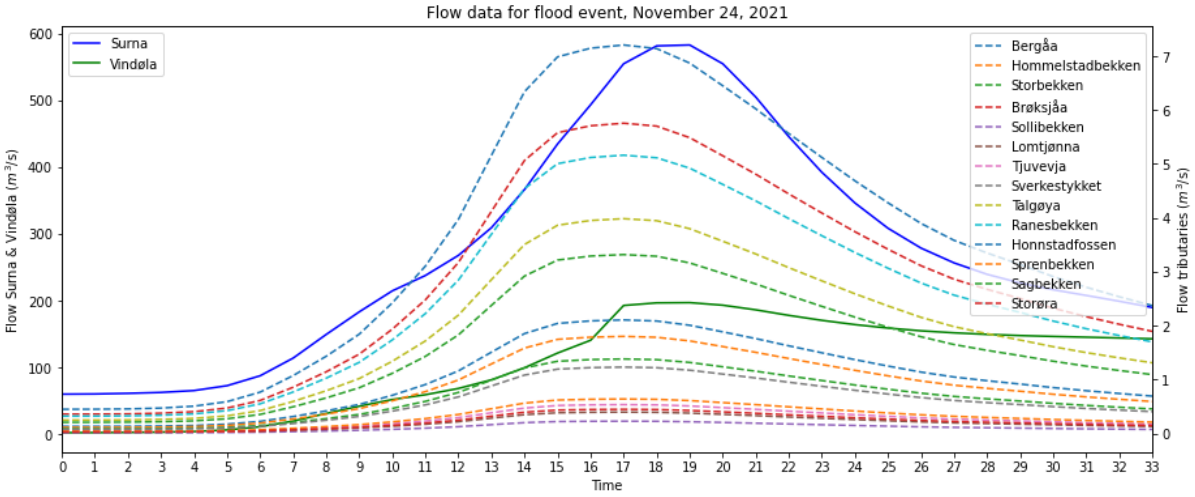

Figure 36: Flow data for flood event, November 24, 2021.

v. Flood January 13, 2022

The flow data for the flood event that happened during Storm Gyda, which reached its peak at 692 m^3/s, covers a duration of 32 hours, starting on January 12, 2022, at 16:00 and ending on January 14, 2022, at 00:00 shown in Figure 37.

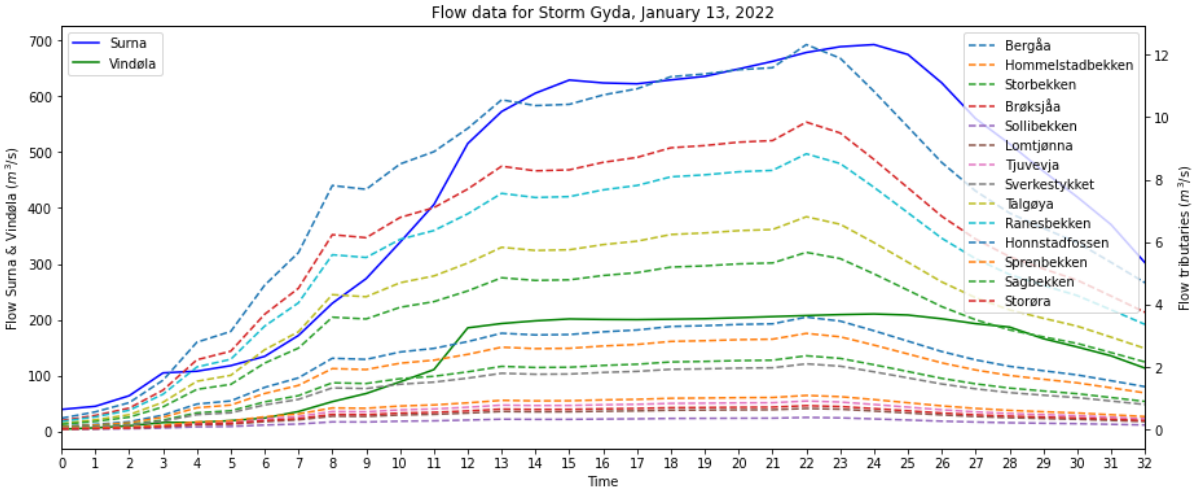

Figure 37: Flow data from Storm Gyda, January 13, 2022.

3.8 Simulations

Furthermore, apart from creating the 2D computational mesh with breaklines, refinement regions, hydraulic structures, land cover layers, and defining flow boundary conditions, there are additional parameters in the 2D hydraulic model that need to be adjusted to control numerical operations during simulations. These parameters play a critical role in ensuring accurate and reliable results. The upcoming sections will cover the parameters that were taken into consideration and adjusted prior to conducting the simulations.

3.8.1 Diffusion Wave vs Shallow Water Equation

HEC-RAS offers the option to use both the diffusion wave equations and the shallow water equations for 2D unsteady flow routing. When using the shallow water equations, there are two solver options available: SWE-ELM (Shallow Water Equation, Eulerian-Lagrangian Method) and SWE-EM (Shallow Water Equation, Eulerian Method). The SWE-EM is a more conservative form of the momentum equation and utilizes an explicit solution scheme. It is particularly useful when analysing water surface and velocity changes around hydraulic structures, piers/abutments, and areas with tight contractions or expansions. However, for most scenarios that require a comprehensive solution scheme based on the full momentum equation, the original SWE-ELM solver is more than sufficient. It provides accurate results and is suitable for a wide range of problems (G. W. Brunner, 2023).

On this background, simulations using both the diffusion wave equation and the original shallow water equation in the 2D hydraulic model was run and the results were compared. Figure 38 displays the outcomes obtained from the simulations of the August 14, 2003, flood event. Upon visual analysis of the results, it was observed that the diffusion wave equation tends to underestimate the water surface elevations in certain areas.

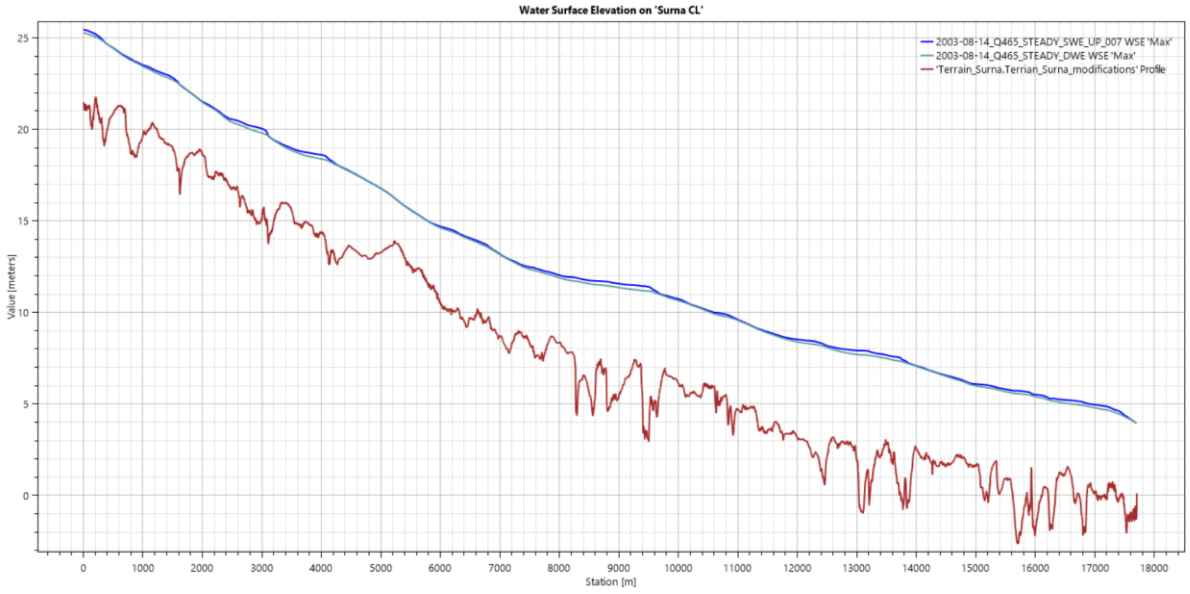

Figure 38: Comparison between diffusion wave and shallow water equation simulating the August 14, 2003, flood event.

Considering this discrepancy, the shallow water equations (SWE-ELM) was chosen as the preferred equation set. It is recommended to assume that the answers using the full-momentum equations are more accurate when there are significant differences in the results (G. W. Brunner, 2023).

3.8.2 Computational time step

Timing parameters are crucial when utilizing the diffusion wave or shallow water equation to perform an unsteady flow analysis in HEC-RAS. In particular, two important parameters need to be considered: the simulation time window and the computation settings.

The simulation time window is determined by the available flow data and represents the duration over which the model will simulate the hydraulic behaviour. This parameter is straightforward and depends on the specific flow data used for the analysis.

Computation settings, on the other hand, encompass the determination of suitable computational time steps that align with the computational mesh, cell sizes, and the characteristics of the modelled event. The computational time step governs the frequency at which the model updates and calculates hydraulic variables during the simulation. It is important to select a time step that strikes a balance between accuracy and computational efficiency. A smaller time step provides more precise results but increases computational time, while a larger time step reduces computational time but may sacrifice accuracy (G. W. Brunner, 2016).

The computational time step was estimated using the Courant Condition with one of the following equations:

$$C = \frac{V\Delta T}{\Delta X} \qquad (12)$$

$$\Delta T \leq \frac{C\Delta X}{V}$$

(13)

where *C* is the Courant number, *V* is the flood wave velocity, *ΔT* is the computational time step, and *ΔX* is the average cell size.

HEC-RAS is capable of utilizing Courant numbers as high as 3.0 for shallow water equations and up to 5.0 for diffusion wave equations while maintaining stability and accuracy. However, the specific choice of the Courant number depends on the characteristics of the event being modeled. If the flood wave exhibits gradual changes over time and space, larger time steps can be employed, allowing for a higher Courant number. Conversely, if the flood wave changes rapidly in relation to time and space, a smaller time step must be used to satisfy the Courant condition. Specifically, a Courant number close to 1.0 is generally recommended to ensure accurate modeling outcomes in these types of events when using the shallow water equations (G. W. Brunner, 2023).

Since the release of version 6.0, HEC-RAS has incorporated the capability to employ a variable time step in the flow engine for 2D unsteady flow models. Previously, a fixed computation time step was utilized throughout the simulation, which were calculated based on the Courant Condition equations. However, with this enhancement, a minimum and maximum Courant number can be specified, enabling the utilization of lower processing times and improved accuracy in modeling outcomes, taking into account the behavior of the flood wave concerning time and space. For more detailed information on the variable time step capabilities of HEC-RAS, readers are encouraged to consult the HEC-RAS 2D User's Manual (G. W. Brunner, 2023).

The following computation settings was utilized for the simulations:

- Computation interval: 5 Second
- Maximum Courant: 2.0
- Minimum Courant: 0.95
- Number of steps below minimum for doubling: 4
- Maximum number of doubling base time step: 4
- Maximum number of halving base time step: 4

3.8.3 Initial conditions

Initial conditions in hydraulic modelling can be either a “hot start” or a “cold start”. In a hot start, the model is initialized with water, while in a cold start, the model begins with no water. The choice of initial conditions depends on the specific requirements and objectives of the simulation.

In this study, two different methods were employed in HEC-RAS to handle the initial conditions of the model: restart files and initial conditions ramp up time. These methods are used to warm up the model before the actual computations begin and establish the initial water conditions (“hot start”).

The restart file method was utilized when a flat hydrograph was employed, specifically in the case of the August 14, 2003, flood event. It involves running a simulation with predefined parameters and creating a restart file that captures the conditions of the model at the end of the simulations. The restart file is then loaded, providing the initial conditions for the actual computations, allowing for faster convergence and shorter

simulation times. However, it is important to note that when using a restart file, no modifications to the geometry in the 2D flow area can be made. If any changes to the geometry are required, a new restart file must be generated to incorporate those adjustments.

For the other flood events that utilized a full hydrograph with different flow values for each time step, the option *initial conditions ramp up time* was employed. This method fills the model with water over a specified duration of time using the first flow value in the hydrograph. As a result, when starting the simulations, the time is initialized with a negative value representing the specified ramp-up time and counts down to zero. Once the time reaches zero, the simulations proceed by utilizing the complete hydrograph for representation of the flood event.

Additionally, the *initial conditions ramp up fraction* parameter can be set within the range of 0 to 1.0. This parameter determines the proportion of *the initial conditions ramp up time* that will be allocated for gradually increasing the flow to the first value of the hydrograph. For instance, if an *initial conditions ramp up time* of 10 hours is specified and an *initial conditions ramp up fraction* of 0.1 is used, the first hour of the ramp up time will be utilized to incrementally raise the flow to the first value of the hydrograph within the *initial conditions ramp up time*.

Through a trial-and-error approach, it was determined that *an initial conditions ramp up time* of 8 hours, coupled with an *initial conditions ramp up fraction* of 0.1, was sufficient to fill the model with water and provide a "hot start" before the actual computations commenced.

3.9 Calibration

Calibrating 2D hydraulic models against observed water surface elevations or flood extents is an extensive task that requires using different Manning's n-values to represent the roughness of the different land cover types. Therefore, the calibration process started with applying the land cover map AR5 as a base, using different sets of Manning's n-values for the main channel (0.02 – 0.1) and floodplains (0.02 – 0.1), while keeping the rest of the Manning's n-values constant. Complete soil cultivated, surface cultivated soil, and infield grazing are individual land cover types, but were treated as a combined roughness group for the floodplains and assigned the same Manning's n-value. The constant Manning's n-value for the other land cover types was:

- Open land (0.040)
- Urban area (0.100)
- Forest (0.150)
- Road (0.016)
- Swamp (0.050)

Then, simulations were run using individual land cover layers in HEC-RAS for all the different Manning's n-value combinations. The Manning's n-values for the floodplains were increased by 0.01 through all the different main channel values, while the rest of the Manning's n-values where kept constant to limit the number of simulations. Each land cover layer was linked to the same number of identical geometries and set up as individual plans in unsteady flow analysis, to utilize the run multiple plans function in HEC-RAS. The first process of calibrating was to achieve the best parameter set for Manning's n-values without using calibration regions to individualize roughness values in

different parts of the main channel and floodplains or using Manning's n-values that were not inside the defined range to achieve a better goodness of fit. This calibration approach was done on both the flood from August 14, 2003, where observed water surface elevations were acquired during the flood and the flood from November 24, 2021, where Sentinel-1 SAR imagery was captured.

After completing the initial calibration, a fine-tune calibration was conducted for the flood event that took place on August 14, 2003. This calibration aimed to further improve the goodness of fit. The best fit Manning's n-value for the main channel was adjusted within a range of +- 0.005, while the n-values for the floodplains were increased by 0.01 progressing from the low to high range, for each increment in Manning's n-value in the main channel.

Studies have shown that the model sensitivity to Manning's n-value for floodplains have found to be relatively small (Horritt, 2006). Therefore, a regionalized calibration was conducted for the Manning's n-values in the main channel for the August 14, 2003, flood event, while keeping the Manning's n-values for the floodplains and other land cover types constant during the calibration process. The Manning's n-values for the other land cover types were set as described earlier in this chapter, while the Manning's n-value for floodplains was set to 0.05. Then calibration regions were made in HEC-RAS on a reach-to-reach basis, based on the observed water surface elevation profile lines. A calibration region in HEC-RAS is used to redefine all the Manning's n-values within that specific region for each land cover type. The start and ending of the calibration regions were placed varying from a couple of hundred meters to a few kilometres upstream and downstream the profile lines, depending on how much of an adjustment to the simulated water surface elevation had to be made. This was a trial-and-error calibration approach, were the placement of the regions and Manning's n-value for the main channel was adjusted until the best fit between the simulated and observed water surface elevations was achieved.

Although the model sensitivity is relatively small for floodplain Manning's n-values, a regionalized calibration was performed specifically for the flood event that occurred during Storm Gyda on January 13, 2022. To establish a baseline, the parameter set with the best measure of fit from the previous calibration, conducted for the flood event on November 24, 2021, was utilized. Subsequently, calibration regions were defined within the main channel and floodplains to adjust the Manning's n-values on a local and reach-to-reach basis as necessary. This calibration process followed a trial-and-error approach, involving modifications to the placement of regions for both the main channel and floodplains, as well as the corresponding Manning's n-values. The ultimate objective was to achieve the best measure of fit between the simulated flood extent and the observed flood extent derived from the EMSR vector product merged with the SR16 forest resource map.

3.10 Validation

Validation is a crucial and integral step in the modelling process as it enables the assessment of the accuracy and reliability of the calibrated flood inundation models. The primary objective of the validation process was to verify the capabilities of the calibrated models in accurately simulating various flood events by comparing them with real-world observations.

In this study, the validation analysis included a comparison between the model predictions and multiple sources of data. These sources included observed water surface elevations, flood delineation maps generated from SAR imagery acquired from the Sentinel-1 and COSMO-SkyMed satellites, and the SR16 forest resource map merged with the mentioned flood delineation maps.

Figure 39 visually presents the flood delineation maps represented in black, along with the SR16 forest resource map displayed in pink. It is important to note that the SR16 forest resource map was clipped separately within each flood simulation in this study, to represent the flooded areas that were not delineated from the SAR images. As a result, the displayed clipped SR16 areas in the figure is not representative to all the validation analyses conducted. It is provided for illustrative purposes only to demonstrate the flood delineation maps with the SR16 map.

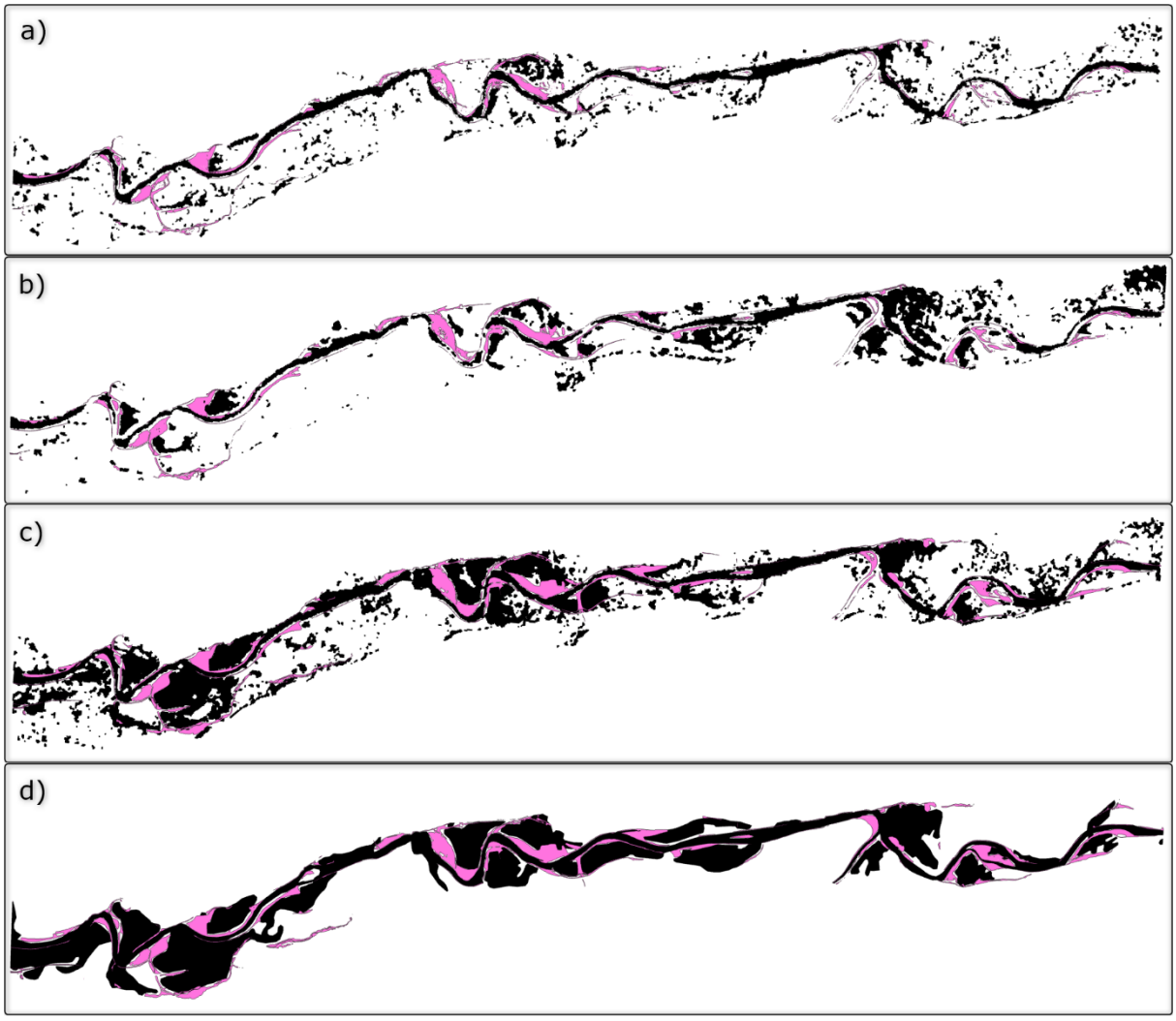

Figure 39: Flood delineated maps of SAR images (black) with the SR16 forest resource map (pink). (a) Flood event, November 26, 2016. (b) Flood event, November 24, 2021. (c) Flood event, November 24, 2021. (d) Storm Gyda flood event, January 13, 2022.

These flood delineated maps from the SAR images offer valuable insight into the observed flood extent, allowing for a comprehensive evaluation of the performance of the model. The utilization of SAR images enables direct comparison of the simulated flood extent with the actual flood extent observed from space, thus enabling a visual confirmation of the accuracy of the model. By conducting thorough validation against

multiple flooding events and utilizing different sources of validation data, this study ensures a comprehensive assessment of the performance of the model and strengthens the overall credibility of the flood inundation models.

The different calibration events validated is listed below, with the elaboration of what validation data is used in each event.

i. Flood August 14, 2003

The flooding event that occurred on August 14, 2003, was initially calibrated against observed water surface elevations. Subsequently, the calibrated model was validated using all available Sentinel-1 SAR images (a), (b) and (c), and the EMSR product derived from the COSMO-SkyMed program (d) (see Figure 39). The validation was conducted using the best parameter set obtained from the fine-tuned calibration process, as well as Manning's n-values from the calibration regions obtained through the regionalized calibration approach.

vi. Flood November 24, 2021

The flood event that took place on November 24, 2021, underwent a calibration process to determine the optimal Manning's n-values for the main channel and floodplains. This calibration step aimed to achieve the best measure of fit for the model. Subsequently, the calibrated model, utilizing the best parameter set, went through validation using two Sentinel-1 SAR images (a) and (b), as well as the EMSR product derived from the COSMO-SkyMed program (d) (see Figure 39). Additionally, the model was validated using observed water surface elevations from the flooding event that occurred on August 14, 2003.

vii. Flood January 13, 2022

The flood event that happened during Storm Gyda was regionalized calibrated trough changing Manning's n-values in channel and floodplains locally with calibration regions, to provide the optimal measure of fit. The calibrated model with the best measure of fit were validated using the three Sentinel-1 SAR images (a), (b) and (c) (see Figure 39). Furthermore, the model underwent validation using observed water surface elevations from the flooding event that took place on August 14, 2003.

3.11 Sensitivity analysis

Sensitivity testing was conducted for the upstream and downstream boundary conditions prior to the calibration and validation processes. This step was essential in defining the study area and avoiding the influence of different friction and energy slopes calculated for the boundary conditions. Additionally, a preliminary sensitivity test was performed for the lateral boundary conditions to compare the effects of using external and internal boundary conditions.

However, these sensitivity tests were conducted during the model setup phase aimed to establish a reliable and robust model for various types of flood events. Trough the analysis of the sensitivity of the model to these boundary conditions, potential uncertainties associated with them could be minimized. This to give confidence in the model to accurately simulate hydraulic behaviour and provide trustworthy results for a range of scenarios and conditions.

It is important to note that sensitivity testing on the mesh resolution in the hydraulic model could provide valuable insights, as this parameter can significantly impact the modelling results (Shustikova et al., 2019). This can be achieved by varying the grid size from coarse to refined, finding the optimal balance between mesh detail and computational efficiency. However, in this study, the grid cells were already set at a resolution of 10 m, matching the pixel resolution of SAR imagery from the Sentinel-1 satellite program. Therefore, further testing on this parameter was not conducted.

The Manning's n-values hold significant importance, if not the utmost importance, in the calibration of 2D hydraulic models (Pappenberger et al., 2005). Altering the Manning's n-values can significantly impact the modelling outcomes, emphasizing the need to investigate the parameters that have the most pronounced influence on the modelling results when adjusted. Consequently, a comprehensive global sensitivity analysis was carried out on the three dominant land cover types within the study area: floodplains, main channel, and forest areas, accounting for 62%, 12.2%, and 15.4% of the total area, respectively. To manage the extensive range of Manning's n-value combinations and ensure a manageable number of simulations, these parameters were assumed to exert the greatest influence on the modelling results, thereby being the primary focus of the sensitivity analysis.

Through the systematic variation of Manning's n-values within established literature-based ranges, the sensitivity analysis sought to evaluate the holistic performance of the model in replicating observed water surface elevations and flood extent. This thorough assessment will offer valuable insights into the parameters that are most susceptible to changes in Manning's n-values, thereby emphasizing their critical role in the calibration process.

3.12 Model analysis and results comparison

The effect of different Manning’s n-values on the performance of a hydraulic model was investigated in this research. To assess the accuracy of the model in predicting water surface elevation, two sets of performance metrics were used for calibration. Furthermore, flood extent was calibrated and validated using the measure of fit *F*, which was computed by comparing model predictions with observed satellite imagery. This performance evaluation provides valuable insights into the sensitivity of the model to Manning’s n-values and the appropriateness of different metrics for hydraulic modelling.

When plotting simulated water surface elevations in the profile lines from the model results, variations in the water surface elevation along the profile occur when using the shallow water equation. There will always be uncertainty in both the simulated and observed water surface elevation. For instance, when measuring water surface elevations, there can be uncertainty in several factors. These sources can be the accuracy and precision of the instrument, human error, environmental factors, spatial variability, and temporal variability. Therefore, an assumption was made, that the uncertainty in the simulated and observed water surface elevations offsets each other. This assumption means that any errors and uncertainties in the model are balanced by error or uncertainties in the measurement, resulting in that no measures were taken to evaluate or quantify the uncertainties.

To account for the variability in the simulated water surface elevations at the profile lines used for the performance evaluation, an average of the observed water surface elevation along the profile line was calculated.

As part of the evaluation of the performance of the model the statistical measures Mean Absolute Error (MAE) and Root Mean Squared Error (RMSE) was used. Both measures have their strength and weaknesses, MAE is more robust to outliers since it does not square the differences, while RMSE puts more weight on large errors. Accordingly, RMSE can be used to reduce large errors in the model, while MAE can be used to minimize the overall difference between the simulated and observed values.

MAE measures the average absolute difference between simulated and observed values with the equation written as:

$$MAE = \frac{1}{n}\sum_{i=1}^{n}|SWE_{obs} - SWE_{sim}| \quad (14)$$

RMSE measures the average squared difference between simulated and observed values, taking the square root of the result with the equation written as:

$$RMSE = \sqrt{\frac{1}{n}\sum_{i=1}^{n}(SWE_{sim} - SWE_{obs})} \quad (15)$$

where SWE_{sim} is the simulated water surface elevation, and SWE_{obs} is the observed water surface elevation in both equations.

Both MAE and RMSE have their advantages and limitations, so to provide a more comprehensive picture of the model performance they were reported together.

The measures of fit used when comparing flood extent maps derived from SAR imagery with flood extent from the model have been proven to provide reliable results in comparing different model outputs across various reaches and flood events in flood inundation modeling problems (Horritt, 2006; Horritt et al., 2007). These measures are represented by the following equations:

$$F^1 = \frac{A}{A+B+C} \quad (16)$$

$$F^2 = \frac{A-B}{A+B+C} \quad (17)$$

where A is the flood area that are correctly predicted by the model, B is the predicted flood area that is observed dry (over-prediction), C is the flooded area not predicted by the model (under-prediction). The value of F^1 can range from 0 to +1, while F^2 can range from -1 to +1, where values closer to +1 means better goodness of fit.

In the numerator of the equation F^2, the term negative B is used to penalize the model for over-prediction, meaning that the model is given a lower score if it predicts more wet area than actually observed. This penalization is important because remote sensing imagery often captures multiple flood-related processes and tends to show a larger flood extent, whereas the model only incorporates a few of these processes, resulting in less

inundation of the floodplain (Di Baldassarre et al., 2009). By penalizing over-prediction, F^2 has been found to give better results when assessing the performance of the model (Horritt et al., 2007).

On the other hand, F^1 does not penalize over-prediction. It simply calculates the ratio of correctly predicted flood area *(A)* to the sum of correctly predicted flood area, predicted dry area *(B),* and flood area not predicted by the model *(C)*. However, it still can be a good measure of fit for models that significantly overpredict inundated area (Horritt et al., 2007).

In summary, F^2 is the preferred measure since it penalizes model over-prediction, providing more realistic assessment of the goodness of fit in the model. Nevertheless, F^1 is still useful, but it may give a relatively high score even if the model over-predicts the flood extent significantly. Therefore, both measures were used when evaluating the calibration and validation of the different modelled flooding events compared to SAR imagery.

4 Results

4.1 Evaluating the flood event, August 14, 2003

4.1.1 Calibration of Manning's n-values

The results of the calibration process, involving various Manning's n-values ranging from 0.02 to 0.1 for the main channel and floodplains, are shown in Figure 40. The objective was to minimize the discrepancy between the observed and simulated water surface elevations. To achieve this, a strategy was employed to explore all combinations of Manning's n-values within the literature-based range, while avoiding unrealistic values that could compromise the calibration. The remaining Manning's n-values for the other land cover types were held constant to minimize the number of variations and subsequent simulation runs. The optimal MAE and RMSE values, measured at 0.29 m and 0.43 m respectively, were obtained when the Manning's n-value for the channel was set to 0.03 and 0.1 for the floodplains.

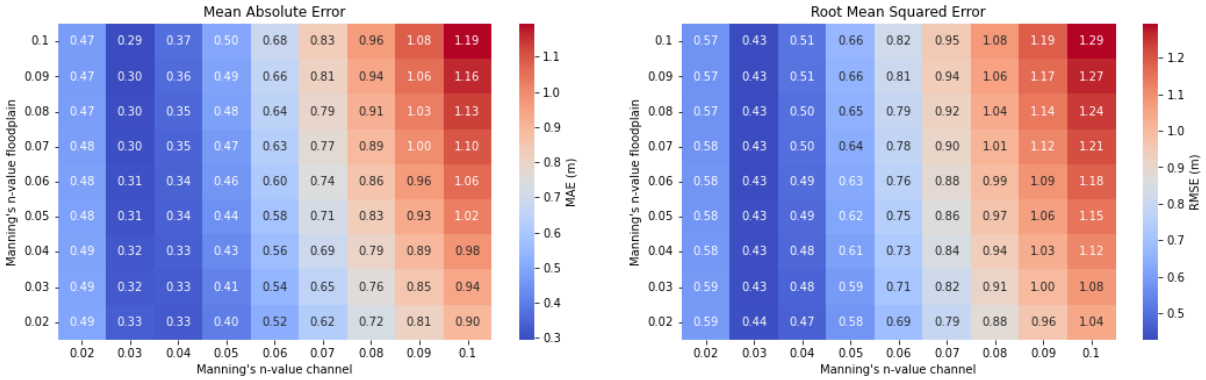

Figure 40: Heatmap illustrating the results from the calibration of the flood event on August 14, 2003. Left: MAE plotted against varying Manning's n-values. Right: RMSE plotted against varying Manning's n-values.

The contour plots from the same calibration process are shown in Figure 41. The contour plot provides further insights into the effectiveness of different parameter settings in the calibration process. The tendency observed in the contour plot is that the optimal parameter set, based on the MAE results, is 0.03 for the Manning's n-value in the main channel, and 0.09 – 0.1 for the floodplains. However, Manning's n-values between 0.028 and 0.042 for the main channel and values between 0.02 and 0.01 for the floodplain will still provide reasonably accurate results compared to the optimal parameter set. In contrast, the RMSE results indicate a narrower range of optimal parameters for the Manning's n-value in the main channel, with optimal values between 0.03 and 0.033, but a broader range for the floodplains, with values between 0.02 and 0.1.

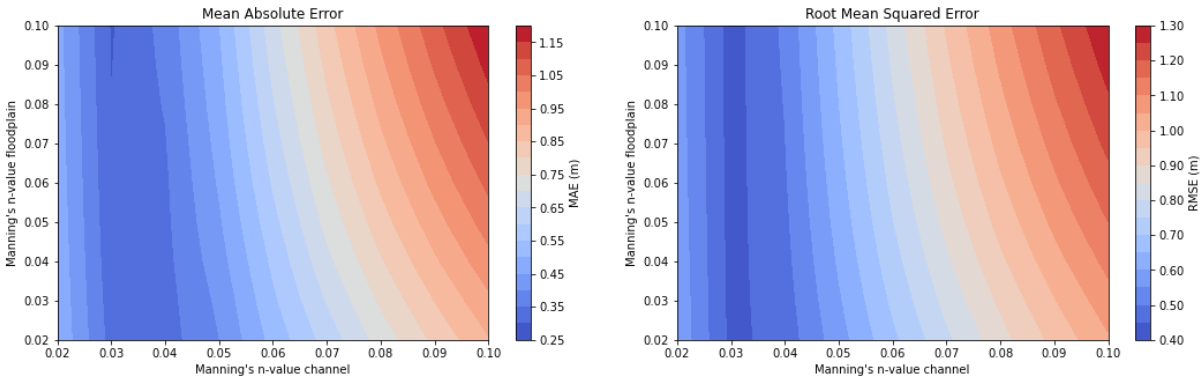

Figure 41: Contour plot illustrating the results from the calibration of the flood event on August 14, 2003. Left: MAE plotted against varying Manning's n-values. Right: RMSE plotted against varying Manning's n-values.

The differences between observed and simulated water surface elevations at each profile line using the best parameter set for the Manning's n-values in the main channel and floodplain are shown in Figure 42. Noteworthy, the largest deviations are observed in profile lines 2, 7, 8, and 9, with values of 0.36 m, 0.70 m, -0.27 m, and -1.03 m, respectively. Negative values indicate an overestimation of simulated water surface elevations, while positive values indicate an underestimation.

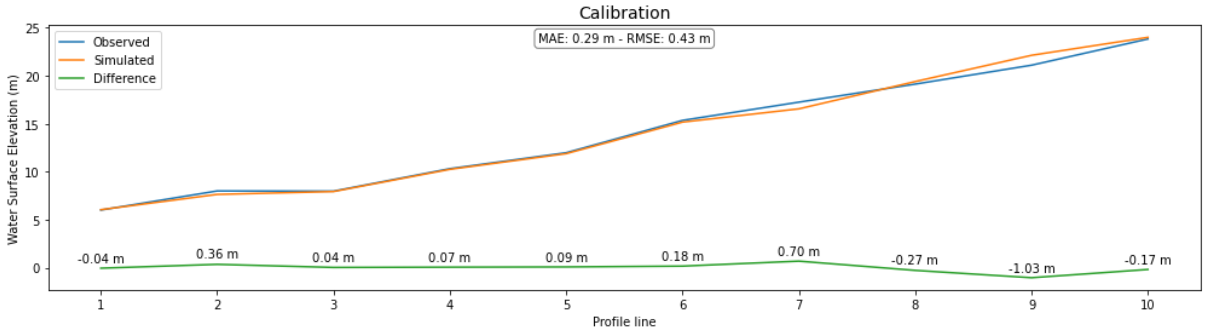

Figure 42: Plot of observed and simulated water surface elevations at each profile line, with a difference line showing the discrepancy, using the optimal parameter set from the calibration of the flood event on August 14, 2003.

4.1.2 Fine-tuned calibration of Manning's n values

To investigate if the MAE and RMSE performance metrics would further improve, a fine-tuned calibration was performed, specifically focusing on the Manning's n-value in the channel. The range of 0.025 to 0.035 was chosen for the Manning's n-value in the channel based on the results from the initial calibration, which showed the best performance within this range. For the floodplain, a range of 0.02 to 0.1 was tested for all the main channel values. The results from the fine-tuned calibration showed a slight improvement in MAE, reducing it to 0.28 m, a decrease of 0.01 m. The RMSE value remained the same at 0.43 m. The optimal parameter set obtained from the fine-tuned calibration is shown in Figure 43, with Manning's n-values of 0.28 for the main channel and 0.1 for the floodplains.

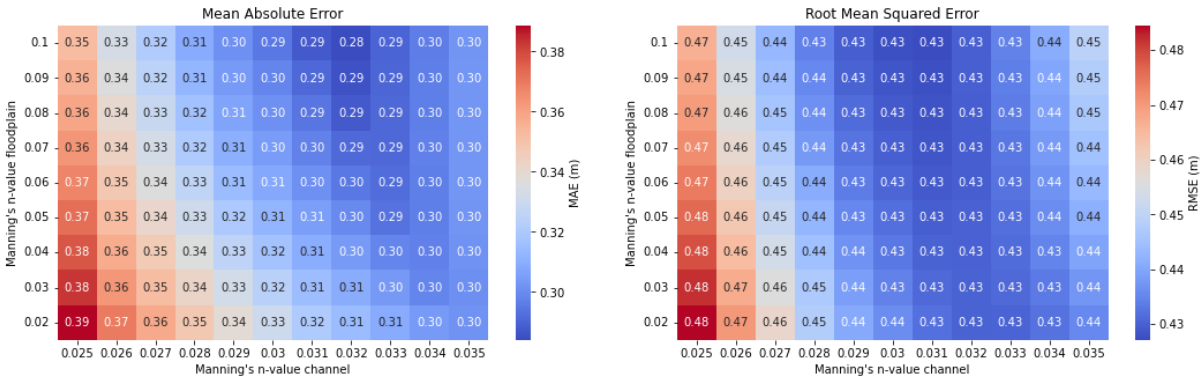

Figure 43: Heatmap illustrating the results from the fine-tuned calibration of the flood event on August 14, 2003. Left: MAE plotted against varying Manning's n-values. Right: RMSE plotted against varying Manning's n-values.

The fine-tuned calibration process, visualized in Figure 44, reveals a range of Manning's n-values that yield respectable outcomes in terms of MAE and RMSE values. The contour plot demonstrates the effectiveness of different parameter settings. Based on the MAE results, the optimal Manning's n-values for the main channel lie within the range of 0.031 to 0.033, while for the floodplain, they range from 0.08 to 0.1. Within these ranges, the model demonstrates good performance. Similarly, the RMSE results indicate that the main channel achieves the best accuracy with Manning's n-values between 0.030 and 0.032, while the floodplain values range from 0.06 to 0.1. These findings emphasize the impact of the fine-tuned calibration process on the model performance.

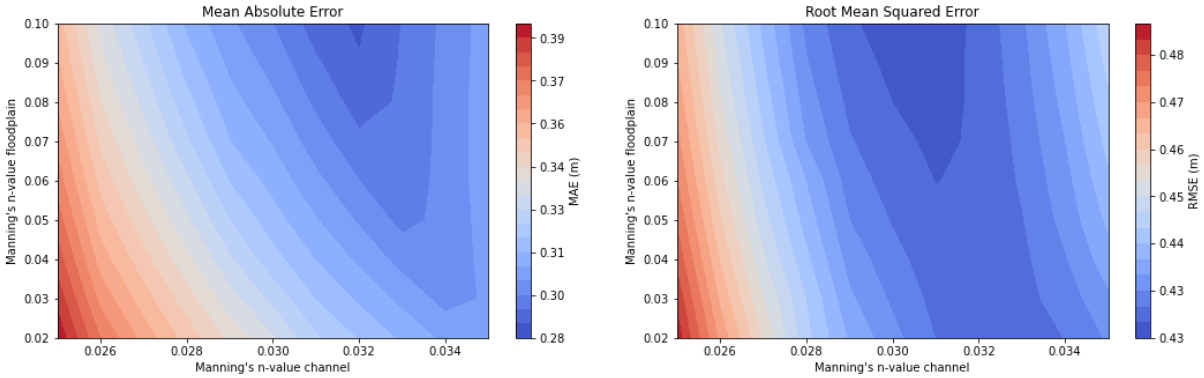

Figure 44: Contour plot illustrating the results from the fine-tuned calibration of the flood event on August 14, 2003. Left: MAE plotted against varying Manning's n-values. Right: RMSE plotted against varying Manning's n-values.

The comparison between observed and simulated water surface elevations at each profile line using the optimal parameter set for the Manning's n-values in the main channel and floodplain is presented in Figure 45. Notably, significant deviations are still observed in profile lines 2, 7, 8, and 9, with deviations of 0.32 m, 0.61 m, -0.31 m, and -1.09 m, respectively. Negative values indicate an overestimation of simulated water surface elevations, while positive values suggest an underestimation.

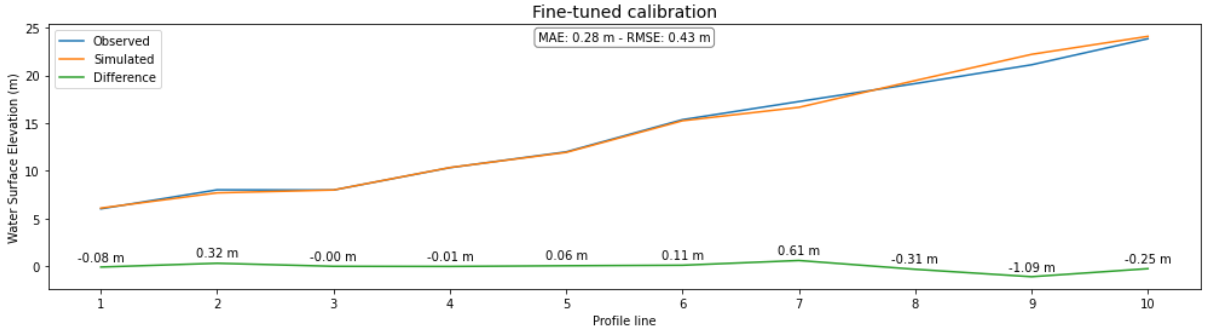

Figure 45: Plot of observed and simulated water surface elevations at each profile line, with a difference line showing the discrepancy, using the optimal parameter set from the fine-tuned calibration of the flood event on August 14, 2003.

The optimal parameter set from the fine-tuned calibration yields a flood inundation area of 5.10 km^2 within the study area shown in Figure 46.

Figure 46: Flood inundation area from the flood event on August 14, 2003, using the optimal parameter set from the fine-tune-calibration.

4.1.3 Regionalized calibration of Manning's n-values in main channel

The regionalized calibration approach will help address the challenges associated with accurately representing water surface elevations in different areas, leading to improved model accuracy and reliability. In the calibration and fine-tuned calibration processes, a single Manning's n-value was used for the entire channel reach. However, in reality, natural rivers exhibit variations in Manning's n-values along their course. To account for this, a regionalized calibration approach was employed, dividing the river into Manning's regions as shown in Figure 47. Each region was assigned a specific Manning's n-value to minimize the discrepancy between observed and simulated water surface elevations.

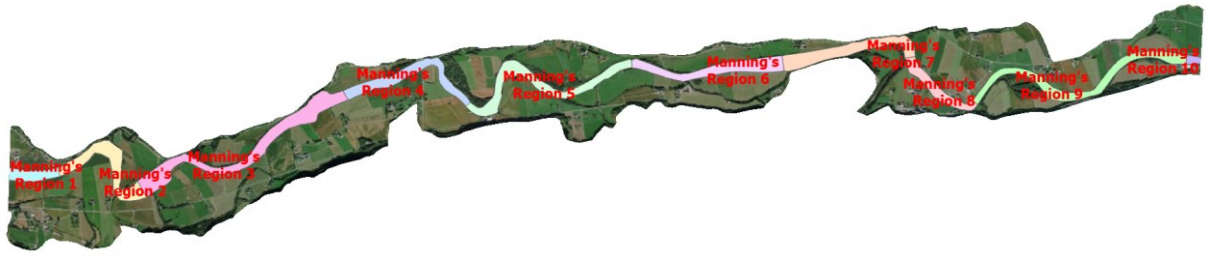

Figure 47: Manning's regions inside the study area used in the regionalized calibration approach of the flood event on August 14, 2003.

Through a trial-and-error process of adjusting the size of the Manning's regions and adjusting the Manning's n-value within the regions, with several iterations, the regionalized calibration resulted in a MAE of 0.02 m and a RMSE of 0.04 m. These

metrics indicate the level of agreement between the observed and simulated water surface elevations and was achieved when using the Manning's n-values listed in Table 9.

Table 9: Manning's n-values main channel assigned to Manning's regions.

Manning's region	Manning's n-value main channel
1	0.030
2	0.057
3	0.018
4	0.037
5	0.054
6	0.038
7	0.050
8	0.009
9	0.004
10	0.042

The comparison of observed and simulated water surface elevations at each profile line, utilizing the Manning's n-values obtained from the regionalized calibration, is depicted in Figure 48. The discrepancies between observed and simulated values have been minimized, with many profile lines exhibiting a difference of 0 m. However, slight deviations are observed in profile lines 2, 3, and 8, with deviations of 0.07 m, -0.09 m, and -0.01 m, respectively. Negative deviations indicate an overestimation of simulated water surface elevations, while positive deviations indicate an underestimation. These results demonstrate a significant improvement in accuracy, as the MAE and RMSE values approach zero, indicating a high level of agreement between observed and simulated values.

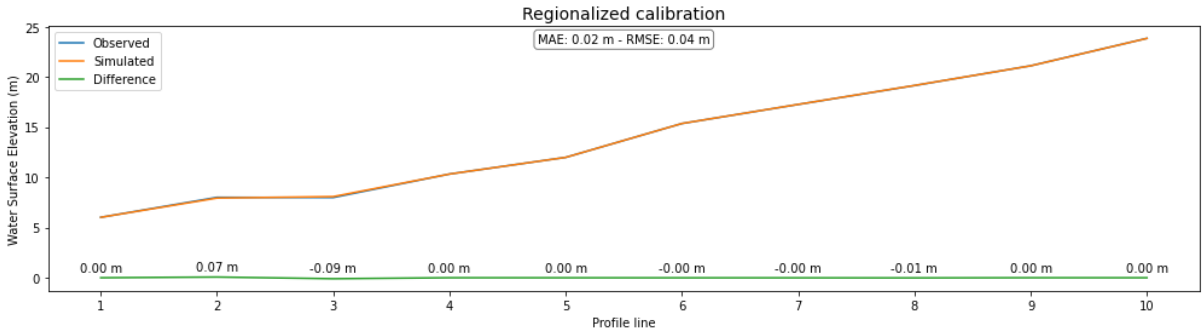

Figure 48: Plot of observed and simulated water surface elevations at each profile line, with a difference line showing the discrepancy, using Manning's n-values in the main channel from the regionalized calibration of the flood event on August 14, 2003.

The Manning's n-values that provided the best performance of the model, hence the lowest MAE and RMSE values from the regionalized calibration yields a flood inundation area of 4.19 km^2 within the study area as shown in Figure 49.

Figure 49: Flood inundation area from the flood event on August 14, 2003, using Manning's n-values in the main channel from the regionalized calibration.

4.1.4 Model sensitivity to Manning's n-values

The study area primarily comprises three main land cover types: the main channel, floodplains (including complete soil cultivated, surface cultivated soil, and infield grazing), and forest. These land cover types account for approximately 12.2%, 62%, and 15.4% of the total area, respectively. The remaining land cover types collectively represent the remaining percentages. Therefore, to assess the sensitivity of the model, an evaluation of the performance and behaviour of the model was made for these three main land cover types.

The model sensitivity was assessed by varying the Manning's n-value in the main channel, specifically using values of 0.02 and 0.1, while keeping the remaining Manning's n-values at their reference levels. The resulting flood extent from both Manning's n-values are showed Figure 50. The blue area represents the overlapping region where both simulations coincide. In contrast, the black area corresponds to the additional flooded area resulting from the use of a Manning's n-value of 0.1, extending beyond the overlapping region. The flood inundation area within the study area is 4.01 km^2 when using a Manning's n-value of 0.02. However, when a Manning's n-value of 0.1 is used, the inundation area expands to 7.01 km^2. This indicates an additional flooded area of 3.0 km^2 resulting from the use of the higher Manning's n-value. When utilizing a Manning's n-value of 0.02 in the main channel, the MAE and RMSE are calculated to be 0.48 m and 0.58 m, respectively. However, when the Manning's n-value is increased to 0.1, the MAE and RMSE values rise to 1.02 m and 1.15 m, respectively.

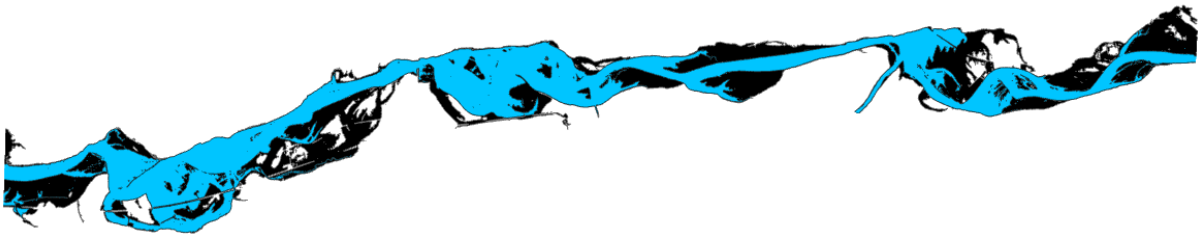

Figure 50: Flood inundation area from the flood event on August 14, 2003, using Manning's n-values 0.02 and 0.1 in the main channel. The blue area indicates the region where both simulations overlap and coincide. The black area represents the additional flooded area when a Manning's n-value of 0.1 is used, extending beyond the overlapping region.

To further investigate the sensitivity of the model, the Manning's n-value for the floodplains was evaluated using values of 0.02 and 0.1. The Manning's n-value of 0.032 in the main channel, determined as the best parameter from the fine-tuned calibration, was retained. The remaining Manning's n-values for other land cover types were kept at their reference levels. Figure 51 displays the flood extent resulting from the simulations using the two different Manning's n-values for the floodplains. The blue area represents

the overlapping region where both parameter sets produce similar flood extents. On the other hand, the black area indicates the additional flooded region that arises when using a Manning's n-value of 0.1 in the floodplains, extending beyond the overlapping area.

When a Manning's n-value of 0.02 is applied to the floodplains, the flood inundation area measures 4.86 km^2. In comparison, utilizing a Manning's n-value of 0.1 yields a flood inundation area of 5.10 km^2, representing an expansion of approximately 0.26 km^2.

The MAE and RMSE values when using a Manning's n-value of 0.02 are 0.31 m and 0.43 m, respectively. When employing a Manning's n-value of 0.1, the MAE remains at 0.28 m, while the RMSE remains unchanged at 0.43 m.

Figure 51: Flood inundation area from the flood event on August 14, 2003, using Manning's n-values 0.02 and 0.1 for the floodplains. The blue area indicates the region where both simulations overlap and coincide. The black area represents the additional flooded area when a Manning's n-value of 0.1 is used, extending beyond the overlapping region.

The land cover type "forest" was the last Manning's n-value that was assessed, which constitutes a substantial portion of the study area, covering 15.4 % of the total area. The Manning's n-value for the main channel was set to 0.32, determined as the best parameter from the fine-tuned calibration. The remaining Manning's n-values for other land cover types were maintained at their reference levels. In the literature, the Manning's n-value for forests typically ranges from 0.1 to 0.2 in the study area. Therefore, increments of 0.01 were examined to cover the range of Manning's n-values for forests, while simultaneously increasing the Manning's n-values for the floodplains from 0.02 to 0.1 through all the forest increments.

The results from the simulations, presented in Figure 52, indicate that the optimal MAE achieved is 0.28 m by utilizing a Manning's n-value of 0.1 for the floodplain and a Manning's n-value of 0.15 for the forest area. On the other hand, the best RMSE value obtained is 0.42, with a Manning's n-value of 0.1 for the floodplains and 0.1 for the forests.

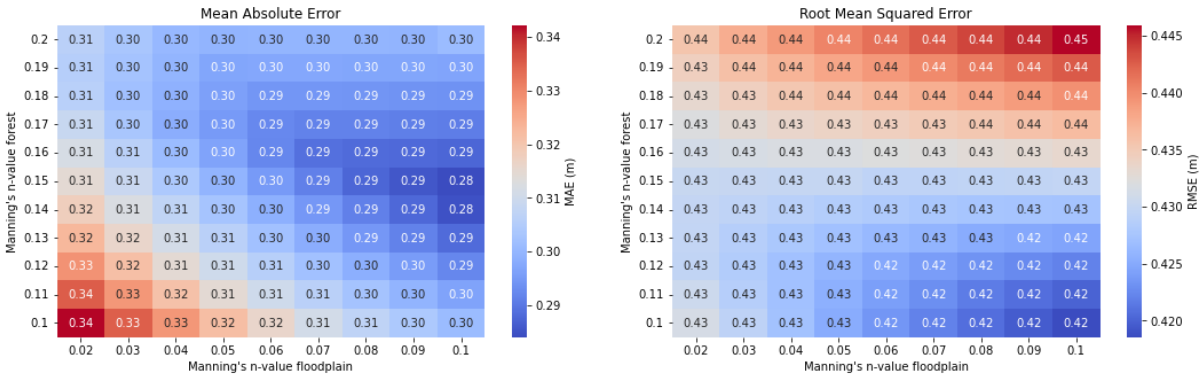

Figure 52: Heatmap of results when analyzing the land cover type "forest" during the flood event on August 14, 2003. Left: MAE plotted against varying Manning's n-values. Right: RMSE plotted against varying Manning's n-values.

To visually analyse the impact of different Manning's n-values on the performance of the model, a contour plot was generated and is presented in Figure 53. The contour plot provides insights into the relationship between the variations in Manning's n-values for the floodplain and forest and the corresponding model performance.

Upon examining the plot, it becomes evident that the model achieves the best MAE performance when utilizing Manning's n-values within the range of 0.08 to 0.1 for the floodplain and 0.14 to 0.16 for the forest. In contrast, the best RMSE performance is attained by employing Manning's n-values between 0.09 and 0.1 for the floodplain, and 0.1 and 0.11 for the forest.

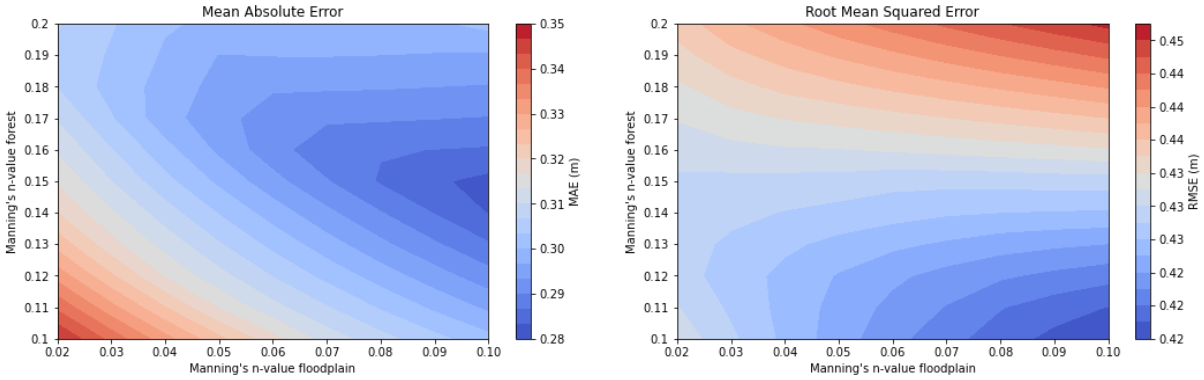

Figure 53: Contour plot of the results when analyzing the land cover type "forest" during the flood event on August 14, 2003. Left: MAE plotted against varying Manning's n-values. Right: RMSE plotted against varying Manning's n-values.

To assess the sensitivity of the model to variations in Manning's n-value for the forest, a flood inundation map was created. This map, presented in Figure 54, displays the distribution of flood areas for two scenarios: using the minimum Manning's n-value of 0.1 and the maximum Manning's n-value of 0.2 for the forest. In the map, the blue area represents the region where both sets of parameter values yield similar flood extents, while the black area indicates the additional flooded region that arises when a Manning's n-value of 0.2 is applied to the forest. This portion of the map extends beyond the overlapping area, signifying that a higher Manning's n-value leads to a larger flood extent compared to the lower value.

When a Manning's n-value of 0.1 is applied to the forest, the flood inundation area measures 4.93 km^2. In contrast, utilizing a Manning's n-value of 0.2 results in a larger

flood inundation area of 5.24 km^2. This represents an expansion of approximately 0.31 km^2 when the higher Manning's n-value is used, highlighting the sensitivity of the flood extent to changes in the forest's Manning's n-value.

Figure 54: Flood inundation area from the flood event on August 14, 2003, using Manning's n-values 0.1 and 0.2 for the forest, and 0.1 for floodplains. The blue area indicates the region where both simulations overlap and coincide. The black area represents the additional flooded area when a Manning's n-value of 0.2 for forest is used, extending beyond the overlapping region.

4.1.5 Validation of the calibrations using SAR imagery

The best set of Manning's n-values from the fine-tuned and regionalized calibration from the August 14, 2003, flood event, is validated with Sentinel-1 SAR imagery of captured floods over the study area within the time-period when the satellites in the Sentinel-1 program has been active. Furthermore, the calibrations are also validated with vector data of the flood event that occurred during Storm Gyda, which was derived from the EMSR product created by Copernicus Emergency Management Service. The flood delineation maps from the satellite imagery are overlayed the simulated flood inundation maps, creating areas that shows where the model correctly predicts, over-predicts, or under-predicts simulated flooded areas, respectively with the colour blue, black and pink. Additionally, the forest resource map SR16 was merged with the flood delineation maps to examine the impact of forests on the results. Forests can obstruct SAR imagery, making it challenging to capture images of water that is concealed beneath the forest canopy. By combining the forest information from SR16 with flood delineation maps, a more comprehensive understanding can be gained regarding the influence of forests on flood mapping accuracy and the detection of water-covered areas.

The measure of fit F^1 and F^2 are calculated based on the flood overlay maps, as depicted in Figure 55 and Figure 56. These measures serve as indicators to evaluate the performance of the simulated flood events when comparing them to real-world observations using the Manning's n-value obtained from the fine-tuned calibration and regionalized calibration. The flood overlay maps provide a visual representation of the agreement or discrepancy between the simulated flood extent and the flood extent from satellite imagery.

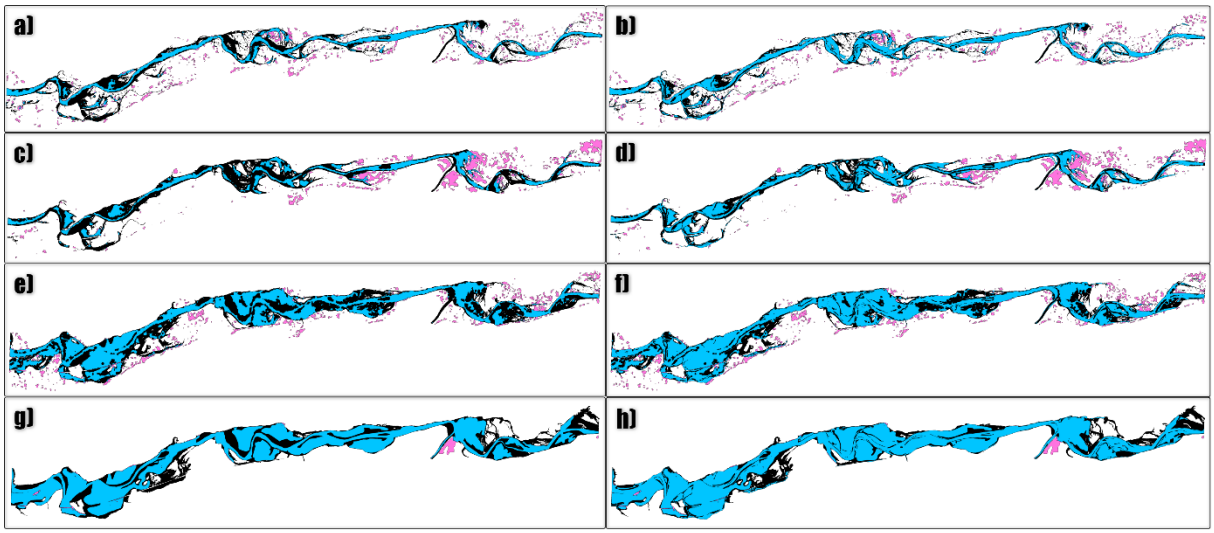

Figure 55: Flood overlay plots used for validation of the fine-tuned calibration of the August 14, 2003, flood event. (a) Flood event, November 26, 2016. (b) Flood event, November 26, 2016, with merged SR16 map and SAR binary map. (c) Flood event, January 21, 2020. (d) Flood event, November January 21, 2020, with merged SR16 map and SAR binary map. (e) Flood event, November 24, 2021. (f) Flood event, November 24, 2021, with merged SR16 map and SAR binary map. (g) Flood event, January 13, 2022. (h) Flood event, January 13, 2022, with merged SR16 map and SAR binary map. Blue: correctly predicted. Black: over-predicted. Pink: under-predicted.

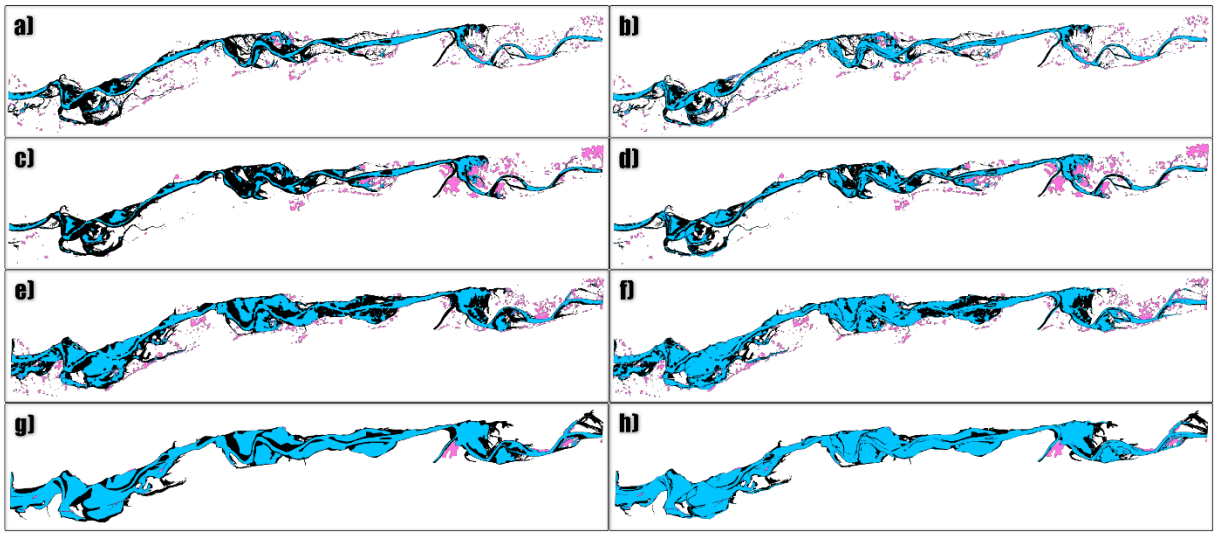

Figure 56: Flood overlay plots used for validation of the regionalized calibration of the August 14, 2003, flood event. (a) Flood event, November 26, 2016. (b) Flood event, November 26, 2016, with merged SR16 map and SAR binary map. (c) Flood event, January 21, 2020. (d) Flood event, November January 21, 2020, with merged SR16 map and SAR binary map. (e) Flood event, November 24, 2021. (f) Flood event, November 24, 2021, with merged SR16 map and SAR binary map. (g) Flood event, January 13, 2022. (h) Flood event, January 13, 2022, with merged SR16 map and SAR binary map. Blue: correctly predicted. Black: over-predicted. Pink: under-predicted.

The measure of fit F^1 and F^2 from the validation of the fine-tuned calibration and regionalized calibration is presented in Table 10. The results are reported with measure of fit values from the comparison of simulated flood inundation maps with flood delineation maps, and flood inundation maps compared with flood delineation maps merged with the forest resource map SR16.

Table 10: Flood events used in validation of the fine-tuned and regionalized calibration. F^1 and F^2 values presented both with and without SR16 map merged with flood delineation map. (FTC = Fine-tuned calibration, RC = Regionalized calibration).

	Flood delineation map				Flood delineation map + SR16			
	FTC		RC		FTC		RC	
Flood event	F^1	F^2	F^1	F^2	F^1	F^2	F^1	F^2
2016-11-26	0.34	-0.16	0.36	-0.13	0.50	0.15	0.53	0.22
2020-01-21	0.29	-0.25	0.30	-0.21	0.45	0.07	0.47	0.14
2021-11-24	0.50	0.10	0.49	0.07	0.62	0.34	0.61	0.31
2022-01-13	0.66	0.34	0.63	0.27	0.79	0.60	0.75	0.52

4.2 Evaluating the flood event, November 24, 2021

4.2.1 Calibration of Manning's n-values

The calibration of the flood event that occurred November 24, 2021, that had a flood peak of 583 m^3/h was based on comparing the flood delineation map from the Sentinel-1 SAR image as shown in Figure 57, with flood inundation maps from the simulations with different Manning's n-value combinations.

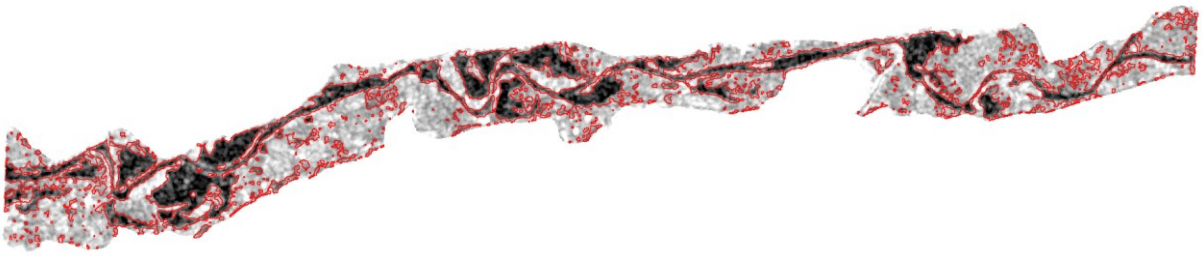

Figure 57: Flood delineation from Sentinel-1 SAR image of flood event, November 24, 2021, inside the area of interest. Red color is the flood delineation line that mark the potential wet pixels by utilizing the threshold method.

The calibration process aimed to minimize the discrepancy between the observed and simulated flood extent by adjusting Manning's n-values for the main channel and floodplains. Manning's n-values ranging from 0.02 to 0.1 were explored, which are within literature-based range while avoiding unrealistic values that could compromise the calibration. To minimize variations and simulation runs, the Manning's n-values for other land cover types were held constant. The best measure of fit F^1 and F^2, measured at 0.54 and 0.21 respectively, were obtained when the Manning's n-value for the channel was set to 0.02 and 0.02 for the floodplains as shown in Figure 58.

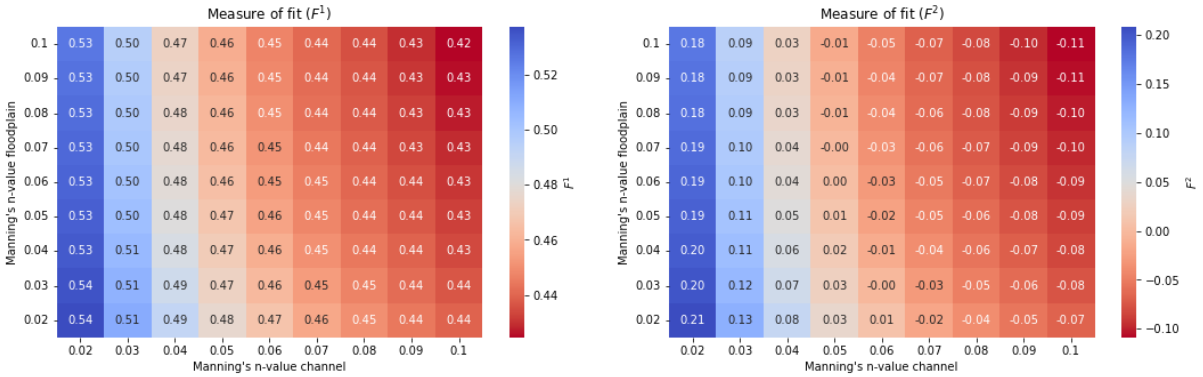

Figure 58: Heatmap illustrating the results from the calibration of the flood event on November 24, 2021. Left: F^1 plotted against varying Manning's n-values. Right: F^2 plotted against varying Manning's n-values.

The calibration process, as depicted in Figure 59, provides a visualization of the relationship between Manning's n-values and the corresponding F^1 and F^2 values. The contour plot illustrates the effectiveness of different parameter settings in achieving optimal outcomes.

Based on the results of F^1 and F^2, the optimal Manning's n-values for the main channel fall within the range of 0.02 to 0.03, while for the floodplain, they range from 0.02 to 0.1. Within these ranges, the model demonstrates the best performance in terms of simulating the observed flood extent.

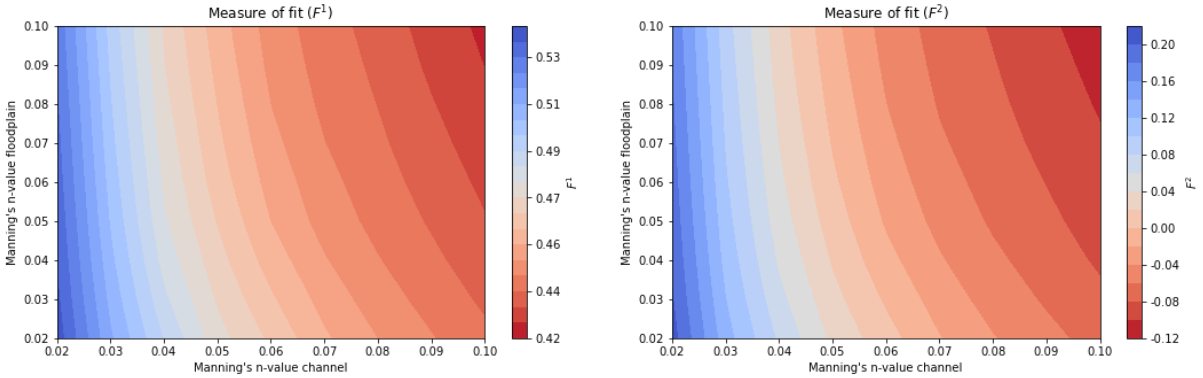

Figure 59: Contour plot illustrating the results from the calibration of the flood event on November 24, 2021. Left: F^1 plotted against varying Manning's n-values. Right: F^2 plotted against varying Manning's n-values.

The measure of fit F^1 and F^2 are calculated by using the areas where the model correctly predicts flood (blue), where it over-predicts (black), and where it under-predicts (pink) as illustrated in Figure 60. When using the best measure of fit Manning's n-values from the calibration the correctly predicted area is 2.47 km^2, the over-prediction is 1.51 km^2, while the under-predicted area is 0.61 km^2.

Figure 60: Flood overlay plot from the flood event on November 24, 2021, using best measure of fit Manning's n-values 0.02 in the main channel and floodplains. The blue area indicates the region the simulation and flood delineation map of the SAR image overlap and coincide. The black area represents the over-prediction from the simulation, while the pink is illustrating the under-prediction.

The forest resource map SR16 was combined with the flood delineation map derived from the SAR image of the flood event to examine the impact of forests on the outcomes. The results of this integration are illustrated by the measures F^1 and F^2, as shown in Figure 61. By utilizing Manning's n-values of 0.02 for both the main channel and floodplains, the calibration process yields a F^1 value of 0.67 and an F^2 value of 0.46.

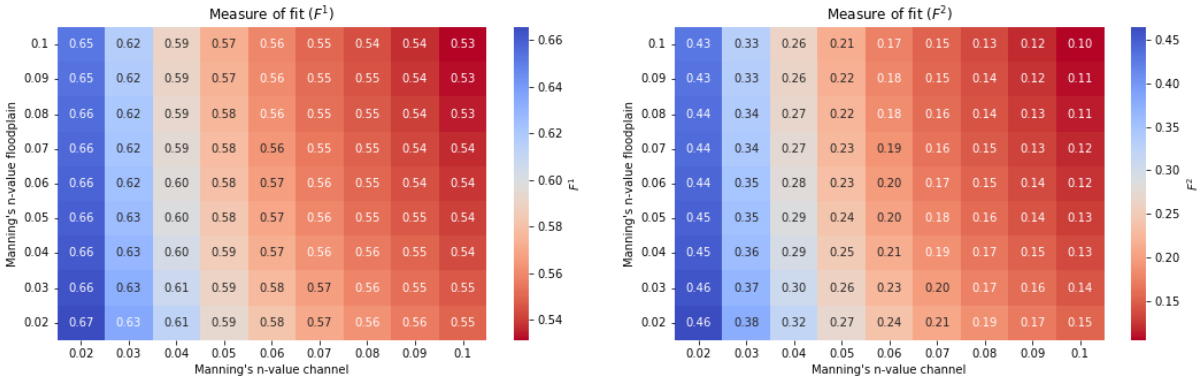

Figure 61: Heatmap illustrating the results from the calibration of the flood event on November 24, 2021, when integrating SR16. Left: F^1 plotted against varying Manning's n-values. Right: F^2 plotted against varying Manning's n-values.

The contour plot, represented in Figure 62, offers a visual representation of the correlation between Manning's n-values and their corresponding F^1 and F^2 values. It effectively showcases the efficacy of different parameter configurations, indicating that the most favorable Manning's n-values for the main channel lie within the range of 0.02 and 0.03, while for the floodplain, the optimal values range from 0.02 to 0.1. It is within these specified ranges that the model exhibits the highest performance in accurately simulating the observed flood extent when adding the forest resource map SR16.

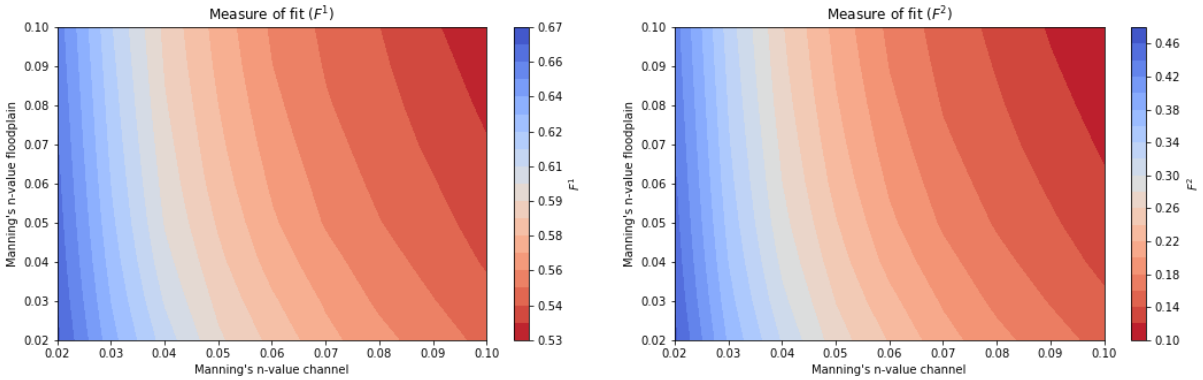

Figure 62: Contour plot illustrating the results from the calibration of the flood event on November 24, 2021, when integrating SR16. Left: F^1 plotted against varying Manning's n-values. Right: F^2 plotted against varying Manning's n-values.

The measure of fit, F^1 and F^2, is determined based on the classification of predicted flood areas into three categories: correctly predicted (blue), over-predicted (black), and under-predicted (pink), as visualized in Figure 63. By utilizing the SR16 map merged with the flood inundation map from the SAR image the model achieves a correctly predicted area of 3.06 km^2, it exhibits an over-prediction of 0.92 km^2, and under-predicts an area of 0.61 km^2.

Figure 63: Flood overlay plot from the flood event on November 24, 2021, using best measure of fit Manning's n-values 0.02 in the main channel and floodplains. The blue area indicates the region the simulation and flood delineation map of the SAR image merged with SR16 map overlap and coincide. The black area represents the over-prediction from the simulation, while the pink is illustrating the under-prediction.

4.2.2 Validating using SAR imagery and observed water surface elevations

The validation of the November 24, 2021, flood event is done using the Manning's n-value that gave the best measure of fit when calibrating the model. The Manning's n-value of 0.02 in the main channel, and 0.02 in the floodplains, while keeping the rest as the reference levels was validated against the flood events from:

- August 14, 2003
- November 26, 2016
- January 21, 2020
- January 13, 2022

The simulated flood inundation maps are overlayed the flood delineation maps from the respective floods simulated, resulting in the areas representing the correctly predicted flood areas (blue), over-predicted flood areas (black), and under-predicted flood areas (pink), as depicted in Figure 64.

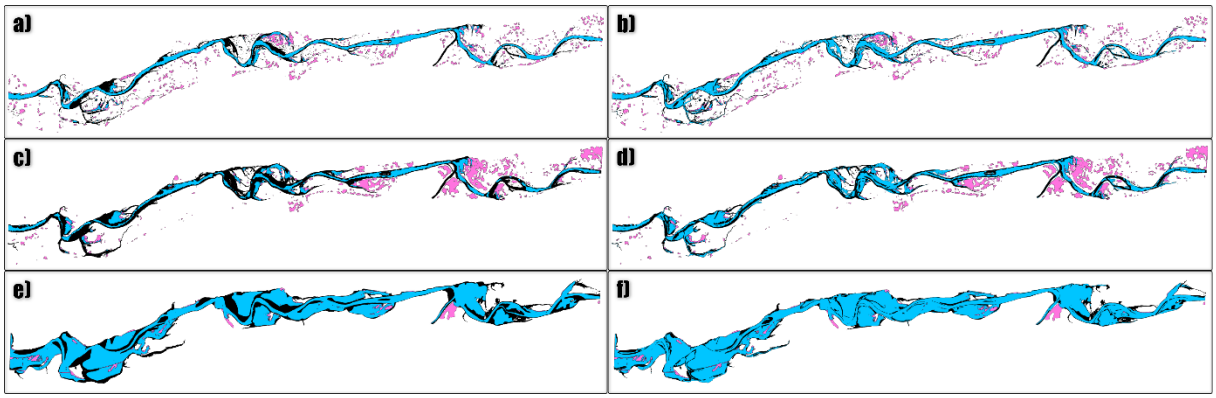

Figure 64: Flood overlay plots used for validation of the calibration of the November 24, 2021, flood event. (a) Flood event, November 26, 2016. (b) Flood event, November 26, 2016, with merged SR16 map and SAR binary map. (c) Flood event, January 21, 2020. (d) Flood event, November January 21, 2020, with merged SR16 map and SAR binary map. SR16 map and SAR binary map. (e) Flood event, January 13, 2022. (f) Flood event, January 13, 2022, with merged SR16 map and SAR binary map. Blue: correctly predicted. Black: over-predicted. Pink: under-predicted.

Table 11 presents the measure of fit values, F^1 and F^2, obtained from the validation of the calibration process of the flood event from November 24, 2021. The results are reported by comparing the simulated flood inundation maps with the flood delineation maps, as well as the flood inundation maps compared to with the flood delineation maps merged with the forest resource map SR16.

Table 11: Flood events used in validation of the calibration of the November 24, 2021, flood event. F^1 and F^2 values presented both with and without SR16 map merged with flood delineation map.

	Flood delineation map		Flood delineation map + SR16	
Flood event	**F^1**	**F^2**	**F^1**	**F^2**
2016-11-26	0.40	0.05	0.54	0.33
2020-01-21	0.29	-0.14	0.46	0.20
2022-01-13	0.68	0.41	0.82	0.69

Furthermore, the calibration is validated by comparing the simulated water surface elevations with the observed water surface elevations from the flood event of August 14, 2003. Using the Manning's n-values obtained from the calibration process, the MAE and RMSE are calculated as 0.49 m and 0.59 m, respectively.

The difference between the observed and simulated water surface elevations along each profile line, employing the Manning's n-values that provide the best measure of fit in the main channel and floodplain from the calibration of the November 24, 2021, flood event, are depicted in Figure 65. It is notable that the simulation generally underestimates the water surface elevations along most profile lines, with the exception of profile line 9 where and overestimation occurs. Negative values signify an overestimation in the simulated water surface elevations, while positive values indicate an underestimation.

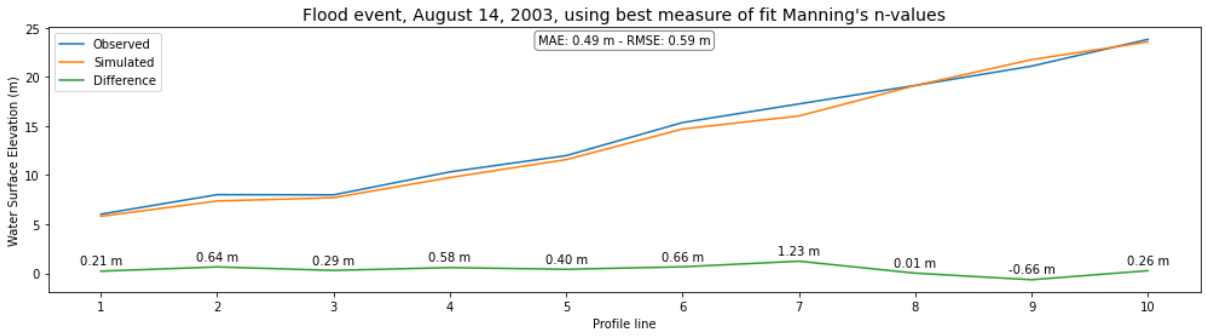

Figure 65: Plot of observed and simulated water surface elevations at each profile line, with a difference line showing the discrepancy, using the best measure of fit Manning's n-values from the calibration of the flood event on November 24, 2021.

4.3 Evaluating the flood event, January 14, 2022 (Storm Gyda)

4.3.1 Regionalized calibration of main channel and floodplains

The calibration process for the flood event that took place on November 24, 2021, achieved the best measure of fit by utilizing a Manning's n-value of 0.02 for both the main channel and floodplains. Subsequently, these optimized Manning's n-values were applied to simulate the flood event during Storm Gyda on January 14, 2022, resulting in measure of fit values of F^1 = 0.82 and F^2 = 0.69, when comparing against the flood delineation map derived from COSMO-SkyMed SAR image that was merged with the SR16 forest resource map. The simulation accurately predicted a flood area of 4.04 km^2, with an over-prediction of 0.66 km^2 and an under-prediction of 0.23 km^2.

To optimize the outcomes even further, a regionalized calibration was performed specifically for the Storm Gyda flood event, with particular emphasis placed on certain zones during the calibration process, as shown in Figure 66.

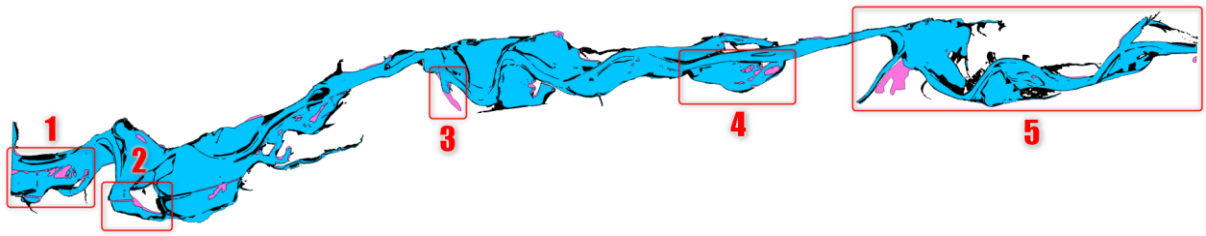

Figure 66: Storm Gyda flood event simulated using optimized Manning's n-values overlayed the flood delineation map derived from COSMO-SkyMed SAR image merged with the SR16 map, highlighting prioritized zones in the regionalized calibration. The colors represent the following: blue for correctly predicted areas, black for over-predicted areas, and pink for under-predicted areas.

As illustrated in Figure 66, zones 1-4 display noticeable under-prediction of the simulated flooded areas (pink areas), while zone 5 shows some over-prediction (black areas). In order to address this, Manning's calibration regions were created specifically for these zones to locally adjust the Manning's n-values inside the zones, as depicted in Figure 67.

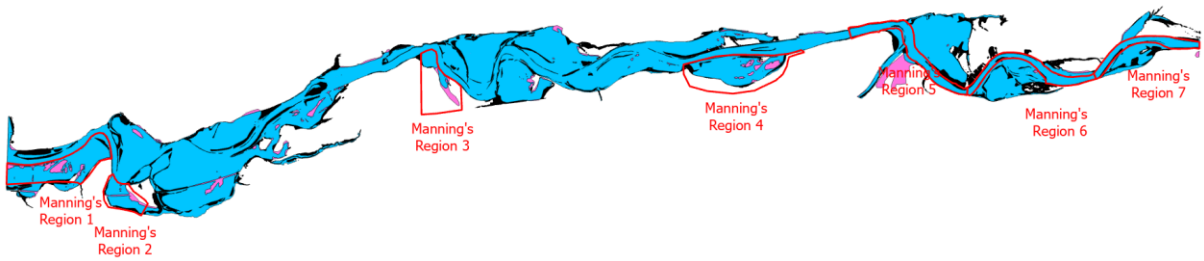

Figure 67: Manning's calibration regions to change the Manning's n-values inside the calibration zones.

To assess the impact of adjusting the Manning's n-values in the floodplains, the baseline Manning's n-values of 0.02 for floodplains and 0.15 for the forest were modified within the under-predicted zones. The baseline values fall within the lower- to mid-range based on existing literature. Therefore, within Manning's region 1-4, the Manning's n-values for floodplains and forest were increased to 0.1 and 0.2, respectively, which represent values in the upper range of Manning's n-values.

Figure 68 presents the results of the simulation using the newly adjusted Manning's n-values in calibration zones 1-4. These adjustments led to an increase in the accurately predicted flood areas, resulting in a total of 4.08 km^2. Additionally, there was a slight increase in the over-predicted areas, totaling 0.68 km^2. On the other hand, the under-predicted areas decreased to 0.19 km^2. However, the measure of fit values, F^1 and F^2, was unchanged, with the values of 0.82 and 0.69, respectively.

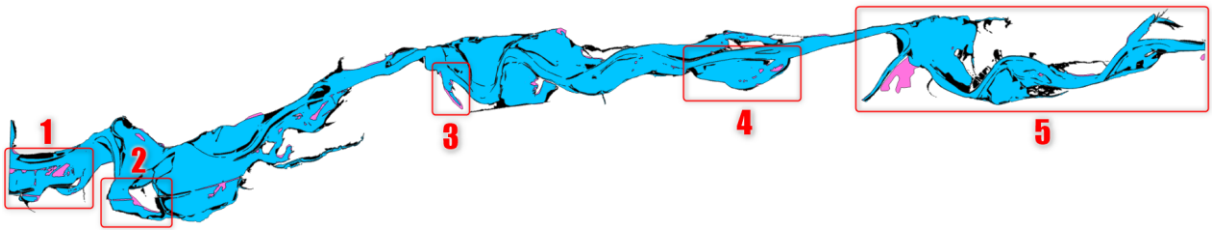

Figure 68: Storm Gyda flood event simulated using new Manning's n-values for zone 1-4, overlayed the flood delineation map derived from COSMO-SkyMed SAR image merged with the SR16 map. The colors represent the following: blue for correctly predicted areas, black for over-predicted areas, and pink for under-predicted areas.

The difference in flooded areas before and after changing the Manning's n-values for the floodplains and forest inside calibration zones 1-4 is illustrated in Figure 69, where (a) and (b) is zone 1, (c) and (d) is zone 2, (e) and (f) is zone 3, and (g) and (h) is zone 4.

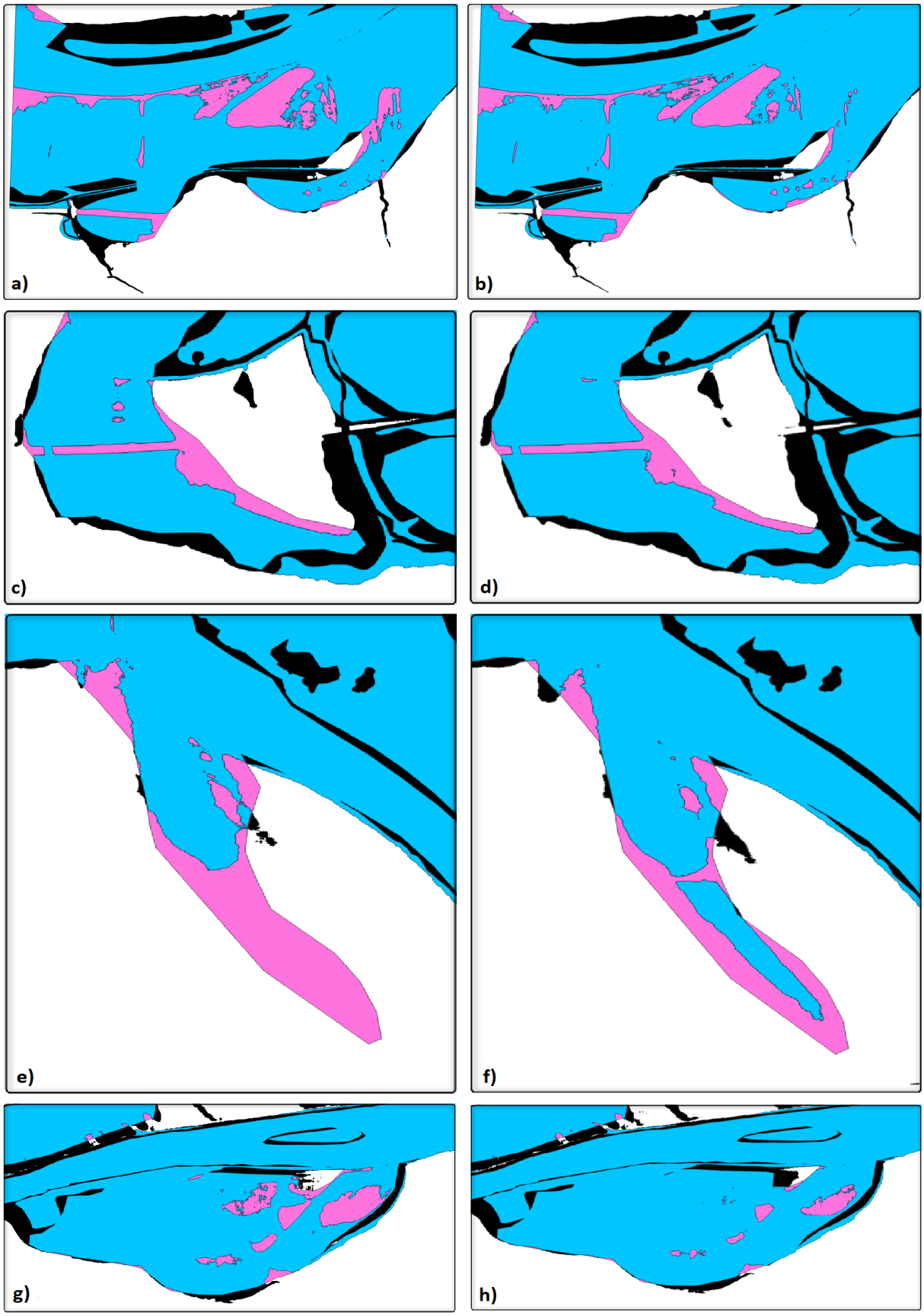

Figure 69: Zones 1-4, where (a) and (b) is zone 1, (c) and (d) is zone 2, (e) and (f) is zone 3, and (g) and (h) is zone 4, before and after changing Manning's n-value for floodplains and forest. Blue is correctly predicted, black is over-predicted, and pink is under-predicted.

To further improve the accuracy of the model, the calibration zone 5 was split into three Manning's calibration regions as displayed in Figure 67. Iterative simulations were performed in a trial-and-error approach to minimize the overestimation, adjusting the Manning's n-value in the main channel within each Manning's calibration region. The compilation of all the Manning's n-values employed in the regionalized calibration can be found in Table 12.

Table 12: Manning's n-values assigned to Manning's regions.

	Manning's n-value		
Manning's region	**Main channel**	**Floodplains**	**Forest**
1	0.020	0.100	0.200
2	0.020	0.100	0.200
3	0.020	0.100	0.200
4	0.020	0.100	0.200
5	0.001	0.020	0.150
6	0.001	0.020	0.150
7	0.014	0.020	0.150

Figure 70 represents the outcomes of the simulation incorporating the recent modifications to the Manning's n-values in all calibration zones. The final adjustments made to the Manning's n-values in calibration zone 5 led to a reduction in correctly predicted flooded areas to 4.03 km^2, a decrease to 0.58 km^2 in over-predicted areas, and the under-predicted areas was unchanged at 0.23 km^2. As a result, there was an improvement in the measure of fit values, with F^1 increasing to 0.83 and F^2 increasing to 0.71.

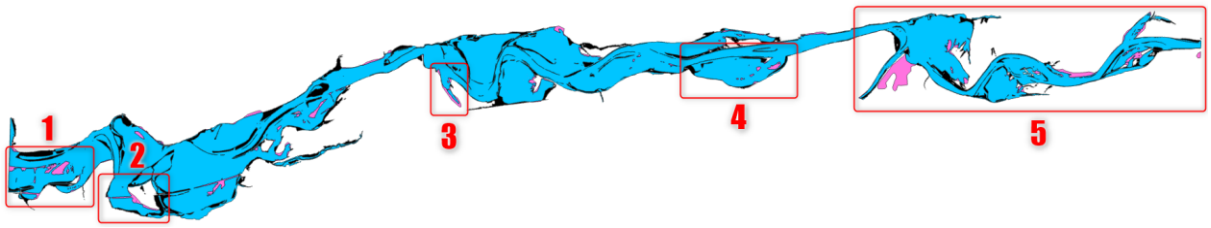

Figure 70: Storm Gyda flood event simulated using new Manning's n-values for all calibration zones, overlayed the flood delineation map derived from COSMO-SkyMed SAR image merged with the SR16 map. The colors represent the following: blue for correctly predicted areas, black for over-predicted areas, and pink for under-predicted areas.

The difference in flooded areas before and after changing the Manning's n-values for the main channel inside calibration zones 5 is illustrated in Figure 71.

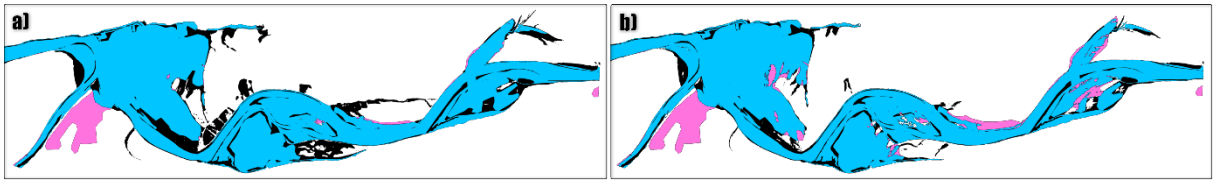

Figure 71: Calibration zone 5 before (a) and after (b) changing the Manning's n-values for the main channel in the Manning's regions 5-7. Blue is correctly predicted, black is over-predicted and pink is under-predicted.

The regionalized calibration of the Storm Gyda flood event involved merging the forest resource map SR16 with the flood delineation map from the SAR image captured by the COSMO-SkyMed satellite during Storm Gyda for comparing overlay areas and assessing the measure of fit values. To evaluate the performance of the model without the integration of the SR16 map, the modelling results were compared using only the flood delineation map. The initial results obtained using the best Manning's n-values of 0.02 for the main channel and floodplains showed measure of fit values of 0.68 for F^1 and 0.41 for F^2. The correctly predicted area was 3.37 km^2, the over-predicted area was 1.33 km^2, and the under-predicted area was 0.23 km^2.

After performing the regionalized calibration with the updated Manning's n-values from Table 12 in the calibration zones and comparing the modelling results to the flood delineation map from the SAR image, there was an improvement in the measure of fit values. The F^1 value increased to 0.70, and the F^2 value increased to 0.44. The correctly predicted area remained unchanged at 3.37 km^2, the over-predicted area decreased to 1.24 km^2, while the under-predicted area remained the same at 0.23 km^2, illustrated in Figure 72.

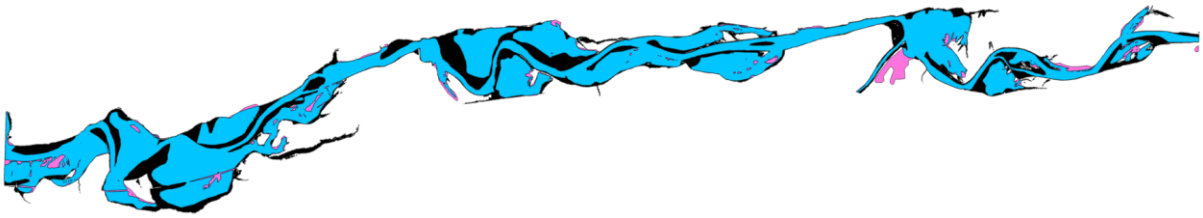

Figure 72: Storm Gyda flood event simulated using new Manning's n-values for all calibration zones, overlayed the flood delineation map derived from COSMO-SkyMed SAR image. The colors represent the following: blue for correctly predicted areas, black for over-predicted areas, and pink for under-predicted areas.

To summarize, Table 13 shows the measure of fit values F^1 and F^2 before and after the regionalized calibration.

Table 13: Measure of fit values before and after the regionalized calibration (RC), when comparing to the flood delineation map, and the flood delineation map + SR16 map.

	Flood delineation map		Flood delineation map + SR16	
Measure of fit	**Before RC**	**After RC**	**Before RC**	**After RC**
F^1	0.68	0.70	0.82	0.83
F^2	0.41	0.44	0.69	0.71

4.3.2 Validating the regionalized calibration of Storm Gyda flood event

The validation of the regionalized calibration of the Storm Gyda flood event that occurred January 13, 2022, is done using the Manning's n-values from Table 12 in the different Manning's regions, while keeping the rest Manning's n-values at reference levels. The regionalized calibration was validated against the flood events from:

- August 14, 2003
- November 26, 2016
- January 21, 2020
- January 13, 2021

The simulated flood inundation maps are overlayed the flood delineation maps from the respective floods simulated, resulting in the areas representing the correctly predicted

flood areas (blue), over-predicted flood areas (black), and under-predicted flood areas (pink), as depicted in Figure 73.

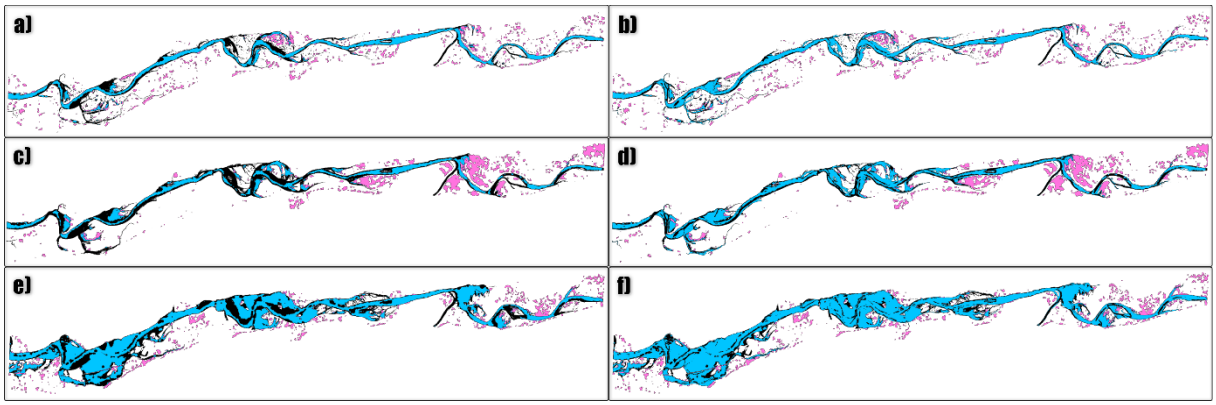

Figure 73: Flood overlay plots used for validation of the regionalized calibration of the Storm Gyda, flood event. (a) Flood event, November 26, 2016. (b) Flood event, November 26, 2016, with merged SR16 map and SAR binary map. (c) Flood event, January 21, 2020. (d) Flood event, November January 21, 2020, with merged SR16 map and SAR binary map. SR16 map and SAR binary map. (e) Flood event, November 24, 2021. (f) Flood event, November 24, 2021, with merged SR16 map and SAR binary map. Blue: correctly predicted. Black: over-predicted. Pink: under-predicted.

Table 14 displays the measure of fit values, F^1 and F^2, derived from the validation of the regionalized calibration of the Storm Gyda flood event. The results are presented through a comparison of the simulated flood inundation maps with the flood delineation maps, as well as the flood inundation maps compared to the flood delineation maps merged with the forest resource map SR16.

Table 14: Flood events used in validation of the regionalized calibration of the Storm Gyda, flood event. F^1 and F^2 values presented both with and without SR16 map merged with flood delineation map.

	Flood delineation map		Flood delineation map + SR16	
Flood event	**F^1**	**F^2**	**F^1**	**F^2**
2016-11-26	0.39	0.06	0.52	0.32
2020-01-21	0.29	-0.13	0.45	0.18
2021-11-24	0.54	0.23	0.66	0.48

Moreover, the effectiveness of the regionalized calibration was further assessed by comparing the simulated water surface elevations with the observed water surface elevations recorded during the flood event on August 14, 2003. By utilizing the Manning's n-values derived from the regionalized calibration in the respective Manning's regions, the MAE and RMSE were calculated, resulting in values of 0.52 m and 0.61 m, respectively.

The disparities between the observed and simulated water surface elevations along each profile line are illustrated in Figure 74. It is noteworthy that, in general, the simulation tends to underestimate the water surface elevations along most profile lines, except for profile line 9 where an overestimation occurs. The differences are represented by negative values, indicating an overestimation in the simulated water surface elevations, while positive values indicate an underestimation.

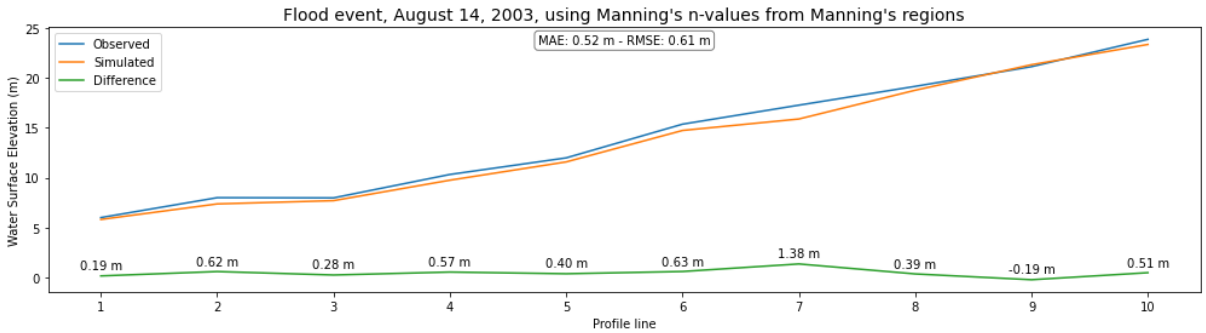

Figure 74: Plot of observed and simulated water surface elevations at each profile line, with a difference line showing the discrepancy, using the Manning's n-values from the Manning's regions from the regionalized calibration of the Storm Gyda flood event.

5 Discussions

5.1 Evaluation of flood event, August 14, 2003

5.1.1 Calibration of Manning's n-values

The findings from the calibration and fine-tuned calibration processes emphasize the value of using the same Manning's n-value for the entire main channel and floodplain in gaining insights into the range of Manning's n-values within the study area. This holistic approach enables a comprehensive understanding of the hydraulic behaviour and roughness characteristics across the entire system. By systematically exploring all possible combinations of Manning's n-values within a literature-based range, it became possible to determine the suitable ranges for these parameters.

Furthermore, the results indicate that the difference in the goodness of fit between the calibration and fine-tuned calibration was minimal. In the fine-tuned calibration, when a new parameter set was found, with Manning's n-values of 0.032 for the channel and 0.1 for floodplains, the RMSE remained unchanged, while the MAE exhibited a reduction of 0.1 m. RMSE, being sensitive to outliers, places more emphasis on extreme values. The lack of reduction in RMSE suggests that the significant deviations in the difference between observed and simulated water surface elevations have not been effectively addressed or improved. These findings suggest that the initial calibration process effectively captured the essential hydraulic properties and achieved a reasonable level of accuracy in simulating water surface elevations.

However, it is important to note that the fine-tuned calibration did have a slight impact on the overall difference in the simulated water surface elevations, as shown in Figure 75. Specifically, the fine-tuned calibration resulted in slightly higher water surface elevations, where positive values indicate the increase. This outcome aligns with expectations since a higher Manning's n-value implies greater resistance on the water surface, leading to higher water levels.

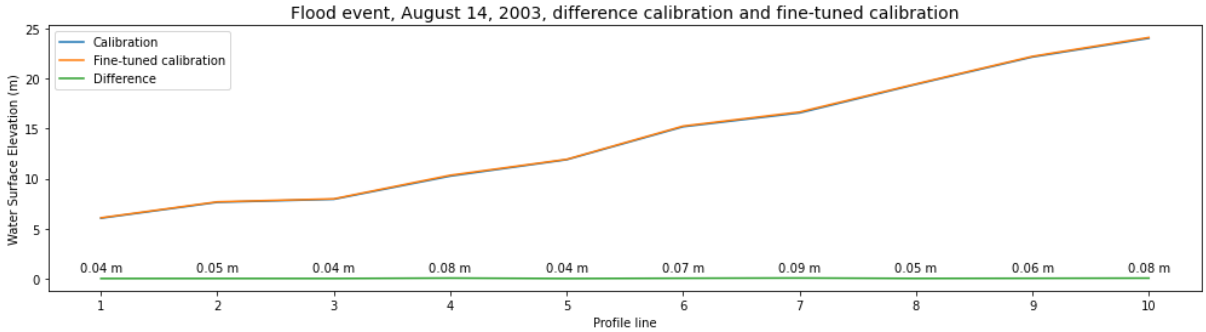

Figure 75: Difference in water surface elevations between calibration and fine-tuned calibration.

The observed and simulated water surface elevations had some significant deviations from both the calibration approaches, particularly in profile lines 2, 7, 8 and 9, as shown in Figure 42 and Figure 45, that can be influenced by various factors. One significant factor contributing to these deviations is the presence of uncertainties in the observed

data. Measurement errors or variations in data collection methods that can contribute to these deviations, such as limitations in measurement instruments (Biemer et al., 2013). Moreover, the specific location within the profile line where the measurements are taken can also impact the observed water surface elevation.

Additionally, the timing of the water surface elevation measurements can introduce further uncertainties. In the study area, where the river spans approximately 17.7 km, it may not be possible to measure water surface elevations at every location simultaneously, when the discharge is exactly 465 m3/s at the 112.27 Skjermo measuring station. This temporal mismatch between the discharge measurement and the collection of water surface elevations can lead to discrepancies between observed and simulated values. On top of that, further uncertainties can evolve from the calculated discharge in the ungauged tributaries that are represented in the model.

Furthermore, the natural variability of the river system itself can contribute to deviations between observed and simulated water surface elevations. Rivers are complex and dynamic systems influenced by various factors such as flow rates, sediment transport, channel morphology, and vegetation (Sun et al., 1996). The observed water surface elevations were collected in 2003, and the LiDAR used in the model were acquired in 2016. This timespan can introduce changes in the factors mentioned, that cannot be captured by the model, leading to differences in between the simulated and observed water surface elevations.

In addition to the uncertainties associated with the observed water surface elevations, deviations between observed and simulated values can also arise from other contributing factors. One such factor is the inherent variations in roughness that occur along the length of natural rivers (Bathurst, 1978), which are not accounted for when using a single Manning's n-value throughout the entire river.

The deviations observed between the observed and simulated water surface elevations can be attributed, at least in part, to these variations along the river. To address this, a regionalized calibration approach was employed to better align the simulated water surface elevations with observed data. This approach involved adjusting the Manning's n-values in specific regions in the river to improve the fit between observed and simulated values.

To achieve the best possible fit between observed and simulated water surface elevations, numerous iterations were performed, experimenting with different Manning's n-values and Manning's region sizes in an attempt to achieve a better performance of the model. After careful evaluation, the values mentioned in Table 9 were determined to yield the best outcome in terms of minimizing the deviations between observed and simulated water surface elevations. Unrealistic Manning's n-values were introduced in Manning's regions 3, 9, and 10, utilizing the values 0.018, 0.009, and 0.004, respectively. These values, that are not within the literature-based range, were specifically selected to optimize the alignment between the simulated and observed data in those particular regions, and further emphasizes the uncertainties in the observed water surface elevations. The observed and simulated water surface elevations exhibited minimal deviations in most profile lines, with deviations close to 0 m, as shown in Figure 48. However, profile lines 2 and 3 showed deviations of 0.07 m and -0.09 m, respectively. These were the optimal values that could be achieved in these profile lines. When attempting to minimize one, the other would increase, and vice versa. This necessitated finding the optimal balance between the two profile lines. Accepting this

deviation was necessary as there could be several factors influencing it, including measurement uncertainties as previously described, inaccuracies in representing the discharges within the river system, or hydraulic properties.

During the calibration process, the focus was to minimize the discrepancies between observed and simulated water surface elevations at specific profile lines. However, it is important to note that the dynamics occurring between these profile lines are not fully accounted for in this approach. This limitation becomes evident when comparing the flood inundation areas generated by the fine-tuned calibration (see Figure 51) and the regionalized calibration (see Figure 54).

The fine-tuned calibration resulted in a flood inundation area of 5.10 km^2, whereas the regional calibration produced a smaller area of 4.19 km^2. The difference of 0.91 km^2 represents a significant reduction in the flood inundation extent when employing the regionalized calibration approach. This finding highlights the importance of considering the spatial variability and local characteristics within the study area when calibrating hydraulic models.

5.1.2 Model sensitivity

The sensitivity of the model to changes in the Manning's n-value was evaluated for the three major land cover types: the main channel, floodplains, and forest. To further investigate this, simulations were done using the minimum and maximum Manning's n-values within the literature-based range. The objective was to assess the resulting impact on the simulation outcomes, specifically in terms of flooded area and changes in performance metrics. The findings from the model sensitivity analysis provided intriguing insights into the influence of different Manning's n-values on the performance of the model.

It was observed that changes in the Manning's n-values for the floodplains did not have a significant effect on the performance of the model when the Manning's n-values for the main channel were relatively low. However, as the Manning's n-values for the main channel increased, there were noticeable deviations between the MAE and RMSE for the minimum and maximum Manning's n-value for the floodplains. This suggests that the accuracy of the model is more sensitive to the Manning's n-values in the floodplains when higher Manning's n-values are applied to the main channel.

One possible explanation for this observation is that higher water surface elevations in the river, resulting from increased Manning's n-values in the main channel, lead to increased water flow into the floodplains. As a consequence, the floodplains Manning's n-values become more critical in determining the accuracy of the model, particularly when dealing with higher water surface elevations. Nonetheless, when using the optimal Manning's n-value of 0.032 for the main channel, the model exhibits marginal sensitivity to changing the Manning's n-value from 0.02 to 0.1 in the floodplains, even though the floodplains comprise the largest area (62 %).

On the other hand, when changing the Manning's n-value in the main channel between the minimum and maximum values, the model exhibits significant sensitivity. This can be attributed to the volume of water flowing through the river during flooding events. While a substantial amount of water may overflow the banks, there is still a considerable flow remaining within the river. A lower Manning's n-value results in less surface resistance, allowing for higher velocities and lower flows. Conversely, a higher Manning's n-value increases surface resistance, leading to lower velocities and higher flows.

The land cover type "forest" is of particular interest in terms of the Manning's n-value, as forests and vegetation often border the river and serve as the first point of contact when water overflows the banks. Therefore, a comprehensive sensitivity analysis was conducted on the Manning's n-value for the forest land cover, ranging from 0.1 to 0.2, which represents the typical range for the forest type within the study area. This analysis was performed while considering different Manning's n-values for the floodplains and utilizing the optimal Manning's n-value of 0.032 for the main channel.

The results of the analysis showed that the model did not exhibit significant sensitivity to the Manning's n-value for the forest land cover. This finding is consistent with earlier observations that the sensitivity of the model to different Manning's n-values in the floodplains is primarily influenced by the Manning's n-value used in the river (Horritt, 2006).

5.2 Evaluting the flood event, November 24, 2021

The flood event on November 24, 2021, was characterized by the highest discharge among all the Sentinel-1 images used in this study. Consequently, this event was chosen for a thorough calibration of the Manning's n-values for the main channel and floodplains, using the F^1 and F^2 measure of fit values to evaluate the performance of the model.

The optimal Manning's n-values obtained from the calibration process were determined to be 0.02 for both the main channel and the floodplains. When assessing the performance of the model using the F^1 measure of fit, which do not penalize for over-prediction, a value of 0.54 was obtained. This indicates reasonably good results for the chosen Manning's n-values, suggesting that the model performs well in terms of accurately predicting flooded areas. However, when evaluating the model using the F^2 measure of fit, which penalize for over-prediction, a value of 0.21 was obtained. This suggests that the model tends to overestimate the extent of flooded areas.

Indeed, the limitations of Sentinel-1 satellite imagery can contribute to the over-prediction observed in the modelling results. The SAR imagery may not provide the necessary level of detail to accurately delineate all flooded areas, leading to some areas being misinterpreted as flooded when they are not. This can result in an overestimation of the extent of flooding.

The subjective nature of the threshold method used for flood delineation is another factor that can contribute to over-prediction. Setting the threshold value involves a degree of subjectivity, and different individuals may interpret the flooded areas differently. Exploring alternative flood delineation methods that are less subjective and more robust can help improve the accuracy of flood extent delineation and reduce over-prediction.

The consistent prediction of flooding in forest areas by the model throughout the calibration and validation processes may also contribute to the over-prediction. Forested areas, especially those located near rivers, can hinder the ability of the satellite to capture images of potential water beneath the vegetation (Horritt et al., 2003). As a result, this limitation introduces a disparity between the modelled flood extent and the observed flood extent in SAR images. Consequently, this disparity can contribute to an overestimation of the flood extent by the model.

When calibrating the model against the flood delineated SAR image, it became evident that the model is most sensitive to changes in the Manning's n-value in the main channel, similar to the calibration of the August 14, 2003, flood event against observed water surface elevations. However, there was not a significant difference in the measure

of fit when varying the Manning's n-value in the floodplains at each increment of Manning's n-value in the main channel.

Interestingly, the model also produced reasonable results for the F^1 measure of fit when using a Manning's n-value of 0.3 for the main channel, which aligns with the findings from the calibration of the August 14, 2003, flood event. According to (Barnes, 1967), Manning's n-values in the main channel can range from 0.024 to 0.075, which corresponds with the findings in the calibration approaches. However, there are instances of unrealistic outliers observed during the regionalized calibration processes. These outliers can be attributed to specific hydraulic properties inherent in the model, which hinder the effective utilization of realistic Manning's n-values. Nonetheless, utilizing high-resolution LiDAR to represent the bathymetry in the river enables the establishment of a clear contextual understanding of the Manning's n-values in the main channel.

This implication suggests that the calibration process can be streamlined, as the regionalized calibration required minimal adjustments once the optimal uniform Manning's n-value was determined for the entire main channel. This finding highlights the potential to achieve an optimal goodness of fit with fewer calibration iterations when applying bathymetric LiDAR data.

Furthermore, the necessity for employing unrealistic Manning's n-values to achieve satisfactory calibration results is very minimal. This suggests that the integration of bathymetric LiDAR data can mitigate the requirement for such unrealistic values, which may otherwise compromise the calibration when validating it against other flood events.

One advantage of calibrating against SAR imagery is the ability to visually inspect the model results against the flood delineation map. Figure 60 highlights areas of over-prediction (black areas) and under-predicted (pink areas) when using the optimal Manning's n-values, which compromises the results in both the F^1 and F^2 values. Refining the flood delineation map and reducing these areas would possibly lead to an improvement in the F-values.

Additionally, when visually inspecting the model it exhibits an over-prediction in the upper part of the river, indicating that the Manning's n-values for the main channel in this section may not fall within the literature-based range of 0.02 to 0.1. The calibration of the August 14, 2003, flood event also revealed an over-prediction in these areas, suggesting the need for lower Manning's n-values than those suggested by the literature to compensate for this discrepancy.

To address the over-prediction of flooded areas, the forest resource map SR16 was incorporated and merged with the flood delineated map derived from the SAR imagery. This integration aimed to compensate for the areas that were not captured by the SAR images due to the presence of dense vegetation. By including these potential flooded areas, the impact on the performance of the model, as measured by the F^1 and F^2 values, was observed.

When utilizing the optimal Manning's n-values, it was observed that the F^1 value increased by 0.13, indicating a greater agreement between the predicted flood extent of the model and the merged map incorporating the forest resource data. The F^2 value also exhibited a significant increase of 0.25, indicating a reduction in the over-prediction area, subsequently leading to less penalization of the performance.

It is important to acknowledge that uncertainties exist regarding the presence of water in every area of the forest within the flooded regions. However, upon analysing the satellite images, it is highly plausible that these forested areas are indeed flooded as shown in Figure 17. This highlights the significance of incorporating potential flooded areas when

calibrating the model, as it can have a substantial impact on the performance metrics. The significant increase in the F^2 value can be attributed to the reduction in over-prediction area, while the smaller increase in the F^1 value is due to the improvement in correctly identifying flooded areas, which also benefits the F^2 metric.

5.3 Evaluating the flood event, January 14, 2022 (Storm Gyda)

The vector data representing the flooded areas during Storm Gyda on January 14, 2022, acquired from the post-flood event EMSR product, was utilized for a regionalized calibration of the model. The best measure of fit Manning's n-values obtained from the calibration of the November 24, 2021, flood event served as the base for the regionalized calibration, as these Manning's n-values also provided the best measure of fit for the Storm Gyda event.

The regionalized calibration started with assessing the local influence of the Manning's n-value on floodplains by adjusting the Manning's n-value for floodplains and forest within specific regions. The calibration process involved dividing the study area into different calibration zones and making specific adjustments to the Manning's n-values within each Manning's region inside the zones. Previous calibrations had shown minimal sensitivity to changing the Manning's n-value for the floodplains and forests for the entire system. By adopting a regional calibration approach, it was possible to visually interpret and analyse the local changes in the flooded area.

Although some changes were observed in the different zones depicted in Figure 69, the adjustments made to the Manning's n-values within these regions, ranging from the lowest to the highest value within the literature-based range, did not have a significant influence on the performance of the model, as reflected by the measure of fit values F^1 and F^2. However, there was a noticeable increase of 0.04 km^2 in the correctly predicted areas, a 0.02 km^2 increase in the over-predicted areas, and a 0.04 km^2 decrease in the under-predicted areas. This indicates an improvement in the performance of the model, albeit not substantial enough to influence the measure of fit values.

The upper region of the study area, which was designated as calibration zone 5, exhibited a significant amount of over-prediction. Since the Manning's n-values for the floodplains and forest already were within the lower and mid-range, it was hypothesized that reducing the flow in the river by adjusting the Manning's n-values in the main channel would help mitigate the over-prediction. Therefore, calibration zone 5 was divided into three Manning's regions, and through a trial-and-error process, suitable Manning's n-values were identified for each region. In order to address the over-prediction, Manning's n-values were chosen that fell outside the literature-based range, similar to the regionalized calibration of the flood event from August 14, 2003.

This suggests that there might be a factor in the model that leads to significant over-prediction in this specific area, when using Manning's n-values within the desired range. It also highlights the potential need for adjustments of Manning's n-values outside the literature-based range during calibration events to achieve the desired results and improve the performance of the model.

Figure 71 shows the results of the of using the calibrated Manning's n-values for the main channel in zone 5. The Manning's n-values did have a noticeable impact on the measure of fit values. The F^1 value increased to 0.83, and the F^2 value increased to 0.71.

As a result of the regionalized calibration, there were slight changes in the areas. The correctly predicted areas decreased by 0.01 km^2, the over-predicted areas decreased by 0.08 km^2, and the under-predicted areas remained the same. This explains why the most significant improvement was observed in the F^2 value, as the over-predicted areas is used to penalize the model in this measure, where the most decrease was observed. It further demonstrates that the Manning's n-value for the main channel has the greatest impact on the performance of the model, as earlier calibrations also have exhibited. Overall, the regionalized calibration approach, including adjustments to the Manning's n-values in the main channel, led to improved performance in the model, particularly in reducing over-prediction.

In summary, it is possible to consider that implementing more Manning's regions for the floodplains could enhance the performance of the model. However, it remains uncertain whether the benefits gained from the additional work required for a regional calibration approach, focused on locally influencing the floodplains, would be substantial enough to justify its implementation. Considering the overall low sensitivity of the floodplains, a careful assessment is necessary to determine if the potential benefits outweigh the additional calibration work involved. Given that adjusting the Manning's n-value in the main channel has demonstrated the most significant impact on the performance of the model, it may be advisable to adopt a regionalized calibration approach with separate Manning's regions for the entire main channel, similar to what was done in regionalized calibration of the August 14, 2003, flood event.

5.4 Validating the calibrated models

A fundamental requirement for all calibrations performed on 2D hydraulic models, is that they need some form of validation to confirm and give confidence in the calibration results. Therefore, all the different calibration event was validated against the available observed water surface elevations, SAR imagery and vector data from the EMSR product that was derived from SAR imagery. In doing so, the point was to see if there were any connection between the calibration processes and how they responded individually to the validation data.

Table 15 provides an overview of the flood events that were subjected to various calibration approaches and subsequently validated against SAR imagery. Upon evaluating the model performance, it becomes apparent that the measure of fit values obtained from the validation against SAR imagery for the November 26, 2016, and January 21, 2020, flood events do not yield satisfactory results. The presence of negative values suggests an over-prediction by the model, indicating that the calibration might not be optimal or that the flood delineation from the SAR image does not accurately capture the flooded areas.

Specifically, the models calibrated against observed water surface elevations tend to exhibit a tendency for the largest over-predictions compared to the other calibration approaches, which could be attributed to the use of high Manning's n-values in the main channel.

An additional important observation when analysing the flood delineation from SAR images is the presence of under-predicted areas located far from the river and floodplains. These areas can be attributed to wet patches created by rainfall or instances where the river has receded, leaving wet spots on the ground. The satellite detects these wet areas, leading to their identification as wet pixels in the threshold method. Consequently, the under-prediction of flood extents is influenced by these falsely detected wet pixels, introducing inaccuracies in the performance of the model.

Regarding the January 21, 2020, flood event, it is interesting to note that a significant number of flooded areas in the upper parts of the study area were identified, despite the low discharge recorded when the SAR image was acquired. This observation suggests the presence of obstructions in the river, potentially in the form of ice accumulation, which can cause water to accumulate and result in additional flooded areas. These obstructions likely contribute to the lower performance of the model in accurately predicting the flood extent.

Furthermore, it is important to consider that these flood events have relatively low flows at image acquisition compared to the November 24, 2021, and January 13, 2022, flood events. As a result, the flooded areas might not be adequately captured by satellites due to their relatively large resolution. The low flow conditions may lead to smaller inundated areas that are not easily distinguishable at the resolution of the SAR imagery.

It is important to acknowledge these limitations when interpreting the results, as they can have a significant impact on the accuracy and performance of the model during calibration and validation against SAR imagery.

The November 24, 2021, and January 13, 2022, flood events, on the other hand, had SAR imagery that were captured at very high flow conditions in the river. The COSMO-SkyMed program captured the Storm Gyda flood event at 657 m^3/s, where the flood peaked at 692 m^3/s. This occurrence is indeed remarkable, as capturing one of the largest measured floods the river has experienced on a satellite image coinciding with the river being nearly at its peak is quite fortuitous. Such a coincidence provides a unique opportunity to study and analyse the flood event in detail, allowing for a more comprehensive understanding of its characteristics and impacts. The November 24, 2021, flood event exhibited a peak discharge of 583 m^3/s, while the satellite image was captured at a slightly lower discharge of 420 m^3/s.

The validation results against the November 24, 2021, flood event demonstrate improved measure of fit values when using the fine-tuned and rationalized calibration of the August 14, 2003, flood event, as well as the regionalized calibration of the flood event from Storm Gyda on January 13, 2022.

The F^1 value for all the approaches is relatively similar, but the Storm Gyda event exhibits the best measure of fit with a value of 0.54. This can be explained by the fact that when the model over-predicts the flood extent significantly, it may still capture the correctly flooded areas visible in satellite imagery.

However, the significant difference is evident in the F^2 value, where there is a notable deviation between the calibration based on observed water surface elevations and the Storm Gyda regionalized calibration based on SAR imagery. This discrepancy can be attributed to the regionalized calibration approach, which effectively addresses over-predictions by locally adjusting the flood extent in specific regions where the model tends to overestimate. By fine-tuning the flood extent in these areas, the model achieves a closer match with the actual flood extent, resulting in improved accuracy. Simultaneously, the rest of the model benefits from utilizing optimal Manning's n-values, ensuring accurate predictions for other areas. As a result, the regionalized calibration approach exhibits a better F^2 measure with reduced penalization, indicating enhanced performance in capturing the actual flood extent.

Furthermore, it is intriguing to note that none of the calibration approaches exhibit negative values in the F^2 measure of fit. This suggests that calibrating against SAR imagery, particularly during larger flood events, offers advantages in terms of accuracy.

The flood event from Storm Gyda on January 13, 2022, provides pre-processed vector data containing the delineation of the flooded areas from SAR imagery captured by the COMSO-SkyMed program. It is worth noting that this data has undergone algorithmic processing to identify and delineate the flooded areas. Interestingly, this delineation specifically removes flood areas that are located away from the river and floodplains. In contrast, SAR images used from the Sentinel-1 program, which utilized the threshold method for flood delineation, included these areas in their flood extent representations.

The analysis of the results from the validation against the Storm Gyda flood event clearly demonstrates a significantly improved measure of fit. This highlights the importance of pre-processing the flood delineation products derived from SAR imagery, as it has a substantial impact on the measure of fit results.

In terms of the F^1 values obtained from the different calibration approaches, they exhibit values close to each other. However, the calibration performed for the November 24, 2021, flood event stands out as the best, yielding a measure of fit F^1 value of 0.68. This calibration approach involves using the optimal Manning's n-value consistently across the entire river and floodplains, without local adjustments.

This distinction is further evident in the F^2 values, where the calibration approach used for the November 24, 2021, flood event exhibits significantly less over-prediction compared to the regionalized calibration of the August 14, 2003, flood event, which was calibrated against observed water surface elevations.

From these results, it is clear that although the regionalized calibration showed excellent performance in terms of MAE and RMSE, with values close to 0, this does not necessarily translate to better results when validating against SAR imagery. In contrast, the calibration approach specifically tailored to SAR imagery demonstrates very good performance in capturing the actual flood extent.

Overall, when analysing the results, the flood events that are calibrated against SAR imagery demonstrate the most promising outcomes when validated against other flood events captured by satellites.

Table 15: Calibrated flood events validated against flood delineation maps from SAR imagery acquired from satellite programs.

Calibrated flood event	2016-11-26		2020-01-21		2021-11-24		2022-01-13	
	F^1	F^2	F^1	F^2	F^1	F^2	F^1	F^2
2003-08-14 Fine-tuned calibration	0.34	-0.16	0.29	-0.25	0.50	0.10	0.66	0.34
2003-08-14 Regionalized calibration	0.36	-0.13	0.30	-0.21	0.49	0.07	0.63	0.27
2021-11-24 Calibration	0.40	0.05	0.29	-0.14	-	-	0.68	0.41
2022-01-13 Regionalized calibration	0.39	0.06	0.29	-0.13	0.54	0.23	-	-

One common observation in the study is the presence of non-wet areas between the river and the floodplains in the flood delineation maps obtained from both the Sentinel-1 program and the COSMO-SkyMed program. Upon visual interpretation of the simulated flooding areas from the flood events, it was observed that these areas were indeed flooded, aligning with forested areas according to the SR16 forest resource map. This

suggests that the SAR imagery from satellites is unable to detect the flooded regions beneath the forest canopy. Consequently, the models exhibit higher levels of over-prediction, which in turn affects the measure of fit values. To explore this observation, the SR16 forest map was merged into the flood delineation maps, and the resulting measure of fit values are presented in Table 16.

It is worth highlighting that all the measure of fit values experienced a significant increase after incorporating the forest areas into the calibration and validation process. This highlights the substantial impact of neglecting the presence of forested regions when calibrating against SAR imagery. In the worst-case scenario, if the objective of calibration is to accurately represent the flooding by ensuring that the model does not falsely classify wet spots as dry, the calibration would be severely erroneous without considering the forested areas. This emphasizes the critical importance of accounting for the presence of such areas in the calibration process to ensure accurate and reliable flood predictions.

However, it is important to acknowledge the presence of uncertainties in this approach. It is impossible to assert with absolute certainty that these areas are flooded without conducting ground observations or having direct measurements. However, in the context of this study, where all simulated events consistently showed these areas as flooded and considering the plausibility based on the observed patterns, it is highly likely that these areas are indeed affected by flooding. While uncertainties exist, the evidence gathered in this study supports the notion that these areas are prone to flooding.

Table 16: Calibrated flood events validated against SR16 forest resource map merged with flood delineation maps from SAR imagery acquired from satellite programs.

Calibrated flood event	2016-11-26		2020-01-21		2021-11-24		2022-01-13	
	F^1	F^2	F^1	F^2	F^1	F^2	F^1	F^2
2003-08-14 Fine-tuned calibration	0.50	0.15	0.45	0.07	0.62	0.34	0.79	0.60
2003-08-14 Regionalized calibration	0.53	0.22	0.47	0.14	0.61	0.31	0.75	0.52
2021-11-24 Calibration	0.54	0.33	0.46	0.20	-	-	0.82	0.69
2022-01-13 Regionalized calibration	0.52	0.32	0.45	0.18	0.66	0.48	-	-

The results of the various calibration events using the optimal Manning's n-values when comparing against observed water surface elevations are presented in Table 17. It is interesting to note that the models calibrated against SAR imagery for the November 24, 2021, and January 13, 2022, flood events exhibit larger deviations in the performance metrics, specifically MAE and RMSE. This can be attributed to the differences in the calibration procedures employed. The August 14, 2003, calibration was based on observed water surface elevations, aiming to minimize the disparity between observed and simulated values. In contrast, when calibrating against SAR imagery, there is no direct information about water surface elevations available, and the calibration is focused solely on matching the flood extent. Consequently, the simulated water surface elevations derived from SAR imagery calibrated models may not correspond as accurately to specific points in the model. However, as observed during the validation of the various calibration events against SAR imagery, calibrating the model using SAR imagery can still lead to an improvement in overall model performance.

Indeed, it is worth highlighting that calibrating against SAR imagery resulted in a smaller difference between the MAE and RMSE values, indicating a reduced presence of outliers compared to the fine-tuned calibration approach. Consequently, calibrating against SAR imagery holds the potential for achieving an overall better balance in the calibrated model.

Table 17: Calibration of flood events using best goodness of fit Manning's n-values compared to observed water surface elevations in the profile lines.

Calibrated flood event	MAE	RMSE
2003-08-14 Fine-tuned calibration	0.28	0.43
2003-08-14 Regionalized calibration	0.02	0.04
2021-11-24 Calibration	0.49	0.59
2022-01-13 Regionalized calibration	0.52	0.61

6 Conclusions and further work

This study aimed to calibrate and validate 2D hydraulic models that utilize high-resolution LiDAR data to represent the terrain and the river's bathymetry. Through a meticulous and comprehensive calibration process involving various flood events, incorporating different types of calibration data, the results highlight the significant influence of Manning's n-values for the main channel. Notably, the regionalized calibration approaches focusing on the Manning's n-value in the main channel exhibited superior model performance.

Interestingly, the study revealed that achieving optimal results in the regionalized calibration sometimes necessitated the introduction of Manning's n-values that fell outside the range defined in existing literature. This highlights the importance of considering unconventional values to accurately capture the complex hydraulic behaviour of the system. However, with the integration of bathymetric LiDAR data, the reliance on these unrealistic values was very minimal. The findings indicated that the Manning's n-values for the main channel largely fell within literature-based ranges. These findings suggest that utilizing bathymetric LiDAR data to represent the river can reduce the calibration requirements by facilitating the identification of appropriate Manning's n-values. Furthermore, employing realistic Manning's n-values in the calibration yields greater confidence in the model when validating against other flood events.

Additionally, through a sensitivity analysis of the boundary conditions it became very clear that some of the boundary conditions have significant impact on the modelling results. This underscores the importance of carefully considering boundary conditions during the development of flood inundation models.

The SAR imagery derived from the Sentinel-1 mission has demonstrated its usefulness in calibration and validation processes. Nevertheless, the findings suggest that the effectiveness of SAR images in representing floods may be influenced by the size of the flood event. The threshold technique applied for flood delineation in the study yielded satisfactory results. However, it was observed that this approach did not consider flood forest areas, leading to a diminished performance in the measure of fit values due to over-prediction. Moreover, the technique resulted in numerous flooded areas located far from the river and floodplains, resulting in under-prediction. To address these limitations, the study merged the flooded forest areas with the flood delineation maps, which greatly enhanced the measure of fit values in all calibration and validation results. These findings emphasize the necessity for additional refinement in the processing of SAR imagery to potentially enhance the accuracy when utilizing them in the calibration and validation of flood inundation models.

The utilization of flood delineation vector data from the Rapid Mapping product provided by the Copernicus Emergency Management Service proved to be highly beneficial in the calibration and validation processes. This positive outcome calls for further utilization of similar products and emphasizes the importance of activating such services before significant flooding events. By capturing valuable data that can be used to aid in the development of flood hazard maps, these services can greatly enhance flood risk management and preparedness efforts.

Based on the findings of this study, there are several interesting areas for further investigation. Firstly, exploring and comparing different flood delineation techniques for deriving flooded areas in SAR images could shed light on their impact on the performance of calibration approaches. This could involve testing alternative thresholding techniques or even exploring advanced machine learning algorithms for more accurate flood delineation.

Additionally, studying other river reaches and investigating whether there is a correlation between the optimal Manning's values derived from this study and those obtained in different study locations would provide valuable insights. It would help to understand if the Manning's values derived from one specific location can be generalized or if they are influenced by the characteristics of the river reach under investigation.

By conducting further research in these areas, we can improve our understanding of flood modelling and calibration approaches, leading to enhanced accuracy and performance in predicting and managing flood events.

References

3. Flaum—Direktoratet for byggkvalitet. (n.d.). Retrieved 17 June 2023, from https://dibk.no/saksbehandling-tilsyn-og-kontroll/utbygging-i-fareomrade-n/3.-flaum

Abdalla, E. M. H. (2019). *Evaluating approaches to estimate runoff from small ungauged catchments in Norway* [Master Thesis]. Technische Universität Dresden.

Abily, M., Bertrand, N., Delestre, O., Gourbesville, P., & Duluc, C.-M. (2016). Spatial Global Sensitivity Analysis of High Resolution classified topographic data use in 2D urban flood modelling. *Environmental Modelling & Software*, *77*, 183–195.

Ahlstrøm, A. P., Bjørkelo, K., & Fadnes, K. (2019). AR5 Klassifikasjonssystem. Klassifisering av arealressurser. *NIBIO BOK*.

Alfredsen, K. (2022). *Oversikt over bruk av batymetrisk LiDAR ved NTNU*.

Apel, H., Aronica, G., Kreibich, H., & Thieken, A. (2009). Flood risk analyses—How detailed do we need to be? *Natural Hazards*, *49*(1), 79–98.

Arcement, G. J., & Schneider, V. R. (1989). *Guide for selecting Manning's roughness coefficients for natural channels and flood plains*.

Aronica, G., Hankin, B., & Beven, K. (1998). Uncertainty and equifinality in calibrating distributed roughness coefficients in a flood propagation model with limited data. *Advances in Water Resources*, *22*(4), 349–365.

Awadallah, M. O. M., Juárez, A., & Alfredsen, K. (2022). Comparison between Topographic and Bathymetric LiDAR Terrain Models in Flood Inundation Estimations. *Remote Sensing*, *14*(1), 227.

Bævre, I., & Øydvin, E. K. (2007). *Flomsonekart, Delprosjekt Surna* (Flomsonekart No. 10/2007). Norges vassdrags- og energidirektorat.

Barnes, H. H. (1967). *Roughness characteristics of natural channels*. US Government Printing Office.

Bates, P. D. (2022). Flood Inundation Prediction. *Annual Review of Fluid Mechanics*, *54*(1), 287–315. https://doi.org/10.1146/annurev-fluid-030121-113138

Bates, P. D., & De Roo, A. (2000). A simple raster-based model for flood inundation simulation. *Journal of Hydrology*, *236*(1–2), 54–77.

Bates, P. D., Horritt, M. S., Aronica, G., & Beven, K. (2004). Bayesian updating of flood inundation likelihoods conditioned on flood extent data. *Hydrological Processes*, *18*(17), 3347–3370.

Bates, P. D., Wilson, M. D., Horritt, M. S., Mason, D. C., Holden, N., & Currie, A. (2006). Reach scale floodplain inundation dynamics observed using airborne synthetic aperture radar imagery: Data analysis and modelling. *Journal of Hydrology*, *328*(1–2), 306–318.

Bates, P., Horritt, M., Smith, C., & Mason, D. (1997). Integrating remote sensing observations of flood hydrology and hydraulic modelling. *Hydrological Processes*, *11*(14), 1777–1795.

Bathurst, J. C. (1978). Flow resistance of large-scale roughness. *Journal of the Hydraulics Division*, *104*(12), 1587–1603.

Beven, K. (2011). 14 Distributed Models and Uncertainty in Flood Risk Management. *Flood Risk Science and Management*, 291.

Beven, K., Lamb, R., Leedal, D., & Hunter, N. (2015). Communicating uncertainty in flood inundation mapping: A case study. *International Journal of River Basin Management*, *13*(3), 285–295.

Biemer, P. P., Groves, R. M., Lyberg, L. E., Mathiowetz, N. A., & Sudman, S. (2013). *Measurement errors in surveys* (Vol. 548). John Wiley & Sons.

Blöschl, G., Kiss, A., Viglione, A., Barriendos, M., Böhm, O., Brázdil, R., Coeur, D., Demarée, G., Llasat, M. C., Macdonald, N., & others. (2020). Current European flood-rich period exceptional compared with past 500 years. *Nature*, *583*(7817), 560–566.

Borah, S. B., Sivasankar, T., Ramya, M., & Raju, P. (2018). Flood inundation mapping and monitoring in Kaziranga National Park, Assam using Sentinel-1 SAR data. *Environmental Monitoring and Assessment*, *190*, 1–11.

Breili, K., Simpson, M. J. R., Klokkervold, E., & Roaldsdotter Ravndal, O. (2020). High-accuracy coastal flood mapping for Norway using lidar data. *Natural Hazards and Earth System Sciences*, *20*(2), 673–694.

Brunner, G., Savant, G., & Heath, R. E. (2020). *Modeler Application Guidance for Steady vs Unsteady, and 1D vs 2D vs 3D Hydraulic Modeling* (TD-41). U.S. Army Corps of Engineers.

Brunner, G. W. (2016). *HEC-RAS, River Analysis System Hydraulic Reference Manual* (Version 5.0). U.S. Army Corps of Engineers.

Brunner, G. W. (2023). *HEC-RAS River Analysis System HEC-RAS 2D User's Manual* (Version 6.3). U.S. Army Corps of Engineers.

Brunner, G. W., Ackerman, C. T., & Goodell, C. R. (2023). *HEC-RAS, River Analysis System HEC-RAS User's Manual* (Version 6.3). U.S. Army Corps of Engineers.

Carreño Conde, F., & De Mata Muñoz, M. (2019). Flood monitoring based on the study of Sentinel-1 SAR images: The Ebro River case study. *Water*, *11*(12), 2454.

Carter, R. W., & Anderson, I. E. (1963). Accuracy of current meter measurements. *Journal of the Hydraulics Division*, *89*(4), 105–115.

Casas, A., Benito, G., Thorndycraft, V., & Rico, M. (2006). The topographic data source of digital terrain models as a key element in the accuracy of hydraulic flood modelling. *Earth Surface Processes and Landforms: The Journal of the British Geomorphological Research Group*, *31*(4), 444–456.

Casulli, V. (2009). A high-resolution wetting and drying algorithm for free-surface hydrodynamics. *International Journal for Numerical Methods in Fluids*, *60*(4), 391–408.

Chapman, B., McDonald, K., Shimada, M., Rosenqvist, A., Schroeder, R., & Hess, L. (2015). Mapping regional inundation with spaceborne L-Band SAR. *Remote Sensing*, *7*(5), 5440–5470.

Chaulagain, S. (2018). *An investigation into remote sensing techniques for describing hydraulic roughness*.

Chow, V. T., Maidment, D. R., & Mays, L. W. (1988). *Applied Hydrology*. McGraw-Hill Book Company.

Cook, A., & Merwade, V. (2009). Effect of topographic data, geometric configuration and modeling approach on flood inundation mapping. *Journal of Hydrology*, *377*(1–2), 131–142.

Dhillon, D. S., Bombardelli, F. A., Fleenor, Wm. E., & Zamani, K. (2014). *On the issues associated with 2-D modeling for flood mapping purposes*.

Di Baldassarre, G., Schumann, G., & Bates, P. D. (2009). A technique for the calibration of hydraulic models using uncertain satellite observations of flood extent. *Journal of Hydrology*, *367*(3–4), 276–282.

Dong, P., & Chen, Q. (2017). *LiDAR Remote Sensing and Applications* (1st edition). CRC Press. https://doi.org/10.4324/9781351233354

Dowman, I. (2004). Integration of LiDAR and IFSAR for mapping. *International Archives of Photogrammetry and Remote Sensing*, *35*.

Ecosystem | Copernicus Data Space Ecosystem. (n.d.). Retrieved 9 June 2023, from https://dataspace.copernicus.eu/ecosystem

Eikenæs, O., Bakkan, M., Berg, H., & Roald, C. M. (2020). *Plan for flomfarekartlegging 2021-2025* (Nr. 33/2020). Norges vassdrags- og energidirektorat.

Elkhrachy, I., Pham, Q. B., Costache, R., Mohajane, M., Rahman, K. U., Shahabi, H., Linh, N. T. T., & Anh, D. T. (2021). Sentinel-1 remote sensing data and Hydrologic Engineering Centres River Analysis System two-dimensional integration for flash flood detection and modelling in New Cairo City, Egypt. *Journal of Flood Risk Management*, *14*(2), e12692.

Ervine, D., Baird, J., Noutsopoulos, G., Hadjipanos, P., Bulman, R., & Holland, P. (1982). Rating curves for rivers with overbank flow. *Proceedings of the Institution of Civil Engineers*, *73*(4), 849–855.

ESA - Mission ends for Copernicus Sentinel-1B satellite. (n.d.). Retrieved 14 June 2023, from https://www.esa.int/Applications/Observing_the_Earth/Copernicus/Sentinel-1/Mission_ends_for_Copernicus_Sentinel-1B_satellite

Ezzine, A., Saidi, S., Hermassi, T., Kammessi, I., Darragi, F., & Rajhi, H. (2020). Flood mapping using hydraulic modeling and Sentinel-1 image: Case study of Medjerda Basin, northern Tunisia. *The Egyptian Journal of Remote Sensing and Space Science*, *23*(3), 303–310.

Faruolo, M., Coviello, I., Lacava, T., Pergola, N., & Tramutoli, V. (2009). Real Time Monitoring of flooded areas by a multi-temporal analysis of optical satellite data. *2009 IEEE International Geoscience and Remote Sensing Symposium*, *4*, IV–192.

Faulkner, D., Kjeldsen, T., Packman, J., & Stewart, L. (2012). *Estimating flood peaks and hydrographs for small catchments: Phase 1*.

Fergus, T., Hoseth, K., & Sæterbø, E. (2010). Vassdragshåndboka: Håndbok i vassdragsteknikk. *Ny Rev. Utg. Trondheim: Tapir Akademisk Forl*.

Fewtrell, T. J., Neal, J. C., Bates, P. D., & Harrison, P. J. (2011). Geometric and structural river channel complexity and the prediction of urban inundation. *Hydrological Processes*, *25*(20), 3173–3186.

Fieberg, J., & Jenkins, K. J. (2005). Assessing uncertainty in ecological systems using global sensitivity analyses: A case example of simulated wolf reintroduction effects on elk. *Ecological Modelling*, *187*(2–3), 259–280.

Filipponi, F. (2019). Sentinel-1 GRD preprocessing workflow. *International Electronic Conference on Remote Sensing*, 11.

Fleig, A. K., & Wilson, D. (2013). *Flood estimation in small catchments*.

Gabrielsen, S.-E., Skår, B., Stranzl, S. F., & Lehmann, G. B. (2017). Kartlegging av gyte- og oppvekstområder for laks i Surna høsten 2016. *LFI Uni Miljø*.

Gioia, G., & Bombardelli, F. (2001). Scaling and similarity in rough channel flows. *Physical Review Letters*, *88*(1), 014501.

Gobeyn, S., Van Wesemael, A., Neal, J., Lievens, H., Van Eerdenbrugh, K., De Vleeschouwer, N., Vernieuwe, H., Schumann, G. J.-P., Di Baldassarre, G., De

Baets, B., & others. (2017). Impact of the timing of a SAR image acquisition on the calibration of a flood inundation model. *Advances in Water Resources*, *100*, 126–138.

González-Sanchis, M., Murillo, J., Latorre, B., Comín, F., García-Navarro, P., & others. (2012). Transient two-dimensional simulation of real flood events in a Mediterranean floodplain. *Journal of Hydraulic Engineering*, *138*(7), 629–641.

Goodell, C. R. (2010, January 4). *Downstream Boundary-Normal Depth? - Kleinschmidt*. https://www.kleinschmidtgroup.com/ras-post/downstream-boundary-normal-depth/

Gulbrandsen, T. (2017). *NDH Surnadal-Rindal 2pkt 2016* [LASERSKANNING FOR NASJONAL DETALJERT HØYDEMODELL]. TerraTec AS.

Hall, J., Tarantola, S., Bates, P., & Horritt, M. (2005). Distributed sensitivity analysis of flood inundation model calibration. *Journal of Hydraulic Engineering*, *131*(2), 117–126.

Hanssen-Bauer, I., Førland, E. J., Haddeland, I., Hisdal, H., Lawrence, D., Mayer, S., Nesje, A., Nilsen, J. E. Ø., Sadven, S., Sandbø, A. B., Sorteberg, A., & Ådlandsvik, B. (2017). *Climate in Norway 2100 – a knowledge base for climate adaptation*. *1/2017*.

HEC-RAS Release Notes. (n.d.). Retrieved 15 June 2023, from https://www.hec.usace.army.mil/confluence/rasdocs/rasrn

Hong Quang, N., Tuan, V. A., Thi Thu Hang, L., Manh Hung, N., Thi The, D., Thi Dieu, D., Duc Anh, N., & Hackney, C. R. (2019). Hydrological/hydraulic modeling-based thresholding of multi SAR remote sensing data for flood monitoring in regions of the Vietnamese Lower Mekong River Basin. *Water*, *12*(1), 71.

Horritt, M. (2006). A methodology for the validation of uncertain flood inundation models. *Journal of Hydrology*, *326*(1–4), 153–165.

Horritt, M., & Bates, P. (2001). Predicting floodplain inundation: Raster-based modelling versus the finite-element approach. *Hydrological Processes*, *15*(5), 825–842.

Horritt, M., & Bates, P. (2002). Evaluation of 1D and 2D numerical models for predicting river flood inundation. *Journal of Hydrology*, *268*(1–4), 87–99.

Horritt, M., Di Baldassarre, G., Bates, P., & Brath, A. (2007). Comparing the performance of a 2-D finite element and a 2-D finite volume model of floodplain inundation using airborne SAR imagery. *Hydrological Processes: An International Journal*, *21*(20), 2745–2759.

Horritt, M., Mason, D., Cobby, D., Davenport, I., & Bates, P. (2003). Waterline mapping in flooded vegetation from airborne SAR imagery. *Remote Sensing of Environment*, *85*(3), 271–281.

Horritt, M., Mason, D., & Luckman, A. (2001). Flood boundary delineation from synthetic aperture radar imagery using a statistical active contour model. *International Journal of Remote Sensing*, *22*(13), 2489–2507.

Hostache, R., Matgen, P., Schumann, G., Puech, C., Hoffmann, L., & Pfister, L. (2009). Water level estimation and reduction of hydraulic model calibration uncertainties using satellite SAR images of floods. *IEEE Transactions on Geoscience and Remote Sensing*, *47*(2), 431–441.

Hygen, H. O. (2023). *Klimarapport 2023*. Finans Norge.

Irish, J. L., & White, T. E. (1998). Coastal engineering applications of high-resolution lidar bathymetry. *Coastal Engineering*, *35*(1–2), 47–71.

Kalsnes, B., Solheim, A., Sverdrup-Thygeson, K., Dingsør-Dehlin, F., Wasrud, J., Indrevær, K., & Bergbjørn, K. (2021). *Flom og skred–sikringsbehov for eksisterende bebyggelse (FOSS)*.

LaRocque, P. E., & West, G. R. (1999). Airborne laser hydrography: An introduction. *Proc. ROPME/PERSGA/IHB Workshop on Hydrographic Activities in the ROPME Sea Area and Red Sea*, *4*, 1–15.

Leatherman, S. P. (2003). Shoreline change mapping and management along the US East Coast. *Journal of Coastal Research*, 5–13.

Leine, A.-L. Ø. (2018). *Flomberegning for Surna (112. Z)*. Rapport.

Liang, J., & Liu, D. (2020). A local thresholding approach to flood water delineation using Sentinel-1 SAR imagery. *ISPRS Journal of Photogrammetry and Remote Sensing*, *159*, 53–62.

Lin, C. S. (1995). Airborne lidar remote sensing of terrain and ocean. *1995 International Geoscience and Remote Sensing Symposium, IGARSS'95. Quantitative Remote Sensing for Science and Applications*, *3*, 2316–2318.

Lobintceva, E. (2014). *Estimating runoff from ungauged catchments using regional modelling* [Master's Thesis]. Institutt for vann-og miljøteknikk.

Mangidi, U., Mandaya, I., & Ngii, E. (2023). Utilization of Sentinel 1 SAR for Flood Mapping in North Konawe Regency, Southeast Sulawesi Province, Indonesia. *IOP Conference Series: Earth and Environmental Science*, *1134*(1), 012019.

Marks, K., & Bates, P. (2000). Integration of high-resolution topographic data with floodplain flow models. *Hydrological Processes*, *14*(11–12), 2109–2122.

Mason, D. C., Cobby, D. M., Horritt, M. S., & Bates, P. D. (2003). Floodplain friction parameterization in two-dimensional river flood models using vegetation heights derived from airborne scanning laser altimetry. *Hydrological Processes*, *17*(9), 1711–1732.

Matgen, P., Schumann, G., Henry, J.-B., Hoffmann, L., & Pfister, L. (2007). Integration of SAR-derived river inundation areas, high-precision topographic data and a river flow model toward near real-time flood management. *International Journal of Applied Earth Observation and Geoinformation*, *9*(3), 247–263.

McMillan, H., Krueger, T., & Freer, J. (2012). Benchmarking observational uncertainties for hydrology: Rainfall, river discharge and water quality. *Hydrological Processes*, *26*(26), 4078–4111.

Mehendale, N., & Neoge, S. (2020). Review on Lidar Technology. *Available at SSRN 3604309*.

Melby, S. (2019, June 3). Øvre Surnadal og nedre Rindal. *NORDMØRSBILDER*. https://ksu.no/artikler/dagens-bilde/96915-gjemnessundet-og-litlholmen-2

Melkamu, T., Bagyaraj, M., Adimaw, M., Ngusie, A., & Karuppannan, S. (2022). Detecting and mapping flood inundation areas in Fogera-Dera Floodplain, Ethiopia during an extreme wet season using Sentinel-1 data. *Physics and Chemistry of the Earth, Parts A/B/C*, *127*, 103189.

Merz, B., & Thieken, A. H. (2005). Separating natural and epistemic uncertainty in flood frequency analysis. *Journal of Hydrology*, *309*(1–4), 114–132.

Ministry of Emergency Management, Beijing Normal Universit, National Disaster Reduction Centre of China, & International Federation of Red Cross and Red Crescent Societies. (2022). *2021 Global Disaster Assessment Report*.

Mostert, E., & Junier, S. J. (2009). The European flood risk directive: Challenges for research. *Hydrology and Earth System Sciences Discussions*, *6*, 4961–4988. https://doi.org/10.5194/hessd-6-4961-2009

Multiconsult, for S. S. (2010). *Flomberegninger for Grytten, Svorka og Trollheim (22.06.10)*.

Navalgund, R., V, J., & Roy, P. (2007). Remote sensing applications: An overview. *Current Science*, *Vol. 93*.

Neal, J., Keef, C., Bates, P., Beven, K., & Leedal, D. (2013). Probabilistic flood risk mapping including spatial dependence. In *Hydrological Processes* (Vol. 27, Issue 9, pp. 1349–1363). Wiley Online Library.

Nicholas, A., & Walling, D. (1997). Modelling flood hydraulics and overbank deposition on river floodplains. *Earth Surface Processes and Landforms: The Journal of the British Geomorphological Group*, *22*(1), 59–77.

Overview | Get to Know SAR – NASA-ISRO SAR Mission (NISAR). (n.d.). Retrieved 14 June 2023, from https://nisar.jpl.nasa.gov/mission/get-to-know-sar/overview/

Pappenberger, F., Beven, K., Horritt, M., & Blazkova, S. (2005). Uncertainty in the calibration of effective roughness parameters in HEC-RAS using inundation and downstream level observations. *Journal of Hydrology*, *302*(1–4), 46–69.

Pappenberger, F., Beven, K. J., Ratto, M., & Matgen, P. (2008). Multi-method global sensitivity analysis of flood inundation models. *Advances in Water Resources*, *31*(1), 1–14.

Park, J.-W., Korosov, A., & Babiker, M. (2017). Efficient thermal noise removal of Sentinel-1 image and its impacts on sea ice applications. *EGU General Assembly Conference Abstracts*, 12613.

Pham-Duc, B., Prigent, C., & Aires, F. (2017). Surface water monitoring within Cambodia and the Vietnamese Mekong Delta over a year, with Sentinel-1 SAR observations. *Water*, *9*(6), 366.

Prinos, P. (2009). Review of flood hazard mapping. *T03-07-01*.

Rana, V. K., & Suryanarayana, T. (2019). Evaluation of SAR speckle filter technique for inundation mapping. *Remote Sensing Applications: Society and Environment*, *16*, 100271.

Robinson, D., Zundel, A., Kramer, C., Nelson, R., deRosset, W., Hunt, J., Hogan, S., & Lai, Y. (2019). TWO-DIMENSIONAL HYDRAULIC MODELING FOR HIGHWAYS IN THE RIVER ENVIRONMENT – REFERENCE DOCUMENT. *FHWA-HIF-19-061*.

Romanowicz, R., & Beven, K. (2003). Estimation of flood inundation probabilities as conditioned on event inundation maps. *Water Resources Research*, *39*(3).

Sanchez, A. (2021). *HEC-RAS Two-Dimensional Sediment User Manual* (Version 6.1.0). US Army Corps of Engineers.

Savage, J. T. S., Bates, P., Freer, J., Neal, J., & Aronica, G. (2016). When does spatial resolution become spurious in probabilistic flood inundation predictions? *Hydrological Processes*, *30*(13), 2014–2032.

Schumann, G., Di Baldassarre, G., & Bates, P. D. (2009). The utility of spaceborne radar to render flood inundation maps based on multialgorithm ensembles. *IEEE Transactions on Geoscience and Remote Sensing*, *47*(8), 2801–2807.

Schumann, G. J., Brakenridge, G. R., Kettner, A. J., Kashif, R., & Niebuhr, E. (2018). Assisting flood disaster response with earth observation data and products: A critical assessment. *Remote Sensing*, *10*(8), 1230.

Schumann, G. J.-P., & Moller, D. K. (2015). Microwave remote sensing of flood inundation. *Physics and Chemistry of the Earth, Parts a/b/c*, *83*, 84–95.

Schumann, G. J.-P., Neal, J. C., Mason, D. C., & Bates, P. D. (2011). The accuracy of sequential aerial photography and SAR data for observing urban flood dynamics, a case study of the UK summer 2007 floods. *Remote Sensing of Environment*, *115*(10), 2536–2546.

Selmi, L. (2021). *Flood mapping using the Sentinel-1 imagery and the ESA SNAP S1 Toolbox* (Version 1.0). CC BY-NC 4.0.

Sentinel-1C - ITC Satellites and Sensors database. (n.d.). Retrieved 14 June 2023, from https://webapps.itc.utwente.nl/Sensor/getsat.aspx?name=Sentinel-1C

Sentinel-1—Data Products—Sentinel Online—Sentinel Online. (n.d.). Retrieved 14 June 2023, from https://sentinels.copernicus.eu/web/sentinel/missions/sentinel-1/data-products

Sentinel-1—Mission Summary—Sentinel Online—Sentinel Online. (n.d.). Retrieved 14 June 2023, from https://sentinels.copernicus.eu/web/sentinel/missions/sentinel-1/overview/mission-summary

Sentinel-1—Missions—Sentinel Online—Sentinel Online. (n.d.). Retrieved 14 June 2023, from https://sentinel.esa.int/web/sentinel/missions/sentinel-1

Shustikova, I., Domeneghetti, A., Neal, J. C., Bates, P., & Castellarin, A. (2019). Comparing 2D capabilities of HEC-RAS and LISFLOOD-FP on complex topography. *Hydrological Sciences Journal*, *64*(14), 1769–1782.

Skogressurskart (SR16)—Nibio. (n.d.). Retrieved 9 June 2023, from https://www.nibio.no/tema/skog/kart-over-skogressurser/skogressurskart-sr16

Small, D., & Schubert, A. (2008). Guide to ASAR geocoding. *ESA-ESRIN Technical Note RSL-ASAR-GC-AD*, *1*, 36.

Smith, M. J., Edwards, E. P., Priestnall, G., & Bates, P. D. (2006). EXPLOITATION OF NEW DATA TYPES TO CREATE DIGITAL SURFACE MODELS FOR FLOOD INUNDATION MODELLING. *FRMRC Research Report UR3*. www.floodrisk.org.uk

Stephens, E. M., Bates, P., Freer, J., & Mason, D. (2012). The impact of uncertainty in satellite data on the assessment of flood inundation models. *Journal of Hydrology*, *414*, 162–173.

Straatsma, M. W., & Baptist, M. (2008). Floodplain roughness parameterization using airborne laser scanning and spectral remote sensing. *Remote Sensing of Environment*, *112*(3), 1062–1080.

Sun, T., Meakin, P., Jøssang, T., & Schwarz, K. (1996). A simulation model for meandering rivers. *Water Resources Research*, *32*(9), 2937–2954.

Sundt, H., Alfredsen, K., & Harby, A. (2021). Regionalized linear models for river depth retrieval using 3-band multispectral imagery and green lidar data. *Remote Sensing*, *13*(19), 3897.

Tarpanelli, A., Brocca, L., Melone, F., & Moramarco, T. (2013). Hydraulic modelling calibration in small rivers by using coarse resolution synthetic aperture radar imagery. In *Hydrological Processes* (Vol. 27, Issue 9, pp. 1321–1330). Wiley Online Library.

Tavus, B., Kocaman, S., Gokceoglu, C., & Nefeslioglu, H. (2018). Considerations on the use of Sentinel-1 data in flood mapping in urban areas: Ankara (Turkey) 2018 floods. *The International Archives of the Photogrammetry, Remote Sensing and Spatial Information Sciences*, *42*, 575–581.

Te Chow, V. (1959). *Open-channel Hydraulics*. McGraw-Hill. https://books.google.no/books?id=JG9_PwAACAAJ

Teng, J., Jakeman, A. J., Vaze, J., Croke, B. F. W., Dutta, D., & Kim, S. (2017). *Flood inundation modelling: A review of methods, recent advances and uncertainty analysis*.

The Emergency Management Service—Mapping | COPERNICUS EMERGENCY MANAGEMENT SERVICE. (n.d.). Retrieved 9 June 2023, from https://emergency.copernicus.eu/mapping/ems/emergency-management-service-mapping

Tollan, A. (2023). Flom. In *Store norske leksikon*. https://snl.no/flom

Toolboxes. (n.d.). Sentinel Online. Retrieved 8 May 2023, from https://copernicus.eu/toolboxes

Tsubaki, R., & Kawahara, Y. (2013). The uncertainty of local flow parameters during inundation flow over complex topographies with elevation errors. *Journal of Hydrology*, *486*, 71–87.

Ugedal, O., Kvingedal, E., Hagen, I. J., Bremset, G., Jensås, J. G., Karlsson, S., & Østborg, G. (2021). *Fiskebiologiske undersøkelser i Surna. Sluttrapport for perioden 2016-2020*.

Vaze, J., Teng, J., & Chiew, F. (2011). Assessment of GCM simulations of annual and seasonal rainfall and daily rainfall distribution across south-east Australia. *Hydrological Processes*, *25*(9), 1486–1497.

Werner, M., Blazkova, S., & Petr, J. (2005). Spatially distributed observations in constraining inundation modelling uncertainties. *Hydrological Processes: An International Journal*, *19*(16), 3081–3096.

What is Copernicus | COPERNICUS EMERGENCY MANAGEMENT SERVICE. (n.d.). Retrieved 9 June 2023, from https://emergency.copernicus.eu/mapping/ems/what-copernicus

Wood, M., Hostache, R., Neal, J., Wagener, T., Giustarini, L., Chini, M., Corato, G., Matgen, P., & Bates, P. (2016). Calibration of channel depth and friction parameters in the LISFLOOD-FP hydraulic model using medium-resolution SAR data and identifiability techniques. *Hydrology and Earth System Sciences*, *20*(12), 4983–4997.

Wozencraft, J. M., & Lillycrop, W. J. (2003). SHOALS airborne coastal mapping: Past, present, and future. *Journal of Coastal Research*, 207–215.

Zotou, I., Bellos, V., Gkouma, A., Karathanassi, V., & Tsihrintzis, V. A. (2020). Using Sentinel-1 imagery to assess predictive performance of a hydraulic model. *Water Resources Management*, *34*, 4415–4430.

Appendices

Appendix 1: [EMSR557] Surnadal: Delineation Product, version 2, release 1, RTP Map #01

GLIDE number: N/A
Int. Charter Act. ID: N/A

Activation ID: EMSR557
Product N.: 05SURNADAL, v2

SURNADAL - NORWAY

Flood - Situation as of 13/01/2022

Delineation - Overview map 01

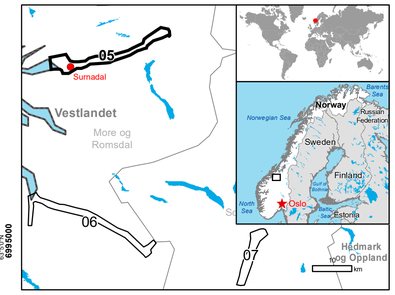

Cartographic Information

1:50000

Full color A1, 200 dpi resolution

0 1 2 4 km

N

Grid: WGS 1984 UTM Zone 32N map coordinate system
Tick marks: WGS 84 geographical coordinate system

Legend

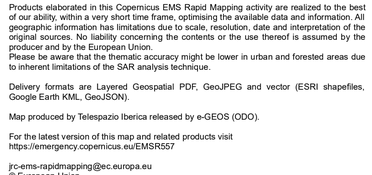

Consequences within the AOI			
		Affected	Total in AOI
Flooded area	ha		543.4
Estimated population		124	5,796
Built-up	ha	0.4	310.4
Transportation	km	16.6	301.1
Facilities	ha	0.0	12.7
Land use	ha	543.6	6,636.8

Full table available in the vector package

Map Information

The extreme weather Gyda will hit western part and central part of Norway on Wednesday 12.01.2022. The extreme weather will bring warm temperatures, wind and heavy rainfall. The combination of rainfall and snow melt is expected to cause floods in many areas. The culmination for larger rivers is expected in the very next days. A high risk of avalanches and landslides is also expected. The Copernicus EMS Rapid Mapping Service has been activated to monitor the flood evolution over the potentially affected areas.

The present map shows the flood delineation in the area of Surnadal (Norway). The thematic layer has been derived from post-event satellite image using a semi-automatic approach. The scale of analysis is 1:20000. The estimated geometric accuracy (RMSE) is 6 m or better, from native positional accuracy of the background satellite image. The minimum mapping unit (MMU) is 576 sq m.

Relevant date records (UTC)

Event	13/01/2022 12:00	Situation as of	13/01/2022 17:21
Activation	11/01/2022 23:27	Map production	24/01/2022

Data sources

Pre-event image: Sentinel-2A (2021) (acquired on 15/09/2021 at 10:57 UTC, GSD 10 m, approx. 0% cloud coverage in AoI) provided under COPERNICUS by the European Union and ESA.

Post-event image: COSMO-SkyMed © ASI (2022), distributed by e-GEOS S.p.A. (acquired on 13/01/2022 at 17:21 UTC, GSD 3.0 m), provided under COPERNICUS by the European Union and ESA, all rights reserved.

Base vector layers: OpenStreetMap © OpenStreetMap contributors (2021), Wikimapia.org, GeoNames 2015, Globe Land 30 (2020), Global Administrative Areas (2012), refined by the producer.
Inset maps: JRC 2013, Natural Earth 2012, GeoNames 2015.

Population data: GHS Population Grid © European Commission, 2019
https://ghsl.jrc.ec.europa.eu/ghs_pop2019.php.

Digital Elevation Model: COP-DEM-EEA-10-R product © DLR e.V. (2014-2018) and © Airbus Defence and Space GmbH (2020) provided under COPERNICUS by the European Union and ESA, all rights reserved.

Disclaimer

Products elaborated in this Copernicus EMS Rapid Mapping activity are realized to the best of our ability, within a very short time frame, optimising the available data and information. All geographic information has limitations due to scale, resolution, date and interpretation of the original sources. No liability concerning the contents or the use thereof is assumed by the producer and by the European Union.
Please be aware that the thematic accuracy might be lower in urban and forested areas due to inherent limitations of the SAR analysis technique.

Delivery formats are Layered Geospatial PDF, GeoJPEG and vector (ESRI shapefiles, Google Earth KML, GeoJSON).

Map produced by Telespazio Iberica released by e-GEOS (ODO).

For the latest version of this map and related products visit
https://emergency.copernicus.eu/EMSR557

jrc-ems-rapidmapping@ec.europa.eu

Copernicus Europe's eyes on Earth

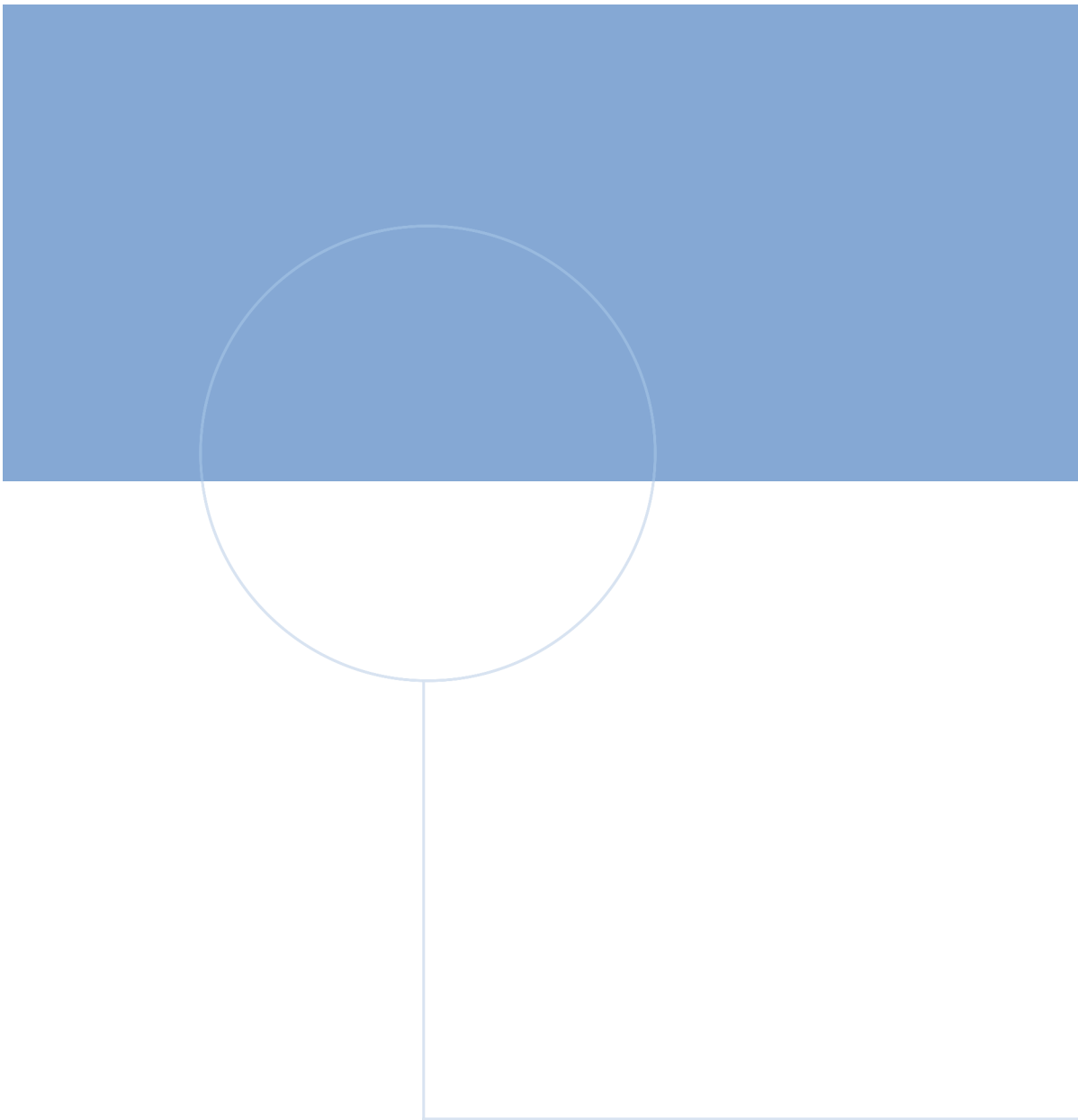

NTNU

Norwegian University of
Science and Technology